Data Analysis of an Unsteady Cavitating Flow on a Venturi-type Profile

Navid Nemati Kourabbasloo

Dissertation submitted to the Faculty of the

Virginia Polytechnic Institute and State University

in partial fulfillment of the requirements for the degree of

Doctor of Philosophy

in

Aerospace Engineering

Olivier Coutier-Delgosha, Chair

Eric G. Paterson

K. Todd Lowe

Yang Liu

August 13th, 2021

Blacksburg, Virginia

Keywords: Instability Modes, Bifurcation Point, Turbulent Energy Cascade, Dominant Balance Identification, Cavitation Model

Copyright 2021, Navid Nemati Kourabbasloo

Data Analysis of an Unsteady Cavitating Flow on a Venturi-type Profile

Navid Nemati Kourabbasloo

(ABSTRACT)

The instability modes and non-linear behavior of a cavitating flow have been studied based on the experimental data obtained from planar Particle Image Velocimetry (PIV). Three data-driven techniques, Proper Orthogonal Decomposition (POD), Dynamic Mode Decomposition (DMD), and Clustered-based Reduced Order Modeling (CROM), are applied to the snapshots of the fluctuating component of velocity to investigate instability modes of the cavitating flow. DMD and POD analysis yield multiple modes are corresponding to slow-varying drift flow, cloud-shedding, and Kelvin-Helmholtz (KH) instability for a fixed inlet flow condition. The high coherence measure obtained from the instabilities suggests a transfer of energy from the largest scales, fluctuating mean flow, to the smaller scales such as cloud cavitation and Kelvin-Helmholtz (KH) instability. It is demonstrated that the POD decorrelation of length scales yields inherently quasi-periodic time dynamics, e.g., incommensurate frequencies. Moreover, the eigenvalue obtained from DMD revealed multiple harmonic with different decay rates associated with the cloud cavitation. The above-mentioned intermittent transition between distinct cloud shedding regimes is investigated via Clustered-based Reduced Order Modeling (CROM). Four aperiodic shedding regimes are identified. 68% of the time, triplets of vortices are formed, while 28% of the time, a pair of vortices are formed in the near wake of the throat. Dominant mechanisms governing the momentum transport and the turbulence kinetic energy production, destruction, and redistribution in distinct regions of the flow field have been identified using Gaussian Mixture Models (GMMs). The preceding data-driven techniques and in-depth analysis of the results facilitated modeling of the cavitation inception and break-up. Accordingly, a phase transition field model is developed using the ultra-fast Time-Resolved Particle Image Velocimetry (TR-PIV) and vapor void fraction spatial and temporal data. The data acquisition is implemented in a Venturi-type test section. The approximate Reynolds number based upon the throat height is $10,000$, and the approximate cavitation number is 1.95. The non-equilibrium cavitation model assumes that the phase production and destruction are correlated to the static pressure field, pressure spatial derivatives, void fraction, and divergence of the velocity field. Finally, the dependence of the model on the empirical constants has been investigated.

Data Analysis of an Unsteady Cavitating Flow on a Venturi-type Profile

Navid Nemati Kourabbasloo

(GENERAL AUDIENCE ABSTRACT)

A cavitation bubble occurs where the pressure field is below the saturation pressure of the liquid. Accumulation of the cavitation bubble forms a cavitating flow. This phenomenon is observed in pumps, propulsion systems, internal combustion engines, and rocket engines. Identifying the mechanisms leading to cavitation-induced damages is imperative in the design of the devices. In this regard, investigation of the cavitation bubble inception, deformation, collapse, and intermittent regime change is mandatory in learning the primary mechanisms of the stresses imposed on the device. Experiments and high-fidelity numerical and analytical methods can be employed to shed light on flow physics. The current study adopted joint experimental methods, data analysis techniques, and computational approaches to scrutinize the unsteady cavitating flow underlying physics as it occurs past the throat of a Venturi-type profile. Different mechanisms of instabilities are identified by applying the data-driven techniques to the raw images of the cavitating flow. The path of the transitions between physically different instabilities mechanisms is examined. The local dominant balance between stress terms in the conservation of momentum equation is identified, and the stress terms roles in cavitating flow instabilities and advective acceleration are determined. A new cavitation model is developed and validated against the experimental results. The new model improves the prediction of the void fraction in different regions of the flow field, making it feasible to simulate different regimes of cavitating flow. Finally, the dominant mechanism governing the liquid-vapor transition and the transport of the void fraction is described.

Dedication

I want to thank my family for their unlimited support and patience in making this accomplishment feasible.

Contents

List of Figures viii

List of Tables xxii

1 Introduction 1

1.1 Introduction to the Physics of Cavitating Flow 1

1.2 History 4

1.3 Objectives of the Current Research 9

1.4 Dissertation Blueprint 13

2 Dynamics of the Unsteady Sheet Cavity and Vapor Cloud 16

2.1 Sheet Cavitation on a Venturi-type Section 16

2.2 Dynamics of the Vapor Sheet on Venturi-type Section 19

2.3 The Collapse of the Cloud Cavitation 22

3 Experimental Design and Measurement Techniques 24

3.1 Experimental Set-up 24

3.2 PIV High-speed Photography 26

3.3 PIV Measurements 27

3.4 X-ray Imaging 28

4 Mathematical Models and Data-driven Techniques 31

4.1 Non-equilibrium Models 31

4.2 Energy Balance of TKE 40

4.2.1 Standard dynamic mode decomposition algorithm 42

4.3 The Nonlinear Dynamic States 46
4.4 CROM Algorithm 50
4.5 POD Time Dynamics Mathematical Model 54
4.6 Pressure Reconstruction Method 59
4.7 Uncertainty Quantification of Pressure Field 62
4.8 Favre-averaged Navier-Stokes Equations 64
4.9 Gaussian Mixture Model 68
4.10 Phase Transition Modeling 70

5 Verification and Validation of Mathematical Models 73

5.1 Free-stream 75
5.2 Boundary Conditions 75
5.3 Computational Domain 75
5.4 Computational Mesh 76
5.5 Spatial and Temporal Schemes 77
5.6 Results and Analysis 77

6 Data-driven Modal Analysis 83

6.1 Introduction 83
6.2 Analysis of the High-speed Images 89
6.3 Technique # 1: Applications of DMD to the Flow Past the Throat of the Venturi Test Section 91
6.3.1 Application and results of DMD technique 91
6.3.2 Analysis and discussion of DMD results 93
6.4 Technique # 2: Applications of POD to the Flow Past the Throat of the Venturi Test Section 98
6.4.1 POD technique application 98

6.4.2 Nonlinear behavior based on POD dynamics 99
6.4.3 POD time dynamics modeled via system of ODEs 110
6.4.4 Interactions of the POD length scales 112
6.5 Technique # 3: Applications of CROM to the Flow Past the Throat of the Venturi Test Section 121
6.5.1 Application of CROM technique 121
6.5.2 Analysis and discussion of CROM results 122
6.6 Conclusions on the Modal Analysis of the Cavitating Flow 128

7 Dominant Physical Mechanisms 131
7.1 Introduction 131
7.2 Exact Compressible Turbulence Kinetic Energy Equation 133
7.3 Favre-averaged Momentum Equation in a Cavitating Flow 138
7.4 Favre-averaged Momentum Transport Dominant Mechanisms in Transition to Cavitating Flow 140
7.5 Compressible Momentum Transport Dominant Mechanisms in Transition to Cavitating Flow 145
7.6 Conclusions on Dominant Physical Mechanisms on Venturi-type Profile . . . 149

8 Data-driven Discovery of Phase Transition Field Equation 152
8.1 Introduction 152
8.2 Phase Transition Modeling in Distinct Regions of Cavitating Flow 156

9 Conclusions and Future Research Directions 168
9.1 Conclusions 168
9.2 Future Research Directions 172

Bibliography 174

List of Figures

1.1 Snapshots captured from the cavitating flow past the throat of the Venturi-type section at $U_\infty = 9.53m/s$, $\sigma = 1.95$, and $Re = 1.00 \times 10^5$. (a) A snapshot of the attached sheet cavity past the throat of a Venturi-type test section. The cavitation sheet is limited to the bottom wall. (b) Large scale vapor cloud shedding on the downstream. (c) Condensation of the vapor cloud on the downstream due to the pressure recovery. 3

2.1 Sheet cavity evolution, vapor shedding, and cloud collapse in sequential frames captured from the cavitatig flow past the throat of the Venturi-type section at $U_\infty = 9m/s$, $\sigma = 0.96$, and $Re = 4.44 \times 10^4$ [48]. The throat width and height are $3.6mm$ and $10.8mm$, respectively. 17

2.2 The typical sequence for the evolution of the sheet cavity and oscillation of its length [48]. In this case, no cloud shedding is observed. The flow condition is similar to cavitation evolution illustrated in figure 2.1 . The throat width and height are $6.7mm$ and $2.7mm$, respectively. 18

2.3 Frame # 8 depicting the maximum length acquired by the attached sheet cavity [48]. For further information of the section geometry and flow, condition look at figure 2.1 20

2.4 Cavitation in a comparatively wide test section at $U_\infty = 9m/s$, $\sigma = 0.96$, $Re = 3.48 \times 10^4$ [48]. The throat width and height are $15mm$ and $2.7mm$, respectively. Depiction of the collision of the re-entrant jet with the side walls due to the re-entrant jet sharp angle. 21

2.5 Representation of the condensation of the cloud cavity on the downstream [48]. For further information on the section geometry and flow condition, look at figure 2.1. 21

2.6 Coalescence of the vapor cloud structures in the downstream [48]. The prescribed flow condition is $U_\infty = 17m/s$, $\sigma = 0.98$ and $Re = 8.09 \times 10^4$. For further information of the section geometry look at figure 2.6. 21

2.7 Single large-scale cloud convection on the downstream [48]. For further information of the flow conditions and the section geometry look at figures 2.6 and 2.1, respectively 21

3.1 (a) Schematic diagram of the test rig. (b) Venturi type test section profile; the confining bottom (2) and top (3) walls leaving the channel with a convergent wedge at the entrance and a divergent one toward the outlet. The flow is from left to right 24

3.2 PIV system apparatus in the front view of the Venturi section showing the Nd: YLF laser, the laser beam, VEO 710L, and FASTCAM SA1.1 cameras, density and notch filters, reflecting mirrors, and flow direction. The flow is from left to right. For further information of the test rig look at figure 3.1. . 27

3.3 (a) Schematic diagram of X-ray light source located at the APS composed of the X-ray light source, X-ray beam, slow and fast shutters, test section, scintillator, and camera [30]. (b) diagram of the X-ray pulse duration, x-axis, versus shutter opening width, y-axis. The fast shutter time during, $9\mu m$, accommodates a pair of camera frames used to implement PIV analysis. The first (second) camera frame detects the primary (secondary) X-ray pulse that creates the image pair for the PIV analysis. 29

3.4 (a) Schematic of X-ray scanning positions [30]. Position # 1 is located adjacent to the throat of the Venturi-type section where the cavitation inception is observed. In each campaign, the test section is moved to the new position to complete the data acquisition. (b) An X-ray image of the cavitating flow at window # 2 illustrates the silver-coated hollow glass spheres overlaid with the vapor structures. 30

5.1 The figure represents the flow over a flat plate as a boundary of the computational domain. The solution domain extends $204 \times L$, in the spanwise direction, where L is the half thickness of the plate. The flat plate extends to 1050 half thickness of the plate downstream of the leading edge. 76

5.2 Representation of the relative error between the DNS data, which is the true value, and the estimated pressure field obtained from the in-house compressible CFD code (a) Instantaneous pressure distribution of transitional boundary-layer obtained from the Direct Numerical Simulations (DNS) of an incompressible flow over a flat plate [40] at $t = 0.5$ sec. and $Re_L = 800$. (b) Instantaneous pressure distribution obtained from the numerical simulation of compressible form of the pressure Poisson equation, Eq. (4.88). (c) streamwise pressure gradient at $\frac{y}{L} = 20$. (d) Convergence of the pressure field in the L_2 norm. (e) Streamwise pressure distribution on the plate. (f) Streamwise pressure distribution at $\frac{y}{L} = 20$. 79

5.3 Flow characteristics past the throat of the Venturi-type test section at location (1), look at figure 3.4 (a) Sample of the instantaneous pressure gradient vector field overlaid with the contours of the instantaneous gas volume fraction. (b) Sample of the velocity vector overlaid with the contour of the instantaneous pressure field. (c) Time-averaged pressure field at location (1). (d) Sample of instantaneous solenoidal iso-contour depicting baroclinity's high value inside the attached sheet cavity and on the vapor-liquid interface. A high value of baroclinity is the primary mechanism of the attached sheet instability. The misalignment of the pressure gradient vector field (green arrows) and the density gradient vector field (blue arrows) influence the vorticity field. Baroclinic torque is an imperative mechanism of the intermittent vapor jet propagating. 81

5.4 Representation of the one-dimensional uncertainty propagation from the velocity vector field and the local void fraction to the pressure field. The measurement uncertainties for the velocity vector field of the liquid-vapor mixture and single-phase flow are $0.46\frac{m}{s}$ and $0.11\frac{m}{s}$, respectively. The uncertainty measurement of the local void fraction is 0.06. Graphs show the standard deviation of the calculated pressure using the Monte Carlo simulations in the (a) single-phase flow and the (b) cavitating flow. 82

6.1 Visualization of the velocity vector field overlapped with the raw images from high-speed photography. Illustration of the re-entrant jet, shear instability, intermittent cloud shedding and condensation process as it occurs in a Venturi-type profile at $Re = 15,000$ and $\sigma = 1.95$. The blue (red) vector field depicts the stream-wise velocity (re-entrant jet). Frame # 1-3 depicts a strong re-entrant jet (red arrows) of the liquid phase followed by the intermittent cloud shedding. Frame # 4 illustrates the vapor structures' dissipation as they are convecting on the downstream. Frame # 7-9 shows the convection of the large-scale cloud shedding. 91

6.2 Representative of the DMD mode shapes, visualized by the velocity magnitude, for the liquid phase at $Re_h = 15,000$, and $\sigma_{cav} = 1.95$. (a-b) The largest coherent structures correspond to the instability created due to velocity shear on the liquid phase and vapor phase interface, (c-l) unstable branch corresponding to the vortical coherent structures of the liquid-phase induced by quasi-periodic shedding and condensation of the cloud cavitating. 96

6.3 (a) DMD spectrum versus the initial amplitudes of the mode shapes associated with the velocity magnitude of the liquid phase at $Re_h = 15,000$, and $\sigma_{cav} = 1.95$. (b) Monotonic decay rate associated with each mode. 97

6.4 Complex eigenvalues of $\hat{A}$ matrix for cavitating flow with $Re =$ and $\sigma_{cav} =$. Eigenvalues lie inside the unit circle implying the convergence, e.g., monotonic decay, of the corresponding mode. 97

6.5 (a) POD mode shapes of the liquid-phase velocity components. The flow is visualized using the iso-contours of the transversal velocity component. (b) POD time coefficients of the transversal velocity of the first eight modes. (c) Power spectral of the time coefficients of the transversal velocity of the first eight modes 101

6.6 The figure depicts the spectrum of the coherence measure associated with the POD mode pairs (a) one and (b) two. The high value of the coherence indicates a linear interaction between the signals, while low coherence indicates a correlation with the nonlinear phenomenon or noise. The figure shows the PDF of the phase difference between the POD time dynamics of mode pairs (c) one and (d) two. The high probability around 90° suggests that the kinetic energy mutually is transferred between the corresponding POD modes. . . . 102

6.7 The figure presents the wavelet coherence of the first four energetic POD mode coefficients: the scalogram of coherence measure. Contours depict the coherence measures. The vectors indicate the phase difference between POD time coefficients only where the coherence measure is greater than or equal to 0.8. A vertical arrow displays an out-phase pair of signals, and a horizontal arrow denotes an in-phase pair of signals. A dashed white line is used to discriminate between the data susceptible to the edge effects from the graph's high-fidelity region. 105

6.8 Representation of the trajectories in the state space for (a) the first pair, (b) the second pair, (c) modes one and three, and (d) mode one and mode four of the POD time coefficients associated with the transversal velocity. The percentage of the FNN versus the number of embedding dimensions for the first four POD coefficients trajectories in the phase-space. FNN is computed at the symbol points and is connected by linear regression. 107

6.9 FTLE distribution function associated with POD time dynamics of the first four modes for the different realization of time interval samples, $L = 1, 10, 100$. 109

6.10 Ten-fold cross-validation error for the POD time dynamics for different realization of $\lambda_{reg.}$. Mean Squared Error (MSE) is obtained via cross-validation (red square-shaped dots) and one-standard-deviation grey bars associated with the uncertainty band. 111

6.11 POD time dynamics probability distribution functions associated with modes (a) one, (b) two, (c) three, and (d) four obtained from the experimental data (dashed, red line) and the numerical simulation of the coupled ODEs dynamical model (solid blue line). 112

6.12 (a) 2-dimensional (2D) POD mode shapes of slowly varying drift flow. Shown are the iso-contours of the transversal velocity components. (b) Time fluctuation of the first two POD modes, (c) and the associated spectrum. Time fluctuation of the modes represents the fluctuations of the available energy of the corresponding mode. 113

6.13 (a) (2D) POD mode shapes of KH instability. Shown are the iso-contours of the transversal velocity components. (b) Time fluctuation of the first two POD modes, (c) and the associated spectrum. Further information can be found in figure 6.12 114

6.14 Representation of the linear link between the POD modes of low wavenumber drift flow and KH instability. The wavelet coherence between drift flow and KH instability time dynamics: the scalogram of coherence measure. The first subscript defines the mode number of the drifting flow, and the second subscript represents the mode number of the KH instability. Further explanation of the graph is illustrated in figure 6.7. 115

6.15 (a) (2D) POD mode shapes are associated with high-frequency cloud shedding. Shown are the iso-contours of the transversal velocity components. (b) Time fluctuation of the first two POD modes, (c) and the associated spectrum. Further information can be found in figure 6.12. 116

6.16 POD time dynamics of the drifting flow, KH instabilities, and cloud-shedding POD mode pairs. Red circles (blue diamond) display the snapshots where the amplitude of the first (second) POD mode of drift flow is greater than %65. Gray squares (orange crosses) display the snapshots where the amplitude of the first (second) POD mode of KH instabilities is greater than %65. Green plus signs (cyan asterisks) display the snapshots where the amplitude of the first (second) POD mode of cloud-shedding is greater than %65. First two dominant POD modes of the drifting flow, attached sheet cavity, and cloud shedding. The flow is visualized through the contours of the transversal velocity component. 119

6.17 The figure illustrates the visualization of the velocity vector field overlapped with the raw images from high-speed photography. The blue (red) vector field depicts the stream-wise velocity (re-entrant jet). (a) Representation of the premature condensation of the cloud at the leading edge of the attached sheet cavity (frames 2-4). (b) Representation of the large-scale cloud cavitation convection and the consequent condensation due to the pressure recovery at the outlet (frames 8-18). (c) Representation of a series of intermittent small-scale clouds shedding (frames 20-46). 120

6.18 The figure shows the Voronoi diagram of the clusters, the cluster centroids (solid black bullets labeled with numbers), the data points (solid color dots) projected in the two-dimensional space of the first two POD time dynamics ν_1 and ν_2. Clusters are discriminated through different colors assigned to the dots. Dots trespassing the borders of the corresponding cluster indicate that the attractor lives in higher dimensions. 123

6.19 (a) CTM and (b) cluster centroid distance matrix. Simplification of the connectivity between the cluster centroids yields Three cluster dominant groups, figure 6.21, $k' = 1, 2, 3, 4$, $k' = 5, 6, 7, 8, 9$, and $k' = 11, 12, 13, 14, 15, 16, 17, 18, 19, 20$. One transition cluster $k' = 10$ that is associated with the vortex pairing is observed in the matrices. 125

6.20 CROM mode shapes, corresponding the cluster centroid $\kappa = \{c_1, c_2, ..., c_{k_{tot}}\}$. The colors show the contours of positive (red) and negative (blue) velocity for each cluster centroid. The flow is coming from left to right. 126

6.21 CTM schematic diagram of the velocity field associated with the liquid phase. The arrows indicate the direction of the possible transitions. A threshold is chosen to simplify the connectivity diagram. The diagram depicts three cyclic cluster groups associated with the convection of coherent triplet structures (gray and black clusters) and pair structures (white clusters). The green cluster represents an intermittent phenomenon that occurs as a consequence of the bifurcation point. 127

6.22 Stability analysis of the CTM: (a) complex eigenvalues of CTM with the largest eigenvalue equals to +1. The color bar displays the absolute value of the eigenvalue (b) $q_{k'}$ the initial probability distribution of the data, ρ_∞ corresponds to the asymptotic PDF, the eigenvector $\omega_{CTM,1}$ associated with the dominant eigenvalue (c) converged CTM. All eigenvalues are located inside of the unit circle implying that the dynamical system is *ergodic*. 128

7.1 Representation of the exact turbulence kinetic energy equation for the cavitating flow (a) rate of change of TKE due to the instability in the mean flow (b) rate of change of TKE due to the advection of the mean flow(c) Rate of production of TKE extracted from the non-stationary signal of the mean flow (d) fluctuating viscous stresses work against the fluctuating strain rates or deformation of the fluid material or velocity deformation rate. (e) Transport of TKE due to the viscous stresses (f) Transport of the TKE due to the velocity fluctuations. (g) mechanism of transportation of the TKE due to the pressure fluctuations. 137

7.2 Representation of the Favre-averaged momentum equation where the sheet cavity is formed. (a) rate of change of momentum of the fluid element as a result of the mean flow instability. (b-c) rate of change in momentum of the fluid element owing to the advection as it occurs in the mean flow. (d) the isotropic stress applied as a result of the mean pressure field gradient. (e-f) Reynolds stresses as a result of the fluctuations in the velocity vector field. (g-h) Viscous stresses are applied to the fluid element due to the molecular processes. 139

7.3 The figure presents the Identification of the dominant terms on the Favre-averaged momentum equation in x-direction represented by covariance matrices inferred by the GMM. Covariance matrices depict dominant terms in separate regions: region (1) volume fraction is significantly high, region (2) freestream, regions (3), (5) interface of the liquid and gas phases, region (4) wall-bounded cavitating flow, and region (6) where most of the terms are contributing to the balance. 142

7.4 Visualization of the equation space associated with Favre-averaged momentum equation in the cavitating flow. The equation space representation enables clustering and sparse approximation of the momentum equation. Extraction of distinct geometrical structures in the space corresponding to dominant balance terms is feasible. The equation space represents the correlation of the forces in momentum equation in non-overlapping regions of the flow field. The dominant forces in each region can be extracted and the balance between different forces can be studied. 144

7.5 Schematic of the dominant balance identification applied to a cavitating flow for $\lambda_{reg} = 10^7$. The equation space is associated with the Favre-averaged momentum equation in the x-direction. (a) The entire domain is segmented using the balance models shown in (c). The segmentation enables the identification of distinct regimes of flow. GMM probabilistic model enables investigation of the clustering uncertainty. (b) Summation of the uncertainty associated with the models that cannot be accommodated in the balance relation. (d) Residuals of the inactive terms in the models as a Sparse Principal Component Analysis (SPCA) regularization function. 145

7.6 Schematic of the dominant balance identification applied to a cavitating flow for $\lambda_{reg} = 10^7$. The equation space is associated with the compressible momentum equation in the x-direction. (a) The entire domain is segmented using the balance models shown in (c). (b) Summation of the uncertainty associated with the models that cannot be accommodated in the balance relation. (d) Residuals of the inactive terms in the models as a Sparse Principal Component Analysis (SPCA) regularization function. 147

7.7 The figure presents the visualization of the equation space associated with the compressible momentum equation in the cavitating flow. SPCA is employed to the set of points in each GMM cluster and. For further information look at figure 7.4 148

8.1 Norm two obtained from the discrepancy between the void fraction transport relation, $\frac{\partial \alpha}{\partial t} + u\frac{\partial \alpha}{\partial x} + v\frac{\partial \alpha}{\partial y}$,and vapor phase transition model, $\dot{m}_v$ in different regions of the flow field: (a) inception of the cavitation (b) vapor phase shedding, (c) break-up of the vapor phase and (d) condensation of the vapor structures. Models suggested for each region is presented in Eqs. (8.2)-(8.5). 158

8.2 Representation of the non-equilibrium cavitation model suggested for region # 1 where the vapor phase is massively generated due to the high-pressure gradient. (a) the pressure gradient mainly governs the mass transition term. 159

8.3 Representation of the non-equilibrium cavitation model suggested for region # 2 where the shedding of cloud cavitation is initiated. (a), (b) negative (positive) pressure gradient patches result in a sudden drop (increase) of the pressure field. The negative pressure gradient is the forerunner of cavitation structures production. A strong negative pressure gradient is observed at the liquid-vapor interface, where the pressure gradient is the dominant mechanism in cavitation production. (c) Divergence of the velocity represents the second mechanism of the production or condensation of the vapor structures. The negative (positive) patches of the divergence of the velocity delineate an expansion (contraction) of fluid element leading to production (destruction) of the vapor phase. (d) Instantaneous snapshot of the field of the void fraction in the near wake of the throat. 162

8.4 Representation of the non-equilibrium cavitation model suggested for region # 3 where the cavitation break-up occurs. (a) the divergence of the velocity mainly governs the mass transition term. For further information, look at figure 8.3 (b) Instantaneous snapshot of the field of the void fraction where the cavitation break-up occurs. 162

8.5 Representation of the non-equilibrium cavitation model suggested for region # 4 where the pressure recovery occurs. (a) the pressure field mainly governs the mass transition term. Since the pressure drops in the near wake, condensation of the vapor structures occurs. (b) Instantaneous snapshot of the field of the void fraction in the near wake of the Venturi-type section throat. . . . 163

8.6 Schematic of the dominant balance identification applied to a cavitating flow for $\lambda_{reg} = 10^3$. The equation space is associated with the void ratio transport equation that governs cavitating flow right after the throat of the Venturi-type section. For further information look at figure 7.5. 164

8.7 Schematic of the dominant balance identification applied to a cavitating flow for $\lambda_{reg} = 10^3$. The equation space is associated with the void ratio transport equation that governs cavitating flow where the vapor cloud shedding occurs. For further information look at figure 7.5. 165

8.8 Schematic of the dominant balance identification applied to a cavitating flow for $\lambda_{reg} = 10^2$. The equation space is associated with the void ratio transport equation that governs cavitating flow where the cavitation break-up initiates. For further information look at figure 7.5. 166

8.9 Schematic of the dominant balance identification applied to a cavitating flow for $\lambda_{reg} = 10^3$. The equation space is associated with the void ratio transport equation that governs cavitating flow in the near wake, where the pressure recovery imposes the condensation of the vapor phase. For further information look at figure 7.5. 167

List of Tables

3.1 Some important system parameters 26

3.2 Overview of the relevant PIV parameters applied to the raw images obtained from the high speed photography. 28

5.1 computational domain size, number of grid points, and spatial resolution of boundary-layer at $x = 1000 \times L$ 77

6.1 LLE, embedding dimensions, mean period, number of the period for the entire sample, and time lag for the time evolution of the temporal coefficients of POD modes. 110

6.2 Values of the coefficients defining the model of the POD time dynamics, Eq. (6.1) 112

Chapter 1

Introduction

1.1 Introduction to the Physics of Cavitating Flow

Cavitation occurs due to the sudden local pressure drops below the saturation pressure associated with that liquid. Understanding the dynamics of flow structures with partial cloud cavitation is imperative in designing mechanical devices, including propellers, rudders, hydraulic machinery, etc. Cavitation inception and condensation of the cloud cavitation generate substantial noise and vibrations, thereby decreasing the efficiency of the mechanical device. An in-depth insight into a two-phase flow paves way toward control of the instabilities and reduces cavitation erosion.

Distinct types of cavitation has been enumerated in the literature [7, 14, 22, 23]. In the current dissertation, dynamics of the energy-carrying coherent structures such as attached sheet cavitation, sheet cavitation, wall-bounded cavitation and cloud cavitation are studied, look at figure 1.1. Sheet cavitation and attached sheet cavitation occurs past the throat of the Venturi-type section where local pressure is significantly below the vapor pressure. These types of cavitation is inevitable due to prescribed geometry and upstream velocity. Local premature condensation of the cavitation structure at the tip of attached sheet cavitation may give rise to pressure fluctuations and consequently erode the mechanical device [46]. Condensation of the cloud cavitation in the downstream may also be a source of cavitation

erosion [27]. At the leading edge of the sheet cavity a re-entrant jet has been observed that might govern the time and length scales of the cloud shedding. The re-entrant jet and the cloud vapor structures create highly vortical regions. A relatively high local pressure may lead vapor structures to condensate. Premature condensation or vapor cloud condensation sends out strong pressure instabilities that mechanically damages the surface of the test section [27, 46].

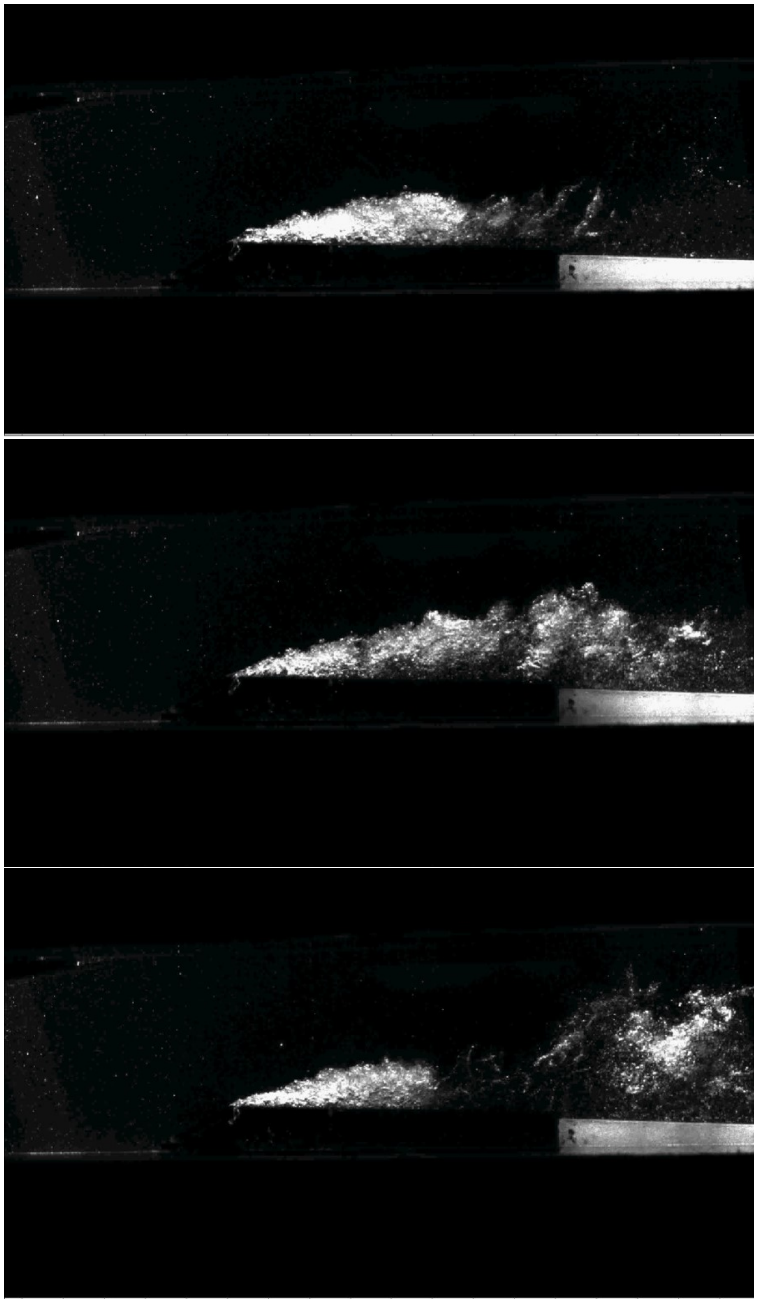

Figure 1.1: Snapshots captured from the cavitating flow past the throat of the Venturi-type section at $U_\infty = 9.53m/s$, $\sigma = 1.95$, and $Re = 1.00 \times 10^5$. (a) A snapshot of the attached sheet cavity past the throat of a Venturi-type test section. The cavitation sheet is limited to the bottom wall. (b) Large scale vapor cloud shedding on the downstream. (c) Condensation of the vapor cloud on the downstream due to the pressure recovery.

1.2 History

The earliest observations of the cavitation flow date back to 1756 by Euler studying the water flow on a rotating machinery [21]. The first formal explanation of the 'cavitation' has been suggested by Froude, describing the void fraction filled with water vapor phase [72]. One of the first observations of the detrimental effect of cavitating flow on the performance and propeller health occurred back in 1895 [63, 74]. Parsson built the first cavitation tunnel to investigate the Destructive effects of cavitation phenomenon [74]. Since then, numerous research work has been published on cavitating flow. The research on cavitating flow falls into three interconnected areas: theoretical, numerical and experimental [23, 32, 42, 63, 74]. These areas can be further split into researches on bubble dynamics and developed cavitating flow.

Research on developed cavitating flow dates back to 1868 [32, 63] and 1869 [42]. These researches were focused on theoretical techniques, including conformal mapping and streamline theory. Birkhoff and Zarantello introduced the Hodograph technique [12]. Wu [77] mentioned that hodograph theory is suitable for bluff bodies and flat plates. In the high-performance computing era, e.g., around the 1970s, Three-dimensional linear methods became feasible. Linear lifting surface theory was amongst the methods used to estimate the sheet cavity. Overestimation of the length of sheet cavity and the void fraction has been mentioned as a disadvantage of this theory. Furthermore, The sheet cavity length variation cannot be predicted by the linear theory [18, 35].

Panel method introduced the possibilities to assess the effect of interface boundary condition nonlinearity on the dynamics of the sheet cavity. This method hypothesizes that the pressure on the cavity interface can be described using constant pressure streamlines. This method captures the dynamic and kinematic of the cavity interface, and the governing equa-

tions are solved iteratively [18, 75]. The panel method assumes that the cavity detachment point is an unknown variable, requiring a closure model to predict the detachment point. Panel method accuracy on the prediction of the detachment region and closure of the sheet cavity is questionable. Furthermore, the prediction of the dynamics of the sheet cavity and the geometry of the cavity seems to be challenging for the panel method. Panel method has abysmal performance on the prediction of the complex physical phenomenon, including cloud shedding.

With an increase in the computational power in the 1990s, new approaches were employed to simulate cavitating flows numerically. One of the popular approaches was the compressible form of Navier-Stokes equations coupled with the transport equation for the void fraction and thermodynamic tables and two-phase flow equilibrium curves. The numerical simulations of the cavitating flow fall into three distinct categories: (1) Two-phase flow methods, (2) Volume of Fluid methods, (3) discrete bubble methods, and (4) Interface tracking methods [35].

In 1992, Kubota et al. [4] used the Rayleigh-Plesset equation coupled with the RANS equations for simulations of the cavitating flow. They computed the void fraction using the radius of the bubble. Since 1992, several researchers proposed cavitation production and destruction terms [3, 8, 16, 33, 49, 56, 57, 60, 66, 70, 79]. Unsteady cavitating flow past the Venturi-type test section is composed of various regimes such as attached sheet cavity, premature condensation, and large-scale cloud shedding. Although numerous cavitation models are developed in the past, very few studies are focused on the performance of the models in distinct regimes of flow, e.g., the cavitation inception and break-up. Besides, the dominant mechanisms and the corresponding physics driving cavitation production (destruction) are

not addressed systematically. In 1998, Merkle et al. [16], and Kunz et al. in 1999 [60] introduced their model of cavitation production (destruction). They imposed artificial compressibility on their model. They used a special preconditioning formulation to solve the momentum transport equations and continuity equations with the RANS turbulence model. In 2002, Singhal et al. [3] introduced their cavitation model, "full-cavitation model". Their model obtains the rate of phase change, given the bubble dynamics and local flow conditions. Although this model simulates the steady sheet cavitation accurately, it fails in an unsteady cavitating regime. In 2003, Saito et al. [79] introduced their cavitation model considering the thermodynamic effects on the production (destruction) terms. The momentum transport equations and continuity equations for the cavitating flow with the RANS turbulence model were solved around a hydrofoil. The turbulent eddy viscosity is based on Baldwin-Lomax with the Degani-Schiff modification.

Homogeneous flow theory describes the multi-phase flow and the corresponding components simply. The theory assumes that the flow of two phases is the simultaneous motion of two phases. Therefore, the homogeneous flow theory assumes that the relative motions between phases do not exist. The fluid mixture properties, including density and viscosity, are the averaged properties of both phases. Besides, two phases are assumed to be in mechanical equilibrium. The assumptions mentioned above are required to derive the governing equations of the flow of the mixture. Assuming that the two species are well mixed and the relative velocity between the species is zero, one may show that the conservation of mass of both species of fluid flow is described as follows:

$$\frac{\partial \rho_m}{\partial t} + \frac{(\partial \rho_m u_i)}{\partial x_i} = 0 \tag{1.1}$$

Where ρ_m is the mixture density:

$$\rho_m = \sum_k \rho_k \alpha_k \tag{1.2}$$

, and u_i is the velocity associated with both of the phases. Since the phases are in mechanical equilibrium, the phases have the same pressure. Besides, the velocity of the flow mixture is assumed to be the same. Given a negligible body force, the mixture momentum equation for an unsteady viscous flow reads:

$$\frac{\partial(\rho_m u_j)}{\partial t} + \frac{\partial}{\partial x_i}(\rho_m u_j u_i) = -\frac{\partial p}{\partial x_j} + \frac{\partial \tau_{ij}}{\partial x_i} \tag{1.3}$$

Besides, to determine the density of the mixture, the advection and temporal changes of one of the phases need to be tracked. Since the mixture is assumed to be homogeneous, tracking the motion of one of the two phases is sufficient to define the density of the mix that is replaced into the conservation of the mass. Therefore, in addition to the mass and momentum conservation, the transport of void fraction is required:

$$\frac{\partial \alpha}{\partial t} + \frac{\partial(\alpha u)}{\partial x} + \frac{\partial(\alpha v)}{\partial y} = \dot{m}_v \tag{1.4}$$

Where $\dot{m}_v$ represents the mass transformation rate from one phase to the other. It should be noted that in this case, the temporal changes of mixture density in the conservation of mass are non-zero.

Evaporation and condensation of the cavity define the liquid-phase transformation. The preceding transformation requires detailed information about the thermodynamic and mechanical states of the phases and the behavior of the interface between them. Kunz et al. [60] suggested a simplified empirical model. They assumed that the transformation from

liquid to vapor phase is distinct from vapor to liquid. Their model implies a correlation between the liquid-vapor transformation with the liquid volume fraction and the value by which the static pressure is below the thermodynamic saturation pressure.

On the other hand, Kunz et al. [60] developed a relationship in which the transformation of the vapor to the liquid phase is proportional to the vapor volume fraction and liquid volume fraction. Similarly, Merkle et al. [16] used the same model for the liquid-phase transformation. The model suggested in the preceding articles simulates the destruction, production accurately. However, the empirical parameter needs to be calibrated for different regimes of cavitating flow. The modeling can be complicated for the fluid flow consisting of distinct physical mechanisms. For instance, the value of the empirical parameter might need to be adjusted depending on location in the flow field. The improvement of the accuracy of the methods mentioned above highly depends on the empirical parameter. The uncertainty of the model parameters which determine the rate of vaporization and condensation is the main limitation of the phase transition relations. Besides, the simulations based on the models mentioned above depict an imperfection in the capturing physics of the cavitating flow [31]. For instance, since the pressure gradient in the mixture of the two phases is not predicted accurately, the cavity does not roll-up. The re-entrant jet is not prominently observed in the closure region of the cavity. Consequently, the intermittent vapor cloud formation and shedding do not occur in the absence of the cavity roll-up and the re-entrant jet. The variation of the vapor cloud and the corresponding frequency of shedding depends on the intermittent re-entrant jet that cannot be predicted.

Schnerr and Sauer [36, 66] developed a dispersed Volume of Fluid (VOF) method for the evolution of the bubble and its collapse. Their numerical model depends on the bubble concentration per unit volume, vapor radius, and the time rate of change of vapor radius. The numerical simulations show that the non-condensable gas effect on the cavitating flow's

inception and evolution and aperiodic behavior is imperative. Schnerr and Sauer model yields significant inaccuracy in the prediction of the unsteady behavior of the cavitating flow, including vapor cloud shedding and condensation process [78].

Charrière et al. [13] assumed that the advection of void fraction and accumulation of the void fraction in an element depends on the divergence of the velocity implying the rate of expansion or contraction of an element. Their model could successfully simulate the aperiodic behavior of vapor cloud shedding as it occurs in a Venturi-type test section. Besides, Charrière et al. [13] model captured the re-entrant jet and the instability in the attached sheet cavity. It does not require any calibration, thereby yielding a set of equations solved for the entire problem domain.

1.3 Objectives of the Current Research

The main objective of the current research is to enhance the understanding of the underlying dynamics of cavitating flow as it occurs in a Venturi-type profile. In this regard, the images obtained from high-speed photography are examined to identify the modes of instabilities in a cavitating flow as it occurs in a specific flow condition. The instantaneous velocity vector field of the liquid and vapor mixture has been obtained using ultra-fast Time-resolved Particle Image Velocimetry (TR-PIV). The instantaneous velocity vector field is further decomposed utilizing three prominent data-driven techniques: standard DMD, POD, and CROM emphasizing the modes of instabilities and the mode transition path in the cavitating flow. The vapor cloud shedding influence on the instability of the velocity vector field is studied, which sheds light on the intermittent and aperiodic transition between different shedding patterns. The data-driven analysis mentioned above displays the leading mechanisms that promote specific flow regimes: the imperative effect of attached sheet cavity instability, cavitation

inception, and condensation on the vapor cloud shedding pattern.

Additionally, POD analysis determines the kinetic energy transfer from the mean flow to the high-frequency modes. Similarly, the instantaneous energy exchange between different modes of instabilites is shown. Besides, the non-linear, chaotic and stability behavior of the POD time coefficients is investigated by looking into the LLEs. The global stability and short time behavior of the time signal of the POD energetic modes are extracted by observing the values of LLEs. The asymptotical behavior of the POD time dynamics is distilled to determine the long-term stability of the POD enegetic modes. Based on the understanding mentioned above, numerical and data-based models are introduced. The implicit objective of this research is to develop a generalizable and parsimonious mathematical model that can be employed for different geometries and flow conditions.

In the current research, the instantaneous pressure distribution in a Venturi-type test section is estimated using (TR-PIV) data and vapor volume fraction. Correspondingly, a numerical method using the Navier-Stokes equations has been developed to simulate snapshots of the pressure field of the cavitating flow. Firstly, a Poisson equation obtained from the conservative form of compressible momentum equation has been derived. Then, the Poisson equation is solved numerically for pressure through the Finite Difference Method (FDM).

The current experimental measurements of the cavitating flow imply that vapor and liquid phases are not in an equilibrium state. This behavior suggests that the thermodynamic saturation curves do not govern the phase transition. The mathematical presented in this research requires the incorporation of non-equilibrium thermodynamic effects by definition. The equilibrium conditions are assumed to be violated in the high void fraction regions, and a mass production(destruction) term is present in the continuity equation. Eventually, a mass transition field term governing the destruction or production of the vapor phase is

developed. It is assumed that the mass transition term is a function of the thermodynamic properties of the dynamical system, such as pressure, velocity vector field, speed of sound, and vapor volume fraction.

- Three-dimensionality: Although cavitating flow displays three-dimensional convection, the suggested models are developed in two-dimensional space.

- Unsteadiness: Cavitating flow depicts highly unsteady behavior owing to the strong inertial forces, even for a fixed uniform flow rate.

- Unsteadiness at the inlet and outlet of the boundaries: It is assumed that the pressure is uniformly distributed in the inlet and outlet of the test section, and unsteadiness has a negligible effect on the boundaries pressure fluctuations.

This dissertation demonstrates that the dynamical system is in a non-equilibrium state due to the phase transition phenomenon, e.g., destruction of the vapor. The deviation from equilibrium behavior of the current system begs some questions:

- How mass destruction(production) phenomenon is correlated to the kinetic and thermodynamic properties of the system?

- Can we describe physically the inception, break-up, and condensation of the cavitating flow relying only on the kinetic and thermodynamic properties of the current system?

- Does the condensation show a physically meaningful correlation with the thermodynamic properties of the system?

- Can we discover a transition field equation based on the kinetic and thermodynamic?

The present research has been implemented in the Propulsion and Multiphase Flow Labo-

ratory (PMFL) at Virginia Polytechnic Institute and State University.

Although the numerical cavitation models that have been discussed in the previous section have improved the estimation and simulations of the underlying physics of cavitating flow, the accuracy of the simulation of the unsteady cavitating flows can still be enhanced using data-driven techniques. As discussed in the previous sections, the cavitating models cannot predict some experimental observations: dynamics of the intermittent re-entrant jet, sheet cavity roll up and separation, quasi-periodic cloud shedding, condensation of the vapor cloud. Previous models proposed in the literature prescribe one governing equation for the entire problem domain where multiple physical mechanisms are observed in the experimental data. Since liquid-vapor phase transition and void transport are involved with distinct spatio-temporal scales, it is more realistic to suggest a combinatorial model that accommodates all features of the cavitating flow due to numerous physical mechanisms and flow conditions. The preceding combinatorial model combines different physical means of the void fraction transport, creation, and destruction using a blending function utilized to activate only a subset of the terms in the general governing equation depending on the location of the flow and the magnitude of the system variables or its corresponding derivatives. This method ensures that the appropriate terms representing the physical mechanism are in effect throughout the flow field. Besides, the local behavior of the dynamical systems can be described using the extraction of the dominant terms in the governing equations. Additionally, the dominant balance analysis of such a system has two key benefits: (1) improvement of our understanding of the physical behavior of the system in different region (2) extraction of the appropriate model for each flow condition.

1.4 Dissertation Blueprint

Chapter 2 presents an overview of the previous research on sheet cavitation and the corresponding physical aspects as it occurs on a Venturi-type test section. In this chapter, different techniques employed to study the dynamics of the cavitating flow have been introduced. Moreover, the advantages and disadvantages of each technique are discussed.

In Chapter 3, initially, the experimental test rig, including the hydraulic system and the test section geometry, are presented. Next, the imaging techniques applied to the cavitating flow, as it occurs in a Venturi-type test section, are discussed. Next, the post-processing techniques yielding the synchronous velocity and void fraction fields are presented.

In Chapter 4, the mathematical models for cavitating flow are developed. Initially, the continuity equation for the mixture is described. The continuity equation is numerically investigated to assess the thermodynamic state of the system. Then, the existing mathematical models for non-equilibrium cavitating flow are reviewed, and their shortcomings in predicting the production and destruction of the vapor phase have been investigated. Secondly, a decomposition scheme is suggested for the velocity vector field, which decorrelates distinct instabilities in the flow field, including the slow-varying drift flow, KH instabilities, and vapor-cloud shedding. In the next step, algorithms of DMD, POD, and CROM techniques are presented, and their applications on the cavitating flow are enumerated. Then, the momentum equations governing the homogeneous mixture of vapor and liquid phases are presented. A Poisson equation is derived using the compressible form of momentum equations to calculate the unsteady pressure field. Next, the numerical method used to obtain the pressure field is presented. The following section focuses on the derivation of the Favre-averaged Navier-Stokes equations and the technique dedicated to extracting the dominant balance physics in a generic compressible flow field. Finally, the data-driven phase

transition modeling method is presented.

Chapter 5 is dedicated to the verification and validation of the mathematical models. Simulation of the turbulent boundary layer over a flat plate is implemented. The simulation serves as a benchmark problem to validate the implementation of pressure reconstruction. Next, the simulation of the pressure field past the throat of the Venturi-type test section has been implemented. Besides, the instability mechanism that arises as a result of the pressure gradient distribution is investigated. Last but not least, the uncertainty level in the computations of the pressure field is shown.

Chapter 6 deals with the results obtained from the data-driven techniques revealing the instability modes as it occurs in a Venturi-type test section. In the first step, distinct shedding regimes are defined and further linked to the physics of flow that is used to extract the underlying mode change path in the cavitating flow. Mode shifting and intermittency phenomena are further investigated for a single fixed inlet flow condition using the CROM technique. Besides, DMD yields the instability modes of the sheet cavity and cloud shedding. Similarly, POD analysis shows that the velocity vector field is composed of distinct instabilities: instability due to the slow-varying drift, KH instabilities, and high-frequency vapor-cloud shedding. Then, it has been shown that the instantaneous velocity vector field can be reconstructed by combining the instabilities mentioned above.

In chapter 7, the local behavior of the cavitating flow is investigated. Firstly, the terms in the TKE equation are obtained; then, Understanding the path of the kinetic energy of the mean flow role and the importance of each term in the TKE equation is defined. In this regard, the mechanisms of transfer of the kinetic energy of the mean flow to the fluctuating component of the velocity and internal energy of flow were studied. Besides, the efficient mechanisms transporting the TKE in the cavitating flow are extracted. In the following sections, the

flow field domain is clustered using GMM; the dominant terms in the momentum equation in each cluster are identified.

In chapter 8, the mass transition between vapor and liquid phases is obtained using a data-driven technique and the void fraction transport equation. Next, the underlying physics of phase transition is discussed. In this regard, the role of each term in the phase transition process is highlighted. Finally, the flow field domain is segmented using GMMs, and the dominant mechanisms causing vapor-liquid phase transition are distilled in each cluster.

Chapter 2

Dynamics of the Unsteady Sheet Cavity and Vapor Cloud

2.1 Sheet Cavitation on a Venturi-type Section

This research focuses on the cavitating flow as it occurs past the throat of the Venturi-type section. Depending on the experiment operating status, one of the several types of cavitation occurs: sheet-cavitation, attached sheet cavitation, and cloud cavitation.

Since the pressure drops past the throat, the vapor sheet emerges at the bottom surface of the test section. Correlation of the length scale of the vapor sheet with cavitation and Reynolds numbers have been investigated in the literature [48]. Besides, cavitation evolution on a Venturi-type test section has been explained by [48, 59]. They identified four types of cavitation patterns:

- Type 1: Attached vapor cavitation instability results in periodical separation of the vapor clouds, and they eventually collapse downstream. Significant oscillation in the length of the sheet cavity is observed. The type 1 cavitation pattern is illustrated in figure 2.1.

- Type 2: Clusters of bubbles separate from the leading edge of the sheet cavity.

- Type 3: An attached sheet cavity is created, and its length oscillates significantly. The type 3 cavitation pattern is shown in figure

- Type 4: An attached sheet cavity is fully developed, and a small oscillation in its size is observed. 2.2.

The pattern of the cavitation concerning the changes in cavitation number has been studied by [48]. With an increase in the cavitation number at a fixed Reynolds number, the cavitation pattern may change from a highly unstable case, e.g., type 1, to a comparatively less unstable case, type 2 or 3. Further increases in the cavitation number result in a small attached sheet cavity with negligible length oscillations. For all Reynolds numbers, small-scale oscillations of the sheet cavity are observed. Besides, the Reynolds number has an insignificant effect on the Strouhal number, which means that increasing the Reynolds number does not significantly affect the cavitating behavior.

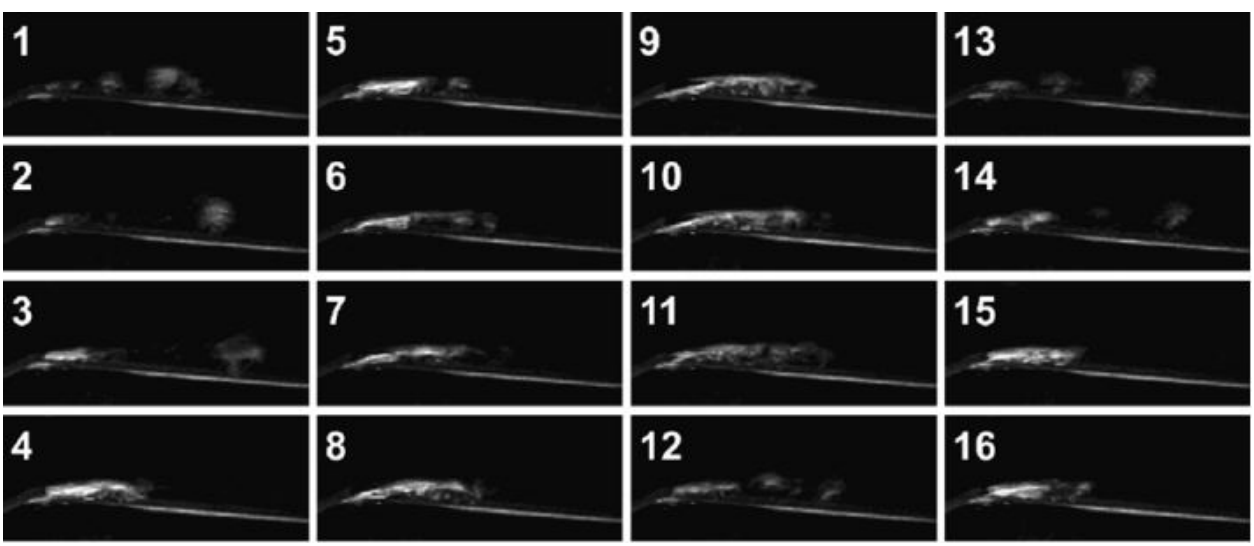

Figure 2.1: Sheet cavity evolution, vapor shedding, and cloud collapse in sequential frames captured from the cavitatig flow past the throat of the Venturi-type section at $U_\infty = 9m/s$, $\sigma = 0.96$, and $Re = 4.44 \times 10^4$ [48]. The throat width and height are $3.6mm$ and $10.8mm$, respectively.

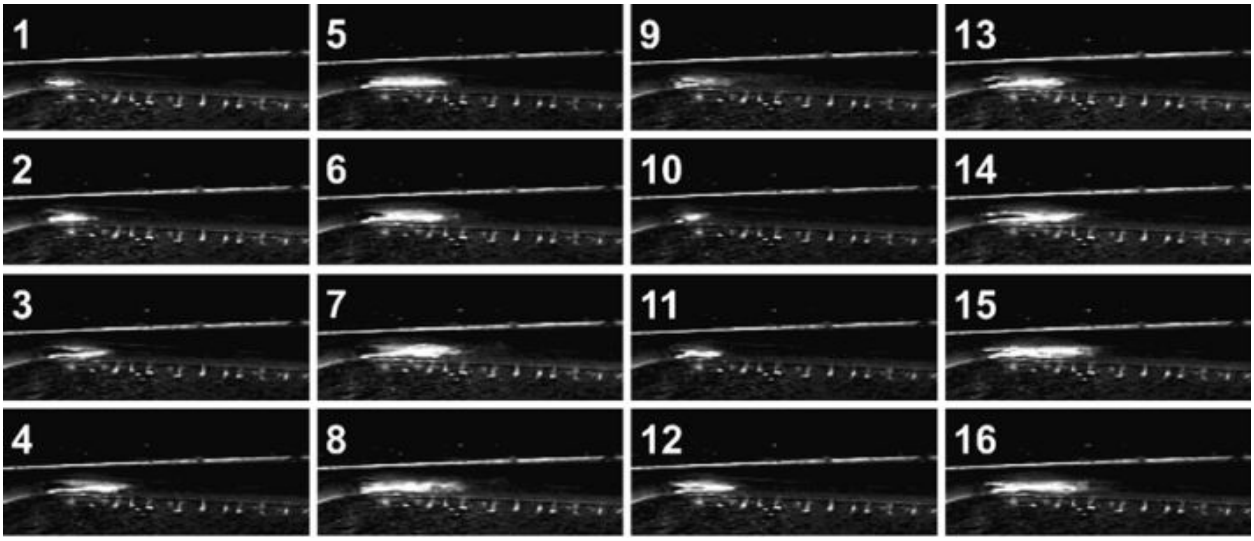

Figure 2.2: The typical sequence for the evolution of the sheet cavity and oscillation of its length [48]. In this case, no cloud shedding is observed. The flow condition is similar to cavitation evolution illustrated in figure 2.1 . The throat width and height are $6.7mm$ and $2.7mm$, respectively.

Dular et al. [48] utilized six test sections characterized by different sizes. They found a unique curve for each Reynolds number, relating the non-dimensional length of the sheet cavity with the cavitation number. Changing the length of the cavity sheet by varying the size of the test section found an almost linear dependence of the length of the sheet on the cavitation number. They also found that for their test sections the Strouhal number at which the sheet cavity was shed depends on cavitation number and test section sizes.

Since the vapor sheet is formed due to a strong adverse pressure gradient, the streamlines tend to be close to each other in the vicinity of the liquid-vapor interface. At the closure region of the sheet cavitation, a liquid jet is formed. The liquid jet may travel upstream and impinge on the interface of the sheet cavity. On the other hand, part of the jet may reattach to the wall. Depending on the inertial forces, the re-entrant jet may travel a longer or shorter distance. The departure mentioned above results in separating the vapor clouds that occur aperiodically depending on the system parameters, such as Reynolds number and

cavitation number. The separation of the clouds leaves a highly vortical flow pattern as the main flow convects it. This circulation is carried downstream as the vapor cloud is traveling. Since the downstream pressure recovers, the vapor structures start to break up into smaller structures and it gradually condensates as the vapor travels downstream. Cavitating vortices are formed as a result of the vapor structure condensation and vortical structures eventually disappear in the high pressure regions. Meanwhile, the sheet cavity length is recovered and a new liquid jet is formed at the tip of the sheet. This quasi-periodic phenomenon is governed by the non-linear inertial terms, and depending on the experimental condition may yield periodic behavior as well.

2.2 Dynamics of the Vapor Sheet on Venturi-type Section

Dular et al. [48] carried out experiments for Venturi-type test sections in unsteady conditions in the small cavitation tunnel VenturiX of the LML Laboratory (Lille, France). Their focus was to generate sheet cavities with distinct length scales to investigate their effect on the cavitating flow and vapor cloud dynamics. In figure 2.1, the process of sheet cavity evolution, vapor shedding, and cloud collapse are depicted. The shedding is defined as periodic, and two characteristics frequencies, associated with shedding frequency and the fluctuations of the sheet cavity, are introduced. Figure 2.3 depicts the maximum length of the attached cavity. Dular et al. [48] showed that the sheet cavity geometry is correlated to dynamics of the re-entrant jet, and it further determines the shedding mechanism of the sheet. Due to the small throat height, the liquid jet's influence on the sheet cavity is insignificant, and because of momentum deficit, the jet is convected by the main flow. Corresponding to the previous research, Callenaere et al. [50] observed that a thin sheet cavity does not oscillate

in length. Dular et al. [48] linked this behavior of the sheet cavity to its thickness. If the sheet cavity is thin, at the closure of the vapor sheet, a liquid jet is developed that interacts with the thin cavity. They suggested that the liquid jet loses its momentum due to the interaction mentioned above. They concluded that the liquid jet penetrating the main flow requires more energy.

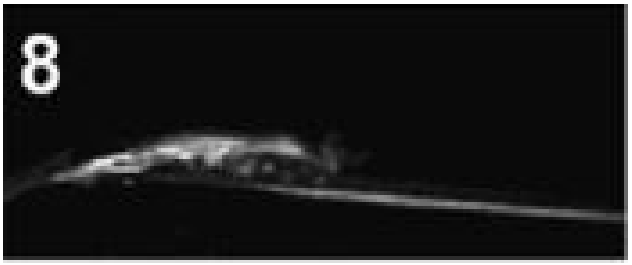

Figure 2.3: Frame # 8 depicting the maximum length acquired by the attached sheet cavity [48]. For further information of the section geometry and flow, condition look at figure 2.1

The re-entrant jet flows toward port or starboard sides; consequently, it collides with one of the walls. At this location, the re-entrant jet 'cuts' the sheet cavity and changes the cavity from a smooth vapor sheet into a separated cloud region. The jet leaves the attached cavity tip with a sharp angle, thereby cutting a big chunk of the sheet cavity. The vapor cloud is convected by the main flow and goes through condensation in the region with higher pressure on the downstream of the throat; look at figures 2.5. In the final images of the collapse of the vapor cloud, downstream vortical structures of vapor are observed that coalesce before the condensation, look at figures 2.6. In figures 2.7 a single but larger-scale upstream vortical structure is formed due to re-entrant jet. This structure, presumably created by the collision of the re-entrant jet with the sidewalls, can be observed in figure 2.4. This observation shows that the shedding of vapor clouds may lead the dynamical system to a quasi-periodic phenomenon.

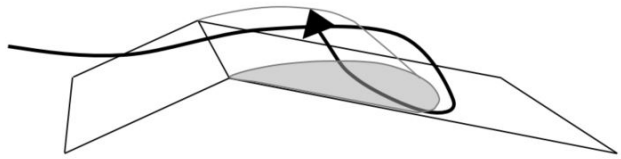

Figure 2.4: Cavitation in a comparatively wide test section at $U_\infty = 9m/s$, $\sigma = 0.96$, $Re = 3.48 \times 10^4$ [48]. The throat width and height are $15mm$ and $2.7mm$, respectively. Depiction of the collision of the re-entrant jet with the side walls due to the re-entrant jet sharp angle.

Figure 2.5: Representation of the condensation of the cloud cavity on the downstream [48]. For further information on the section geometry and flow condition, look at figure 2.1.

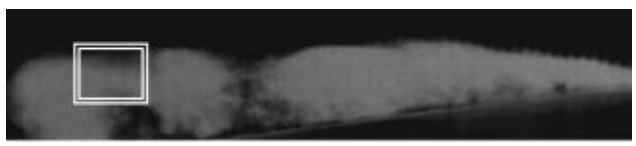

Figure 2.6: Coalescence of the vapor cloud structures in the downstream [48]. The prescribed flow condition is $U_\infty = 17m/s$, $\sigma = 0.98$ and $Re = 8.09 \times 10^4$. For further information of the section geometry look at figure 2.6.

Figure 2.7: Single large-scale cloud convection on the downstream [48]. For further information of the flow conditions and the section geometry look at figures 2.6 and 2.1, respectively

Dular et al. [48] showed that the throat height and width of the test section determines the vapor shedding mechanism. To distinguish between cloud cavitation and partial, intermittent

shedding, Dular suggested that the test section's small height prevents further progression of the re-entrant jet, thereby inducing low-frequency oscillations of the sheet cavity. This jet has a weak side-wise velocity that prevents it from reaching the wall. They used the term jet's 'premature stop' for the case that the direction of the jet exiting the attached cavitation area is not perpendicular to the flow above the cavity, and its corresponding angle is not sharp, so the jet may not reach out to the wall.

2.3 The Collapse of the Cloud Cavitation

The attached sheet cavity break-up leads to vapor clouds. The vapor cloud is a highly vortical region and introduces turbulent fluctuations due to high shear stress. Transportation of the vapor cloud to the regions with high pressure causes the collapse of the cloud. It has been observed that the destruction of the clouds results in intense pressure pulses [27]. During this process, the system's boundary, e.g., the Venturi bottom wall, experiences an unsteady loads that might be the main reason for the cavitation erosion and noise production. In the study of the dynamics of cloud collapse, It is imperative to assume that the flow field is compressible.

In the literature, the collapse of an isolated bubble has been studied both theoretically and experimentally. Experimental observations on the destruction of an isolated bubble and cloud cavitation suggest that the pressure pulses amplitude may reach 100 bar, Fujikawa & Akamatsu [24]. In an experimental investigation, Reismann et al. [26] studied the breakup and the collapse of sheet and vortex cavities. In this study, pressure pulses on the surface have been captured. They explained that the shock dynamics result in damage to the surface and cause noise in cavitating flow. The collapse of the bubble is employed in medical applications as well [71]. The shock wave caused by the cloud cavitation was utilized for Lithotripsy. It

has been observed that unsteady pressure pulses can destroy kidney stones. In a numerical investigation, Johnson and Colonius [41] studied the breakup of kidney stones exposed to the shockwave.

Schmidt et al. [67] numerically estimate the inception and transport of shocks and rarefaction waves corresponding to the collapse of vapor in a cavitating flow. The preceding compressible flow simulation causes unsteady loads on the boundaries. Coutier-Delgosha et al. [54] showed that the periodical behavior is dictated by pressure waves caused due to the collapse. They suggested that the backpropagation of the intense pressure wave delays the growth of the cavity that in turn reduces the cycle frequency significantly.

Chapter 3

Experimental Design and Measurement Techniques

3.1 Experimental Set-up

The experiments are conducted in a Venturi-type test section installed on a closed-loop hydraulic test rig designed by Coutier-Delgosha et al. [55], figure 3.1. The flow rate is controlled by a frequency variator connected to a circulating pump. The re-circulation loop is assigned to maintain a small flow rate preventing the pump from operating in unstable conditions. The reference pressure at the inlet and outlet of the loop is adjusted by a vacuum pump connected to the free surface of the tank.

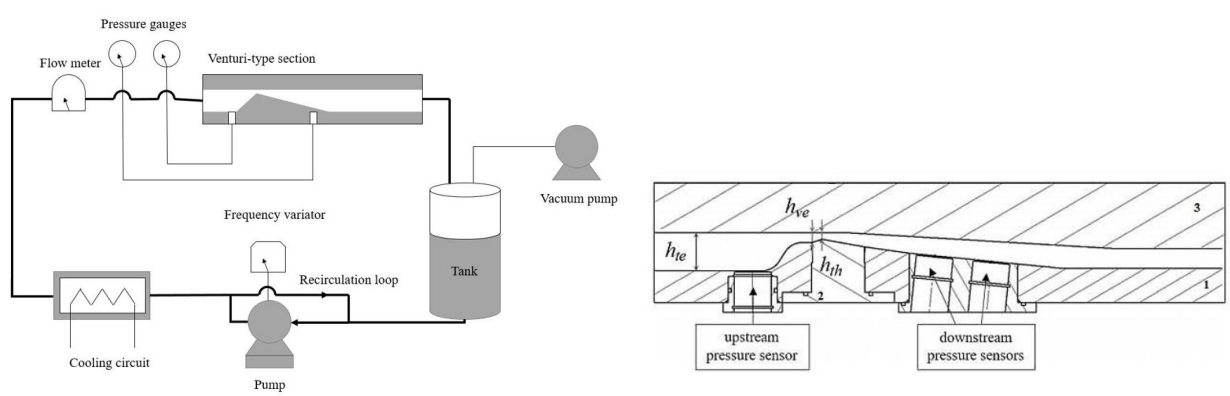

Figure 3.1: (a) Schematic diagram of the test rig. (b) Venturi type test section profile; the confining bottom (2) and top (3) walls leaving the channel with a convergent wedge at the entrance and a divergent one toward the outlet. The flow is from left to right

The Venturi test section is presented in Figure 3.1. The Venturi-type section is formed through two walls, labeled (1) and bottom wall labeled (3), then part (2) is inserted in a gap on the bottom wall to confine the flow in the channel. The confining part leaves the Venturi section with a converging angle of 18° at the inlet and a divergent angle of 8° at the outlet. The width of the channel is $4mm$. At the entrance, a contraction ratio of 1.1 connects the inlet to the throat. The height at the entrance of the Venturi, h_{ve}, is $17mm$ and the height at the throat of Venturi, h_{th}, is $15.34mm$. The height at the entrance of the test section, h_{te}, is $31mm$. The thickness of each plexiglass side wall is as small as $0.5mm$. Two pressure gauges are installed on the bottom wall of the test section. The pressure sensors work in a range of 0-3 bar with a full-scale uncertainty of 0.25%. The upstream pressure gauge value determining the pressure at the inlet is utilized to compute the cavitation number. The relative cavitation intensity is indicated through cavitation number. The cavitation number σ_{cav} is the ratio of the local static pressure difference from the vapor pressure to the dynamic pressure:

$$\sigma_{cav} = \frac{p_o - p_v}{\frac{1}{2}\rho_w u_{inlet}^2} \tag{3.1}$$

Where p_o is the static pressure at the upstream and p_v is the vapor pressure, ρ_w is the density of the liquid phase, and u_{inlet} is the inlet time-averaged velocity. The inlet time-averaged velocity is computed using the flow rate measured by a flow meter with a reading uncertainty of 2% and installed before the entrance of the Venturi. The Reynolds number presents the ratio between the inertial forces over viscous forces. The Reynolds number based on the height of the Venturi section throat may be defined as follows:

$$Re_h = \frac{u_{inlet} h_{th}}{\nu_w} \tag{3.2}$$

ν_w is the kinematic viscosity of water. The primitive uncertainty obtained from the pressure gauge and the flow meter leads to a derived uncertainty of 3.5% in the cavitation number. Table 3.1 has listed some of the most important system parameters.

Table 3.1: Some important system parameters

Symbol	Description	Value
$f_{St}(Hz)$	frequency of the Strouhal number	138
$l_{SC}(mm)$	length of the attached sheet cavity	23.5
St	Strouhal number	0.21
$u_{inlet}(\frac{m}{s})$	Inlet velocity	15
$t_{St}(ms)$	period of the Strouhal number	7.25

3.2 PIV High-speed Photography

The raw images of cavitating flow in the Venturi section were captured from the side view. In this experiment, two cameras are located on both sides of the test section, figure 3.2. A FASTCAM SA1.1 camera with a Tokina 100mm lens is used to capture the images of the seeding particles, the camera on the left-hand side. This camera is equipped with a notch filter to transmit most wavelengths with little intensity loss while attenuating light within the laser light sheet wavelength range. In all campaigns, the field of the first camera view was 1024 $\times$ 1024 pixels, with each pixel corresponding to 20 m. A VEO 710L camera, installed on the right-hand side, is equipped with a density filter recording the dynamics of the vapor phase. A density filter has been utilized to alleviate the over-illumination of the vapor phase on the sensor of the second camera. A laser light sheet with the maximum thickness of 1.5 mm has been created in the middle of the test-section span by an Nd: YLF

Laser (Neodymium-doped yttrium lithium fluoride) operating at 2.4 kHz with a wavelength of 527 nm. Rhodamine B fluorescent dyes were injected into the flow and illuminated by the laser light sheet. A double pulse laser beam yields a pair of consecutive images of the illuminated particles. Time duration between two consecutive images, dt_{beams}, is 10μ. The PIV set-up is presented in figure 3.2.

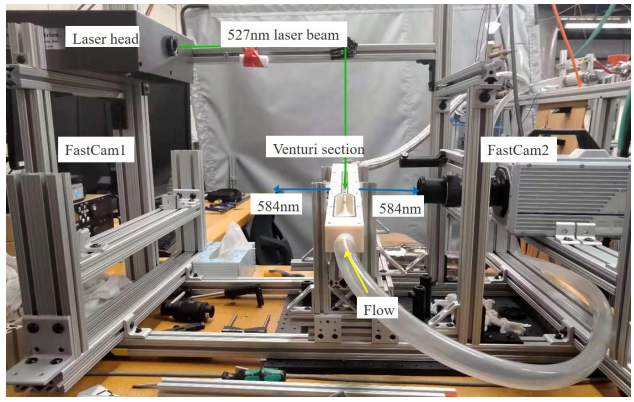

Figure 3.2: PIV system apparatus in the front view of the Venturi section showing the Nd: YLF laser, the laser beam, VEO 710L, and FASTCAM SA1.1 cameras, density and notch filters, reflecting mirrors, and flow direction. The flow is from left to right. For further information of the test rig look at figure 3.1.

3.3 PIV Measurements

Velocity vector field was resolved using a high-speed Particle Image Velocimetry (PIV). The instantaneous velocity field of the liquid phase is evaluated through the cross-correlation algorithm. Next, outlier vectors are detected and then replaced by a bi-linear interpolation applied to the high-fidelity neighboring vectors. A cross-correlation algorithm was applied to each pair of images to determine the instantaneous liquid phase displacements. Computations were carried out using DaVis 8.3 from LaVision. The number of images that are acquired is 2500 yielding one second of data. A multi-pass algorithm has been employed where the first pass is performed with an interrogation window size of 64×64 and a 50%

overlap. The final pass was performed with 16×16 window size and overlap of 50%. An overview of the PIV parameters applied to high-speed photography is presented in Table 3.2. The uncertainty in liquid phase velocity measurements was estimated. The results indicated an error of approximately 3% of the reference velocity for the liquid phase.

Table 3.2: Overview of the relevant PIV parameters applied to the raw images obtained from the high speed photography.

	reconstruction method	PIV
Interrogation window parameters	interrogation area, initial pass (Pixel × Pixel)	64×64
	number of passes	2
	interrogation area, final pass (Pixel × Pixel)	16×16
	overlap interrogation area	50%
	interrogation window-shape	Square
	Deformation of the interrogation window	Asymmetric shift:
		Applied on the second frame only

3.4 X-ray Imaging

Zhang et al. [30] conducted the X-ray experiments at the Advanced Photon Source (APS). A high-energy and spatially coherent X-ray has been employed. Figure 3.3 depicts the X-ray source aligned with the test section on the left-hand side, and the X-ray detector, a scintillator, is on the right-hand side. The scintillator converts the X-ray beam into visible light, recorded by the high-speed CCD camera. The X-ray source sends out two pulses: the primary pulse has a $500ns$ duration, and the second pulse has a $10ps$ duration. The aperture of the X-ray source is $1.7 \times 1.3mm^2$. The time interval between the primary and secondary X-ray pulses is $3.68\mu s$. The X-ray source is located at a distance of about $60m$ from the test section. The distance between the object and the detector is $50cm$ to enhance the phase contrast. Figure 3.3 depicts the synchronization between the X-ray flashes, the fast shutter, and the camera. The synchronization enhances images used for PIV analysis. The

acquisition frequency of the camera is $12,070$ fps, and the corresponding spatial resolution of 704×688 $pixel^2$ with a pixel size being $2\mu m$.

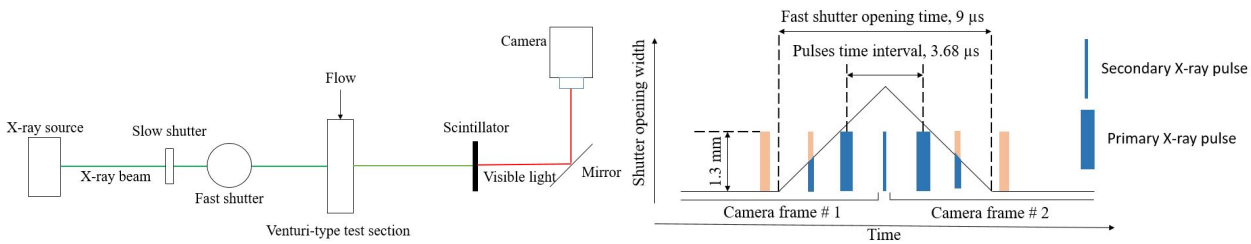

Figure 3.3: (a) Schematic diagram of X-ray light source located at the APS composed of the X-ray light source, X-ray beam, slow and fast shutters, test section, scintillator, and camera [30]. (b) diagram of the X-ray pulse duration, x-axis, versus shutter opening width, y-axis. The fast shutter time during, $9\mu m$, accommodates a pair of camera frames used to implement PIV analysis. The first (second) camera frame detects the primary (secondary) X-ray pulse that creates the image pair for the PIV analysis.

Silver-coated hollow glass spheres with an average diameter of 10 and 17 μm are used as the tracers of the liquid phase. Since the cross-section of the X-ray beam is small compared to the cross-section of the test section, the complete image for the flow field is broken into individual windows shown in figure 3.4. Successive but not simultaneous acquisitions at different windows are implemented at each measurement campaign. For each campaign, the test section was moved parallel to the divergent wall of Venturi and perpendicular to the X-ray beamline by a mobile platform. At each position, $1,872$ images were recorded. Figure 3.4 shows a raw X-ray image of cavitation flow at the second position. Since the tracer particles and the vapor structures are both captured clearly, the imaging enables simultaneous study of the liquid phase and vapor phase.

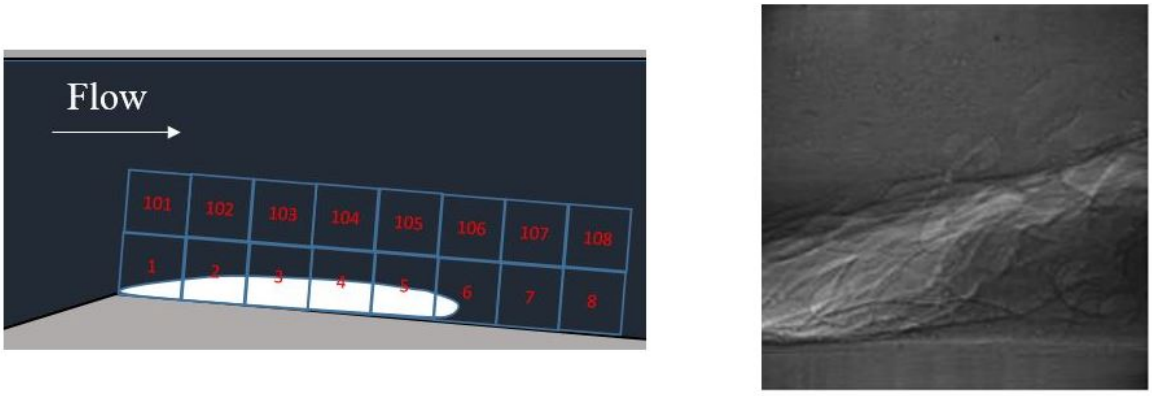

Figure 3.4: (a) Schematic of X-ray scanning positions [30]. Position # 1 is located adjacent to the throat of the Venturi-type section where the cavitation inception is observed. In each campaign, the test section is moved to the new position to complete the data acquisition. (b) An X-ray image of the cavitating flow at window # 2 illustrates the silver-coated hollow glass spheres overlaid with the vapor structures.

Chapter 4

Mathematical Models and Data-driven Techniques

4.1 Non-equilibrium Models

In the present research, we have investigated and further assessed non-equilibrium models for cavitation. Here it is assumed that the density of the liquid and vapor phases are constant. It is also assumed the temperature remains constant. In this section, we present several non-equilibrium models.

It is generally assumed that the pressure and temperature of the liquid and vapor phases are different, taking into account the non-equilibrium condition. In this case scenario, the system's status cannot be identified by the thermodynamic saturation curves. Typically, one may show that the conservation of mass equation is as follows:

$$\frac{\partial(\alpha\rho_v)}{\partial t} + \frac{\partial(\alpha\rho_v u)}{\partial x} + \frac{\partial(\alpha\rho_v v)}{\partial y} = \dot{m}_v \tag{4.1}$$

Where $\dot{m}_v$ is the mass transfer source term for the vapor phase. Eq. (4.1) defines the mass transformation in the term of vapor mass change. This equation makes it feasible to consider the non-equilibrium processes. Kunz et al. [60] modeled mass transfer term using empirical

mass transfer rates of Merkle et al. [16]. Mass transfer rate of vapor phase $\dot{m}_v$ is assumed to consist of a source and a destruction term. The source (destruction) term is responsible for the transition of the liquid (vapor) mass to the vapor (liquid) mass. The mass transfer term can be written as follows:

$$\dot{m}_v = C_{Prod}\frac{\rho_v(1-\alpha)}{\frac{1}{2}\rho_l U_\infty^2 t_\infty} min(0, p - p_{sat}) - C_{dest}\frac{\rho_v(1-\alpha)^2\alpha}{t_\infty} \tag{4.2}$$

The transition of the liquid to vapor is assumed to be correlated to the liquid volume fraction, $1-\alpha$, and the difference of the static pressure with the saturation pressure. C_{prod} is an empirical constant, U_∞ is the mean flow velocity and $t_\infty = \frac{U_\infty}{c}$ is a mean flow time-scale. The transition of the vapor phase to the liquid phase is correlated to the volume fraction of the vapor and liquid phases [60]. C_{dest} is an empirical constant. Merkle et al. [16] assumed that liquid density changes are proportional to the dynamic pressure:

$$|p_{sat} - p| = \frac{\kappa\rho_\infty U_\infty^2}{2} \tag{4.3}$$

Where κ is an arbitrary parameter having a value between 0.2 to 0.5, the assumptions mentioned above imply that their model considers the compressibility of the flow. Besides, Merkle et al. [16] took into account the time scale of the flow motion:

$$t_\infty = \frac{d}{U_\infty} \tag{4.4}$$

The corresponding time scale allowed them to evaluate the required time for the transition from one phase to another.

A void ratio transport equation is suggested by Saurel et al. [57] and later by Charrière et al. [13] that can be expressed as follows:

$$\frac{\partial \alpha}{\partial t} + \frac{\partial(\alpha u)}{\partial x} + \frac{\partial(\alpha v)}{\partial y} = (K + \alpha)(\frac{\partial u}{\partial x} + \frac{\partial v}{\partial y}) + \frac{\dot{m}_v}{\rho_I} \tag{4.5}$$

Another popular method to define the transition of the vapor to the liquid phase is given by Eq. (4.5) Where K and ρ_I are defined as follows:

$$K = \frac{\rho_l c_l^2 - \rho_v c_v^2}{\frac{\rho_l c_l^2}{1-\alpha} + \frac{\rho_v c_v^2}{\alpha}} \tag{4.6}$$

$$\rho_I = \frac{\frac{\rho_l c_l^2}{1-\alpha} + \frac{\rho_v c_v^2}{\alpha}}{\frac{c_v^2}{\alpha} + \frac{c_l^2}{1-\alpha}} \tag{4.7}$$

Goncalvès [29] assumed that the mass transition is correlated to the velocity divergence. In this case scenario, the destruction (source) term is responsible for vapor volume decreases (increases).

$$\dot{m}_v = \frac{\rho_l \rho_v}{\rho_l - \rho_v}(1 - \frac{c^2}{c_{wallis}^2})(\frac{\partial u}{\partial x} + \frac{\partial v}{\partial y}) \tag{4.8}$$

Where c_{wallis} is the propagation velocity of acoustic waves without mass transfer [76]. This speed of sound is expressed as a weighted harmonic mean of the speed of the sound of each phase:

$$\frac{1}{\rho c_{wallis}^2} = \frac{\alpha}{\rho_v c_v^2} + \frac{1-\alpha}{\rho_v c_l^2} \tag{4.9}$$

This model takes into account a correlation between sound speed and the thermodynamic equilibrium.

Rayleigh [58] developed a mathematical model of the cavitation process in an incompressible flow. This mathematical model assumes that the surface tension and viscosity effects are negligible in the cavitation process.

The well-known Rayleigh–Plesset equation governing the dynamics of a spherical bubble in an incompressible flow is expressed as follows:

$$R\frac{d^2R}{dt^2} + \frac{3}{2}(\frac{dR}{dt})^2 = \frac{p_{sat} - p}{\rho_l} - \frac{2\sigma}{\rho_l R} - 4\frac{\mu_l}{\rho_l R}\frac{dR}{dt} \tag{4.10}$$

Inspired by Rayleigh, Schnerr, and Sauer [66] developed a transport-based cavitation model. Their model takes into account the dynamics of the bubble growth:

$$\dot{R} = \frac{dR}{dt} = \sqrt{\frac{2}{3}\frac{(p - p_{sat})}{\rho_l}} \tag{4.11}$$

The initial value of bubble radius, R, was set to 3×10^{-5}.

Source terms of their model are expressed as follows:

$$\dot{m}^+ = \frac{\rho_v \rho_l}{\rho_m}\alpha(1-\alpha)\frac{3}{R}\sqrt{\frac{2}{3}\frac{(p - p_{sat})}{\rho_l}} \tag{4.12}$$

$$\dot{m}^- = \frac{\rho_v \rho_l}{\rho_m}\alpha(1-\alpha)\frac{3}{R}\sqrt{\frac{2}{3}\frac{(p_{sat} - p)}{\rho_l}} \tag{4.13}$$

The transport equation of the model requires no empirical constants and depends only on quantitative values of the physical parameters.

Based on the Rayleigh-Plesset equation, Iben [33] developed a source term as follows:

$$\dot{m}^{+} = C_{prod}\rho_v \frac{6\alpha}{2R}\sqrt{\frac{2}{3}\frac{p - p_{sat}}{\rho_l}} \tag{4.14}$$

$$\dot{m}^{-} = -\rho_v \frac{6\alpha}{2R}\sqrt{\frac{2}{3}\frac{p_{sat} - p}{\rho_l}} \tag{4.15}$$

In this model, an empirical constant determines the rate of condensation, and other terms are physical parameters. Iben's model is primarily used to simulate cavitation in throttles and nozzles in two-dimensional geometries.

Singhal et al. [3] formulated the cavitation source term as follows:

$$\dot{m}^{+} = C_{prod}\frac{\sqrt{k}}{\sigma}\rho_l\rho_l\sqrt{\frac{2}{3}\frac{(p - p_{sat})}{\rho_l}}f_v \tag{4.16}$$

$$\dot{m}^{-} = -C_{dest}\frac{\sqrt{k}}{\sigma}\rho_l\rho_v\sqrt{\frac{2}{3}\frac{(p_{sat} - p)}{\rho_l}}(1 - f_v - f_g) \tag{4.17}$$

Source terms of Singhal et al. [3] are assumed to be correlated to the surface tension, ($\sigma = 0.0717\ \frac{N}{m}$), turbulence kinetic energy, and the content of non-condensable gasses in the liquid ($f_g \approx 10$). The vapor mass fraction can be obtained as follows:

$$\alpha = f_v \frac{\rho_m}{\rho_v} \tag{4.18}$$

Frobenius [49] developed a model similar to Schnerr and Sauer [66]. The source terms of the Frobenius model have the following forms:

$$\dot{m}^+ = C_{prod} \frac{\rho_v \rho_l}{\rho_m} \alpha (1-\alpha) \frac{3}{R} \sqrt{\frac{2}{3} \frac{(p - p_{sat})}{\rho_l}} \tag{4.19}$$

$$\dot{m}^- = -C_{dest} = \frac{\rho_v \rho_l}{\rho_m} \alpha (1-\alpha) \frac{3}{R} \sqrt{\frac{2}{3} \frac{(p_{sat} - p)}{\rho_l}} \tag{4.20}$$

Frobenius et al. [49] implemented two- and three-dimensional steady and unsteady flow simulations around a hydrofoil and steady simulations for flow past the centrifugal pump impeller.

Saito et al. [79] for the first time suggested a model based on the mass surface change. In this model the mass source unit is not $\frac{kg}{m^3 s}$, instead it is $\frac{kg}{m^3 s}$. To define the interfacial area concentration in the vapor-liquid mixture, Saito et al. [79] utilized a new variable A:

$$A = C_a \alpha (1-\alpha) \tag{4.21}$$

The source terms of Saito et al. are expressed as follows:

$$\dot{m}^+ = C_{prod} A \alpha (1-\alpha) \frac{p - p_{sat}}{\sqrt{2\pi R_1 T_{sat}}} \tag{4.22}$$

$$\dot{m}^- = -C_{dest} A \alpha (1-\alpha) \frac{\rho_l}{\rho_v} \frac{p_{sat} - p}{\sqrt{2\pi R_1 T_{sat}}} \tag{4.23}$$

The relationship between all constants is expressed as follows:

$$C = C_p C_a = C_d C_a \tag{4.24}$$

The value of the empirical model constant C is set to $0.1\frac{1}{m}$. Saito et al. assessed the fidelity of their model in prediction of cavitation region in unsteady three-dimensional cavitating flows over a hemisphere and a cylinder. Furthermore, they employed their model in the two-dimensional simulations of an unsteady flow past a hydrofoil.

Zwart et al. [56] proposed source terms of the model as follows:

$$\dot{m}^+ = C_{prod} \frac{3\alpha\rho_v}{R} \sqrt{\frac{2}{3} \frac{p - p_{sat}}{\rho_l}} \tag{4.25}$$

$$\dot{m}^- = -C_{dest} \frac{3\rho_v (1-\alpha)\alpha_{nuc}}{R} \sqrt{\frac{2}{3} \frac{p_{sat} - p}{\rho_l}} \tag{4.26}$$

This model has a similar form as of Iben's model [33]. Nucleation site of volume fraction α_{nuc} is set to 5×10^{-4}. This model has been employed to simulate three-dimensional unsteady cavitating flows. Zwart et al. [56] used the model to simulate and analyze the cavitating flow around a hydrofoil. They also presented the results of the simulation of the cavitating flow past an inducer and a Venturi-type section.

Huang and Wang [8] suggested a new method of mass transition from the liquid phase to

vapor phase:

$$\dot{m}^{+} = \chi(\frac{\rho_m}{\rho_l})\dot{m}_Z^{+} + (1 - \chi(\frac{\rho_m}{\rho_l}))\dot{m}_S^{+} \tag{4.27}$$

$$\dot{m}^{-} = -\chi(\frac{\rho_m}{\rho_l})\dot{m}_Z^{-} + (1 - \chi(\frac{\rho_m}{\rho_l}))\dot{m}_S^{-} \tag{4.28}$$

In this model the blending function $\chi(\frac{\rho_m}{\rho_l})$ is described as:

$$\chi(\frac{\rho_m}{\rho_l}) = 0.5 + \frac{tanh[\frac{C_1(\frac{0.6\rho_m}{\rho_l} - C_2)}{0.2(1-2C_2)+C_2}]}{[2tanh(C_1)]} \tag{4.29}$$

The author combined the blending function with the expressions of source terms of Zwart [56] and Schnerr and Sauer [66]. The values of the model constants C_1 and C_2 are set to 4 and 0.2. Huang and Wang [8] evaluated the performance of their model for unsteady flows around a hydrofoil.

Konstantinov et al. [70] proposed an equation to solve the instability problem of the Rayleigh-Plesset equation. They emphasized that this equation describes the bubble dynamics with better accuracy and imposes no effect on the computational stability. Taking into account the effect of the Reynolds number on the radius of the bubble, they derived the following equation describing the dynamics of the bubble:

$$\frac{dR}{dt} = tanh[1.221(\frac{R\sqrt{|p_{sat} - p|\rho_m}}{4\mu})^{0.353}]\sqrt{\frac{2}{3}\frac{|p_{sat} - p|}{\rho_l}} \tag{4.30}$$

Konstantinov et al. [70] combined their new bubble dynamic equation with the source terms

suggested by Zwart et al. [56] and obtained revised source terms as:

$$\dot{m}^{+} = C_{prod}\frac{3\alpha\rho_v}{R}tanh[1.221(\frac{R\sqrt{|p_{sat}-p|\rho_m}}{4\mu})^{0.353}]\sqrt{\frac{2}{3}\frac{|p_{sat}-p|}{\rho_l}} \tag{4.31}$$

$$\dot{m}^{-} = -C_{dest}\frac{3\rho_v(1-\alpha)\alpha_{nuc}}{R}tanh[1.221(\frac{R\sqrt{|p-p_{sat}|\rho_m}}{4\mu})^{0.353}]\sqrt{\frac{2}{3}\frac{|p-p_{sat}|}{\rho_l}} \tag{4.32}$$

This section briefly reviewed the various numerical models expressed in the literature to simulate the response of the single bubble and vapor structures to the pressure field. The following characteristics, assumptions, and challenges of some of the preceding cavitation models are explained. The first homogeneous transport model is the Rayleigh-Plesset equation, which obtains the dynamics of a single bubble. This model considers the effects of the surface tension and viscosity on the radius of the bubble. One of the Rayleigh-Plesset model problems is that it cannot describe the dynamics of the vapor structures accurately.

Cavitation models proposed by Merkle et al. [16], Kunz et al. [60], Singhal et al. [3], Saito [79] address the destruction, production, expansion due to merging, compression, and phase transition processes. They suggested that the processes mentioned above depend on the semi-empirical relation between the pressure difference between the static pressure and the vapor saturation pressure. Fundamentally, these models assume that the vapor-liquid interface is in equilibrium condition. The results dependence on the semi-empirical constants is the major problem with these models. Since numerous cavitation regimes are observed in different regions of the flow field, the calibration of the model in the distinct regions has remained a challenging objective.

Assuming that the bubble expansion is occurring in a controlled inertia regime, Schnerr and

Sauer [66] solved the simplified form of Rayleigh–Plesset equation. Negligible acceleration results in an explicit relationship between the interface radial velocity with the pressure difference. Schnerr and Sauer [66] model neglects the thermodynamic and mass transfer effects on the dynamic of the bubble. It also assumes that the acceleration is negligible for all regimes of cavitating flow.

Charrière et al. [13] assumed that the mass transfer between phases occurs via void ratio transport. Their assumption neglects the vapor phase density variation as a function of the pressure field.

4.2 Energy Balance of TKE

The Reynolds decomposition represents the instantaneous variable as a summation of the fluctuating component and long time-averaged:

$$\phi^i(x_j, t) = \Phi^i(x_j) + \phi'^i(x_j, t) \tag{4.33}$$

The non-stationarity requires:

$$\overline{\phi^i(x_j, t)} = \Phi^i(x_j) = \lim_{T\to\infty} \int_t^{t+T} \phi^i(x_j, t)dt \tag{4.34}$$

Eq. (4.33) is the generalized form of decomposition of the instantaneous variable. The fluctuating component shown in Eq. (4.33) can be further decomposed into the fluctuations introduced by the slow varying drift flow $\phi^i_{drift}(x_j, t)$, fluctuations introduced by the shear instabilities $\phi^i_{KH}(x_j, t)$, reduced-order large-scale coherent structures $\phi^i_c(x_j, t)$, and

high-dimensional small-scale turbulent fluctuations. Therefore, in a cavitating flow the fluctuating component may be decomposed into quadruple terms:

$$\phi'^{i}(x_j,t) = \phi^{i}_{drift}(x_j,t) + \phi^{i}_{KH}(x_j,t) + \phi^{i}_{c}(x_j,t) + \phi^{i}_{ic}(x_j,t) \tag{4.35}$$

Here, $\phi^{i}_{drift}(x_j,t)$ represents the low-frequency drifts that distribute and transfer the energy of the mean flow between high-frequency fluctuations arises as a result of the Kelvin-Helmholtz instability, formation of the coherent structures, and generation of the incoherent turbulent fluctuations.

To extract the low-frequency modes corresponding to drift in the flow field, a low-pass filter with a Gaussian distribution is convoluted with the fluctuating component of the velocity:

$$h(t) = \frac{1}{\sqrt{2\pi}\sigma_G} e^{\frac{-t^2}{2\sigma_G^2}} \tag{4.36}$$

$$\phi^{i}_{drift} = \sum_{\tau=-T_{wz}/2}^{T_{wz}/2} \phi'^{i}(x_j,t)h(t) \tag{4.37}$$

Where T_{wz} is the filter bandwidth. The cutoff frequency may be defined as follows:

$$f_c = \frac{F_s}{2\pi\sigma_G} \tag{4.38}$$

The choice of the filter cutoff frequency for the extraction of the drifting flow depends on the largest unstable structures, KH instabilites.

4.2.1 Standard dynamic mode decomposition algorithm

Hussain & Reynolds decomposition for non-stationary turbulence variable:

$$\phi^i(x_j, t) = \langle \Phi^i(x_j, t) \rangle + \hat{\phi}^i(x_j, t) \tag{4.39}$$

where $\phi^i(x_j, t)$, $\langle \Phi^i(x_j, t) \rangle$ and $\hat{\phi}^i(x_j, t)$ are the instantaneous, non-stationary and fluctuating components, respectively.

The non-stationary part of the variable is decomposed as follows:

$$\langle \Phi^i(x_j, t) \rangle = \tilde{\Phi}^i(x_j, t) + \Phi^i(x_j) \tag{4.40}$$

Where $\tilde{\Phi}^i(x_j, t)$ is the quasi-periodic component of the variable and $\Phi^i(x_j)$ is the long time average component. Here we assume that the continuous turbulence variable can be temporally discretized into a finite number of snapshots. Let $\hat{\phi}^i(x_j, t)$ be a matrix consisting of a set of columns snapshots of the resolved turbulence variable. Here the sampling process is uniform, so the total time is discretized equally between k samples.

A dynamical system can be generally expressed as follows:

$$\frac{\partial}{\partial t}\{\phi^i(x_j, t) - \Phi^i(x_j)\} = \frac{\partial \hat{\phi}^i}{\partial t} = f\{\hat{\phi}^i, t; \mu(t)\} \tag{4.41}$$

Where vector $\hat{\phi}^i(t) \in \mathbb{R}^n$ represents the state of the system and can be obtained by reshaping all variables defining the state of the system into a single column vector; $\mu \in \mathbb{R}^{\hat{n}}$ is a set of non-dimensional system parameters and operator f represents all linear and nonlinear partial

derivatives of vector $\hat{\phi}^i$. Generally, Eq. (4.41) can be a set of coupled Partial Differential Equations (PDEs) governing the flow field in a typical cavitating flow.

In the time-resolved PIV, the system's state is extracted by resolving the velocity vector field in a finite number of cells in the space in each time step. Finally, with a consecutive sampling in time with constant time steps of Δt, the evolution of the dynamical system's state is obtained. DMD assumes that a best fit linear matrix $A \in \mathbb{R}^{n \times m}$ exists that maps the state of the dynamical system from time step $k+1$ to k.

$$\hat{\phi}^i_{k+1} \approx A\hat{\phi}^i_k \tag{4.42}$$

Where n is the rank of the state vector, and m is the number of snapshots. The snapshots obtained from PIV measurements can be rearranged as follows:

$$X = [\hat{\phi}^i_1, ..., \hat{\phi}^i_{m-1}], \quad Y = [\hat{\phi}^i_2, ..., \hat{\phi}^i_m] \tag{4.43}$$

Where the subscripts represent the snapshots time step. Eq. (4.43) implies that each columns of matrix X needs to be mapped to the identical columns of matrix Y through a linear multiplication. Clearly, matrix A is non-unique and for different values of k, different values for A are obtained. Since the state vector accommodates a set of finite descritized vertex in the space and time, the state vector and consequently matrix A is quite large. Instead of defining a full-rank matrix A, DMD introduces an algorithm providing a low-rank eigenvalues and eigenvectors of A matrix that is computationally affordable. Matrix X rank is $n \times m$, where n>m. X can be written using a Singular Value Decomposition (SVD):

$$X \approx U\Sigma V^* \tag{4.44}$$

where $U \in \mathbb{C}^{n\times r}$, $\Sigma \in \mathbb{C}^{r\times r}$ $V \in \mathbb{C}^{m\times r}$. Where U columns are POD mode shapes.

The matrix A may be obtained through the pseudoinverse of X as follows:

$$A = X'V\Sigma^{-1}U^* \tag{4.45}$$

By the projections of A onto the POD mode shapes:

$$\hat{A} = U^*AU = U^*X'V\Sigma^{-1} \tag{4.46}$$

Where $\hat{A} \in \mathbb{R}^{r\times r}$. Matrix $\hat{A}$ eigenvalues define a high-fidelity time evolution of the dynamical system, provided that a sufficient number of POD mode shapes are considered:

$$\hat{A}\Omega = \Omega\lambda \tag{4.47}$$

The eigenvectors, mode shapes, of matrix A are the columns of Φ:

$$\Phi = YV\Sigma^{-1}\Omega$$

The mode amplitude time evolution may be obtained as follows:

$$\Theta = \beta exp^{\tau} \tag{4.48}$$

Where $\Theta \in \mathbb{R}^{r \times \hat{m}}$ is the matrix of DMD modes time evolution and $\beta \in \mathbb{R}^{r}$ is the vector of the initial conditions of mode amplitude.

$$\beta = \beta_o \Phi^{+} \tag{4.49}$$

Where Φ^{+} is Moore–Penrose inverse of Φ, and β_o is the vector of the initial status or the initial snapshot, first snapshot, of the dynamical system.

The decay rate of the modes can be obtained as follows:

$$\lambda_{DMD} = \frac{log_e|\lambda|}{\Delta t}; \tag{4.50}$$

The frequency of mode shapes can be obtained as follows:

$$\tilde{\omega} = f_N \frac{\tan^{-1}(\lambda)}{\pi}; \tag{4.51}$$

Where $\tilde{\omega}$ is the vector of mode shape frequencies, λ is the vector of eigenvalues, and f_N is the Nyquist frequency.

The description of the coherent structures in the cavitating flow that improve our understanding of the underlying physics can be implemented using the DMD. This data-driven technique can extract the dominant physics governing the transport processes and the instabilities mechanism in the flow field. For this purpose, the data captured from the TR-PIV

is used. DMD mode shapes and the corresponding eigenvalues describe the stability of the distinct large-scale energy-carrying physical mechanism. Besides, DMD illustrates the regions of the flow field that the occurrence of each instability is expected: DMD decomposes complex flow fields caused by the cavitation into subdomains where local instabilities occur. Finally, the temporal evolution of the coherent structures, the corresponding oscillation frequency of amplitudes, and the monotonic decay rate of each mode can be extracted from this analysis.

4.3 The Nonlinear Dynamic States

The signal of the POD time coefficient has been acquired by a uniform sampling of the time-resolved PIV data; therefore, it can be exhibited as a data vector of the form:

$$\nu = \{v_1, v_2, ..., v_m\} \tag{4.52}$$

The reconstructed time series is defined as follows:

$$\hat{\nu}_k = \{v_k, v_{k+t'}, v_{k+2t'}, ..., v_{k+(d-1)t'}\} \tag{4.53}$$

where k goes from 1 to $q = m - (d-1)t'$

The delayed reconstructed geometry of the phase-space can be expressed using matrix Π:

$$\Pi = [\nu_k, \nu_{k+t'}, \nu_{k+2t'}, ..., \nu_{k+(d-1)t'}], k = 1, 2, ..., q = m(d-1)t' \tag{4.54}$$

q is the total number of reconstructed points in the state-space:

$$q = m - (d-1)t' \tag{4.55}$$

Where m is the number of samples, and d is the minimum embedding dimensions. The time series contains meaningful information on the instability of the dynamical system. The geometry of the attractors of the dynamical system corresponding to a one-dimensional time signal, for example, time coefficient of POD, can be further investigated using the concept of reconstruction to a finite-dimensional state-space [1]. The reconstruction process can be implemented using a time delay lag shifted coordinate [52].

Each column of the Π matrix determines the state of the dynamical system. Likewise, each column of matrix Π is a point in the state-space of the reconstructed geometry. Using the delay lag and embedding dimensions of attractors, one obtains a series of vectors of time coefficients of POD leading to the finite-dimensional state-space reconstruction. The time delay lags τ for state-space reconstruction can be estimated using Average Mutual Information (AMI) [5, 9]. AMI is obtained from marginal entropies of the original signal and the delayed lag signal. The vector data ν_k and $\nu_{k+t'}$ components are used to find the AMI as follows:

$$AMI(t') = \sum_{k=1}^{m} p(\nu_k, \nu_{k+t'}) \log_2 \left[\frac{p(\nu_k, \nu_{k+t'})}{p(\nu_k)p(\nu_{k+t'})} \right] \tag{4.56}$$

Where $p(\nu_k)$ determines the probability of occurrence of each component of ν_k, and $p(\nu_k, \nu_{k+t'})$ is the probability of co-occurrence of components of ν_k and $\nu_{k+t'}$ in each of the vector sets. AMI can be obtained using different values for t'. Here it is assumed that the location of

the first minimum of AMI is the best estimate of t'. The minimum embedding dimensions of the attractors' reconstruction is evaluated through False Nearest Neighbor (FNN) algorithm [61]. After generation of the delayed reconstruction matrix Π, the Euclidean distance of a point let say k^{th} reconstructed vector, given a dimension d, and its nearest neighbor point is computed as follows:

$$s_k = \min_{\Pi_{\hat{k}}} \|\Pi_k - \Pi_{\hat{k}}\|_2 \tag{4.57}$$

Where s_k is the initial Euclidean distance from the kth point to its nearest neighbor concerning the reference point k. Next, the following expression is assessed:

$$\sqrt{\frac{s(d+1) - s(d)}{s(d)}} > r_{tres.} \tag{4.58}$$

The threshold $r_{tres.}$ is set to be 20. If Eq. (4.58) is false, neighbors are false neighbors [47]. For some values d, the number of the false nearest neighbors to the size of the signal becomes minimum. FNN method implies that the trajectories of the attractors cross, thereby violating the uniqueness of the solution. When dimensions of the reconstructed state-space increase, the number of trajectories crossing each other drops asymptotically. Here The minimum embedding dimension is defined as the dimension d that yields the lowest number of false nearest neighbors. Once the delayed reconstruction of the phase-space is generated Eq. (4.54), the nearest neighbor distance is determined by searching for the point that minimizes the Euclidean distance to the selected reference point. An additional constraint is also imposed to the nearest neighbors that limit the temporal separation to the values greater than the mean period:

$$|k - \hat{k}| > t_{mean} \tag{4.59}$$

The mean period has been acquired using the spectral response of the POD time coefficients. After finding the nearest neighbor point $\hat{i}$ with respect to the i reference frame, the FTLE for an arbitrary interval $L = (l_n - l_o + 1)$ can be defined as follows:

$$\lambda_{FTLE} = \frac{1}{L} \sum_{l=l_o}^{l_n} \frac{1}{l\Delta t} ln \frac{\left\| \Pi_{k+l} - \Pi_{\hat{k}+l} \right\|_2}{\left\| \Pi_k - \Pi_{\hat{k}} \right\|_2} \tag{4.60}$$

Where $\lambda_{FTLE} \in \mathbb{R}^k$, Δt is the sampling time. Then the Lyapunov exponent is obtained using a linear regression model of Eq. (4.60). Given the entire time series of the POD coefficients, Eq. (4.60) can also be used to find the LLE associated with each of the coefficients.

The study of the LLEs is intuitive, where POD coherent structures and their corresponding time dynamics reveal some non-linear states and chaotic behavior. The results of the LLEs are imperative in the stability analysis of the POD energetic modes. LLEs close to zero implies that the corresponding time dynamics are quasi-periodic; positive values of LLEs show the chaos in the time dynamics and negative values represent a periodic behavior of the time dynamics. The LLE obtained from a prolonged period represents the asymptotical behavior of the time dynamics. Using the LLE obtained from an extended period, one can determine the long-term stability of the POD energetic modes. Accordingly, after an extended period, zero LLEs imply that the system asymptotical becomes quasi-periodic. A negative value for LLEs after a long period suggests that the system asymptotically becomes periodic. On the other hand, if the long period of time the LLEs is positive, the system's behavior becomes chaotic.

4.4 CROM Algorithm

For the analysis of the time-resolved velocity vector field of the liquid phase in the Venturi profile, the CROM strategy is employed. The CROM strategy splits the state-space geometry into a finite number of clusters representing the dynamics; each cluster represents a group of points or states in the phase-portrait. Next, a transition model is employed to describe the transition between the states [20]. Here the reduced-order behavior of the instantaneous velocity, $W \in \mathbb{R}^{n \times m}$ is studied where index n represents the rank of the state vector, and m represents the number of snapshots. The input for CROM is the time-resolved snapshots obtained from PIV measurements of the liquid phase.

The components of the distance matrix $Z = [z_{l\hat{l}}] \in \mathbb{R}^{m \times m}$ is defined as follows:

$$z_{l\hat{l}} = \|\omega_l - \omega_{\hat{l}}\|_2 \, , l, \hat{l} = 1, 2, ..m \tag{4.61}$$

Where $z_{l\hat{l}}$ is the Euclidean distance between two snapshots or two columns of W matrix, and ω_l is the state of the system at time step l. Among the clustering algorithms, $k - means++$ has received a lot of attention due to its advantages, such as insensitivity to the initial condition and rapid clustering. The geometry of the phase-portrait obtained from the snapshots is grouped into a finite number clusters $\kappa = \{c_1, c_2, ...c_{k_{tot}}\}$ such that the distance between the points inside of a cluster is minimized, while the distance between the points associated with one cluster to points outside of that cluster is maximized. Therefore, a set of optimal cluster centroid may be obtained as follows:

$$\kappa_{opt} = \min_{\kappa} \tilde{v}\left(\kappa\right) \tag{4.62}$$

Where $\kappa_{opt} \in \mathbb{R}^j$ is the vector of cluster centroid with component $\{c_1, c_2, ...c_{20}\}$, and $\tilde{v}$ is the cluster variance defined as follows:

$$\tilde{v}\left(\kappa\right) = \sum_{k'=1}^{k_{tot}} \sum_{\omega_l \in c_{k'}} \|\omega_l - c_{k'}\|_2 \tag{4.63}$$

The cluster centroid representing the mean mode shape of the points lying in the cluster may be obtained as follows:

$$C = \frac{1}{n_{k'}} \sum_{\omega_l \in c_{k'}} \omega_l = [\xi'_k], k' = 1, ...k_{tot} \tag{4.64}$$

Where $C \in \mathbb{R}^{k' \times n}$ is the matrix of the mode shapes of the cluster centroids and $\xi \in \mathbb{R}^n$ is the vector of the mode shape of each centroid. $n_{k'}$ is the number of points in cluster k'. One may summarize the $k - means + +$ algorithm as follows:

1. Select a sub-sample at random from W. The chosen sub-sample is the first centroid c_1.

2. Computing the Euclidean distance between sample points and the selected centroid at the previous step, $D_{new}(\hat{\phi}^i_j)$.

3. Finding the shortest distance from a data point $\hat{\phi}^i_j$ to the closest center, and repeat this for all data points.

4. Replacing the shortest distances into $D_{old}(\hat{\phi}^i_j)$

5. Normalize $D(\hat{\phi}_j^i)$ with the mean value of 0 and standard deviation 1.

6. Select the next centroid; pick up randomly one point from the normalized distribution

7. Repeat steps 2-6 until we have chosen a total of k centers.

8. Compute point-to-cluster-centroid distances of all data points to each centroid.

9. Assign each data sample to the cluster with the lowest distance from a centroid.

10. Compute the average of the samples in each cluster to obtain k' new centroid locations using Eq. (4.64).

11. Repeat steps 8 through 10 until centroids locations do not change.

$$\Delta = \begin{cases} 1 & \text{if } \omega_l \in c_{k'} \\ 0 & \text{otherwise} \end{cases} \tag{4.65}$$

Where $\Delta \in \mathbb{R}^{k \times m}$

$$n_{k'} = \sum_{l=1}^{m} \tilde{d}_{lk'} \tag{4.66}$$

$$q_{k'} = \frac{n_{k'}}{m} \tag{4.67}$$

$$n_{\tilde{j}k'} = \sum_{l=1}^{m-1} \tilde{d}_{lk'} \tilde{d}_{l+1\tilde{j}} \tag{4.68}$$

The elements of the probability matrix are obtained as follows:

$$p_{\tilde{j}k'} = \frac{n_{\tilde{j}k'}}{n_{k'}} \tag{4.69}$$

, where the rank of the probability matrix is $P \in \mathbb{R}^{k_{tot} \times k_{tot}}$. The probability vector can be defined as follows:

$$\rho_l = \{p_{1,l}, p_{2,l}, ..., p_{k_{tot},l}\} \tag{4.70}$$

$$p_{l+1} = Pp_l \tag{4.71}$$

The long term behavior can be studied as follows:

$$\rho_\infty = \lim_{l \to +\infty} P_l \rho_0 \tag{4.72}$$

$$P_\infty = \lim_{l \to +\infty} P_l \tag{4.73}$$

$$\hat{d}_{\tilde{j}k'} = \left\| c_{\tilde{j}} - c_{k'} \right\|_2, \tilde{j}k' = 1, ...k_{tot} \tag{4.74}$$

where $D = [\hat{d}_{\tilde{j}k'}] \in \mathbb{R}^{k_{tot} \times k_{tot}}$

CROM technique prescribes the path and probability of intermittent transition between dif-

ferent flow regimes and shedding patterns. Fundamentally, the CROM technique is used for modal decomposition of the unsteady flow fields such as cavitating flow. Using the Phase-averaging technique, CROM extracts the dominant flow patterns representing a big population of the flow field status. Statistical analysis of cluster probability distributions reveal the time duration that the flow remains in any of the dominant flow patterns. Besides, this technique detects the clusters resulting in bifurcation occurrence where the cloud shedding pattern fundamentally changes.

4.5 POD Time Dynamics Mathematical Model

POD technique decorrelates the length scales and yields time coefficients determining the fluctuations of the energy of each mode. Velocity field reconstruction from the spatial structures and the time coefficients is expressed as follows:

$$u_i = \sum_{n=1}^{N_{POD}} \upsilon_{i,n}(x_1, x_2)\sigma_n \nu_n(t) \tag{4.75}$$

The time fluctuations may be used to build a system of ODEs that determines the dynamics of the coherent structures. The dynamical system mathematically can be expressed through Eq. (4.41). The governing equations of the dynamical system, right-hand side of Eq. (4.41), may be extracted through a robust data-driven technique. The generic form of the system of governing equations considering polynomials up to the fifth-order is as follows:

$$\frac{d\nu_i}{dt} = 1 + P_5(\nu_j), \{i, j\} = 1, 2, ..., 4 \tag{4.76}$$

Once the generic governing equations are considered, one needs to find the coefficient via regressions methods. The right-hand side of the dynamical system, defining the multi-variable fifth-order polynomial, consists of $r_p = 126$ terms. Since the time fluctuations of POD are obtained from the PIV measurements, the time derivative of the data may be obtained through high-resolution finite-difference differentiation such as:

$$\frac{d\nu_i}{dt} = \frac{1}{12\Delta t}(\nu_i(t_o - 2\Delta t) - 8\nu_i(t_o - \Delta t) + 8\nu_i(t_o + \Delta t) - \nu_i(t_o + 2\Delta t)) + O(\Delta t^4) \quad (4.77)$$

Then, matrix $\Psi \in \mathbb{R}^{N_{test} \times r}$ is built from the vectors of the time derivative of POD coefficients, $\frac{d\nu_i}{dt}$. The Koopman observables, polynomials reconstruction of the measured data, are stacked into a matrix $\tilde{X} \in \mathbb{R}^{N_{test} \times r_p}$. Following system of linear differential equations may be solved to obtain the vectors of coefficients of the polynomial, $\tilde{Z} = [\zeta_1, \zeta_2, \zeta_3, \zeta_4] \in \mathbb{R}^{r_p \times r}$.

$$\Psi = \tilde{X}\zeta_i \quad (4.78)$$

Eq. (4.78) is an over-determined system of equations. The coefficients of the polynomial are obtained by the minimization of the smallest l_2 norm. Minimization of smallest l_2 norm yields an overfitted model with high complexity. Besides, such a model lacks interpretablity and physical meaning because it randomly selects a tuning parameter that maps the input to output with high accuracy. Regularization can be employed that avoids overfitting the governing equations of the dynamical system. The least absolute shrinkage and selection operator (LASSO) [73] minimizes the smallest l_2 norm subjected to a l_1 regularization:

$$\underset{\zeta_i}{arg\,min}\left(\frac{1}{2N_{test}}\sum_{k=1}^{N_{test}}(\psi_i^k-\chi^k\zeta_i)^2+\lambda_{reg.}\sum_{k_{r_p}=1}^{r_p}|\zeta_i|\right) \tag{4.79}$$

The data of POD time coefficients are partitioned randomly into 10-fold of roughly equal, disjoint subsets. One fold, the test set, is reserved for evaluating the model, and the rest of the folds are used to train the polynomial coefficients. Next, $\lambda_{reg.}$ is varied through a range of values, and all realizable models with the corresponding closure coefficients are validated against the test set. Since the evaluation of the derivative through the finite-difference scheme introduces some level of noise to the data, a sparse polynomial is not feasible. However, the l_1 norm regularization parameter can be adjusted to cancel out some of the high order non-linear terms contributing to the over-fitting to the test set data. Besides, one may use the physical insight obtained from the governing equations to estimate the level of non-linearity of the dynamical system. In this regard, to build a reasonably sparse model representing the dynamics of the POD mode coefficients, the cross-validation MSE is utilized. Based on the value of the MSE, the final complexity of the model can be selected, and the physical interpretability of the model can be further assessed for distinct models. Substitution of Eq. (4.75) into the conservation of momentum equation yields a POD reduced-order model [44]. The reduced-ordered form of the momentum equation governing the dynamics of the fluctuating component of velocity, u', can be expressed as follows:

$$\frac{d\nu}{dt}=\mathcal{L}(\nu)+\mathcal{N}(\nu) \tag{4.80}$$

Where $\mathcal{L}$ represents the linear operators including pressure gradients and diffusive terms, and $\mathcal{N}$ represents the nonlinear convective terms due to inertial forces. The nonlinear inertial forces redistribute the energy between different large length scales, producing no kinetic

energy in an incompressible flow. The quadratic non-linearity preserve turbulence kinetic energy, thus:

$$\nu\mathcal{N}(\nu) = 0 \tag{4.81}$$

Eq. (4.81) yields a set of constraints to Eq. (4.10) enforcing the conservation of energy to the system of linear equations. Next, to address the compressibility of the flow, the regularization parameter may be relaxed to decrease the uncertainty of the model.

$$\begin{bmatrix} \nu_1 \\ \nu_2 \\ \nu_3 \\ \nu_4 \end{bmatrix}^T \begin{bmatrix} z_{1,6}\nu_1 & z_{1,7}\nu_1 + z_{1,10}\nu_2 + z_{1,11}\frac{\nu_3}{2} + z_{1,12}\frac{\nu_4}{2} & z_{1,8}\nu_1 + z_{1,11}\frac{a_2}{2} + z_{1,13}\nu_3 + z_{1,14}\frac{\nu_4}{2} & z_{1,9}\nu_1 + z_{1,12}\frac{\nu_2}{2} + z_{1,14}\frac{\nu_3}{2} + z_{1,15}\nu_4 \\ z_{2,6}\nu_1 + z_{2,7}\nu_2 + z_{2,8}\frac{\nu_3}{2} + z_{2,9}\frac{\nu_4}{2} & z_{2,10}\nu_2 & z_{2,8}\frac{\nu_1}{2} + z_{2,11}\nu 2 + z_{2,13}\nu_3 + z_{2,14}\frac{\nu_4}{2} & z_{2,9}\frac{\nu_1}{2} + z_{2,12}\nu_2 + z_{2,14}\frac{\nu_3}{2} + z_{2,15}\nu_4 \\ z_{3,6}\nu_1 + z_{3,7}\frac{\nu_3}{2} + z_{3,8}\nu_3 + z_{3,9}\frac{\nu_4}{2} & z_{3,7}\frac{\nu_1}{2} + z_{3,10}\nu_2 + z_{3,11}\nu_3 + z_{3,12}\frac{\nu_4}{2} & z_{3,13}\nu_3 & z_{3,9}\frac{\nu_1}{2} + \zeta_{3,12}\frac{\nu_2}{2} + z_{3,14}\nu_3 + z_{3,15}\nu_4 \\ z_{4,6}\nu_1 + z_{4,7}\frac{\nu_3}{2} + z_{4,8}\frac{\nu_2}{2} + z_{4,9}\nu_4 & z_{4,7}\frac{\nu_1}{2} + z_{4,10}\nu_2 + z_{4,11}\frac{\nu_3}{2} + z_{4,12}\nu_4 & z_{4,8}\frac{\nu_1}{2} + z_{4,11}\frac{\nu_2}{2} + z_{4,13}\nu_3 + z_{4,14}\nu_4 & z_{4,15}\nu_4 \end{bmatrix} \begin{bmatrix} \nu_1 \\ \nu_2 \\ \nu_3 \\ \nu_4 \end{bmatrix} = 0 \tag{4.82}$$

$$z_{1,6} = z_{2,10} = z_{3,13} = z_{4,15} = 0 \tag{4.83a}$$

$$z_{1,7} = -z_{2,6} \tag{4.83b}$$

$$z_{1,8} = -z_{3,6} \tag{4.83c}$$

$$z_{1,9} = -z_{4,6} \tag{4.83d}$$

$$z_{2,7} = -z_{1,10} \tag{4.83e}$$

$$z_{3,8} = -z_{3,13} \tag{4.83f}$$

$$z_{4,9} = -z_{1,15} \tag{4.83g}$$

$$z_{2,11} = -z_{3,10} \tag{4.83h}$$

$$z_{2,13} = -z_{3,11} \tag{4.83i}$$

$$z_{2,12} = -z_{4,10} \tag{4.83j}$$

$$z_{2,15} = -z_{4,12} \tag{4.83k}$$

$$z_{3,14} = -z_{4,13} \tag{4.83l}$$

$$z_{3,15} = -z_{4,14} \tag{4.83m}$$

$$z_{2,8} + z_{3,7} + z_{1,11} = 0 \tag{4.83n}$$

$$z_{2,9} + z_{4,7} + z_{1,12} = 0 \tag{4.83o}$$

$$z_{3,9} + z_{4,8} + z_{1,14} = 0 \tag{4.83p}$$

$$z_{2,14} + z_{3,12} + z_{4,11} = 0 \tag{4.83q}$$

4.6 Pressure Reconstruction Method

Since pressure drop in the Venturi section occurs abruptly, the dynamical system goes through an isothermal phase change during the accumulation of the gas phase. Besides, the force due to the surface tension is negligible compared to the inertial forces. Based on the assumptions mentioned above, the 2D conservation of mass and momentum incompressible form for a mixture of gas and liquid read:

$$\frac{\partial \rho_m}{\partial t} + \frac{\partial(\rho_m u)}{\partial x} + \frac{\partial(\rho_m v)}{\partial y} = 0 \tag{4.84a}$$

$$\frac{\partial(\rho_m u)}{\partial t} + \frac{\partial(\rho_m uu + p)}{\partial x} + \frac{\partial(\rho_m uv)}{\partial y} = \frac{\partial \tau_{xx}}{\partial x} + \frac{\partial \tau_{xy}}{\partial y} \tag{4.84b}$$

$$\frac{\partial(\rho_m v)}{\partial t} + \frac{\partial(\rho_m vu)}{\partial x} + \frac{\partial(\rho_m vv + p)}{\partial y} = \frac{\partial \tau_{xy}}{\partial x} + \frac{\partial \tau_{yy}}{\partial y} \tag{4.84c}$$

Assuming that the mixture density, ρ_m, is linearly depending on the density of each phase, one can express the density relation as follows[11]:

$$\rho_m = (1 - \alpha)\rho_l + \alpha\rho_g \tag{4.85}$$

α is the gas volume fraction, ρ_l is the liquid-phase density, and ρ_g is the density of the gas phase.

The stress components τ_{ij} can be written as:

$$\tau_{xx} = \frac{2}{3}\mu_m\left(2\frac{\partial u}{\partial x} - \frac{\partial v}{\partial y}\right) \tag{4.86a}$$

$$\tau_{yy} = \frac{2}{3}\mu_m\left(2\frac{\partial v}{\partial y} - \frac{\partial u}{\partial x}\right) \tag{4.86b}$$

$$\tau_{xy} = \mu_m\left(\frac{\partial u}{\partial y} + \frac{\partial v}{\partial x}\right) \tag{4.86c}$$

The mixture viscosity may be expressed as follow [19]:

$$\mu_m = (1-\alpha)(1+2.5\alpha)\mu_l + \alpha\mu_g \tag{4.87}$$

In cavitating flows, local pressure drop under the vapor pressure yields the phase transition of the fluid. Given the velocity and density snapshots of the dynamical system, the instantaneous pressure field can be obtained explicitly by solving the compressible momentum equation, i.e., Eq. (4.84) pressure. Estimating the instantaneous pressure field, one can explicitly locate the phase-change regions to verify the experimental density evaluations.

For the compressible momentum equation, pressure and velocity are coupled. After taking the divergence of the momentum equations, Eq. (4.84), in x and y directions, a Poisson equation in the following form may be obtained:

$$\frac{\partial^2 p}{\partial x^2} + \frac{\partial^2 p}{\partial y^2} = RHS \tag{4.88}$$

The RHS contains the partial derivatives of the inertial forces and molecular diffusive terms:

$$RHS = -\frac{\partial}{\partial x}\Big[\frac{\partial(\rho_m u)}{\partial t} + \frac{\partial(\rho_m uu)}{\partial x} + \frac{\partial(\rho_m uv)}{\partial y} - \Big(\frac{\partial \tau_{xx}}{\partial x} + \frac{\partial \tau_{xy}}{\partial y}\Big)\Big] \\ - \frac{\partial}{\partial y}\Big[\frac{\partial(\rho_m v)}{\partial t} + \frac{\partial(\rho_m vu)}{\partial x} + \frac{\partial(\rho_m vv)}{\partial y} - \Big(\frac{\partial \tau_{xy}}{\partial x} + \frac{\partial \tau_{yy}}{\partial y}\Big)\Big] \quad (4.89)$$

LHS of Eq. (4.88) is discretized with a diffusive-type central differencing scheme which is solved by applying an iterative technique with a Successive Over Relaxation (SOR) parameter, i.e., $\lambda > 1$. The optimal value to use for the SOR parameter, λ, is predicted for boundary conditions. Given the Dirichlet boundary conditions, the optimal value for the SOR parameter is the smaller root of the following relation [applied numerical analysis seventh edition]:

$$\Big[cos(\frac{\pi}{I}) + cos(\frac{\pi}{J})\Big]^2 \lambda^2 - 16\lambda + 16 = 0 \quad (4.90)$$

where I and J are the number of subdivisions corresponding to the rectangular region.

$$p_{i,j}^{l+1} = \frac{p_{i+1,j}^{l} + p_{i-1,j}^{l} + p_{i,j+1}^{l} + p_{i,j-1}^{l}}{4} + RHS_{i,j}^{l} \quad (4.91)$$

$$p_{i,j}^{l+1} = \lambda p_{i,j}^{l+1} + (1-\lambda) p_{i,j}^{l} \quad (4.92)$$

Neumann boundary condition has been imposed on the Venturi test section walls, and constant pressure, Dirichlet boundary condition, acquired from the pressure gauges is set on the

nodes located adjacent to the inlet and the outlet boundaries:

$$p_{i,j} = p_{inlet} \quad i,j \in inlet \tag{4.93a}$$

$$p_{i,j} = p_{outlet} \quad i,j \in outlet \tag{4.93b}$$

$$\frac{\partial p_{i,j}}{\partial x_i} = 0 \quad i,j \in wall \tag{4.93c}$$

For example, imposing the Neuman boundary condition, one can express the pressure on the wall boundary as follows:

$$p_{wall}^{l+1} = 2p_{i-1,j}^{l} + p_{i,j+1}^{l} + p_{i,j-1}^{l} + RHS_{i,j}^{l} \tag{4.94}$$

The following relation has been checked for all instances that meet the convergence criteria

$$res = \left\| \frac{p_{i,j}^{l+1} - p_{i,j}^{l}}{p_{i,j}^{l+1}} \right\|_2 < 10^{-6} \tag{4.95}$$

4.7 Uncertainty Quantification of Pressure Field

The posterior distribution of the velocity propagates the uncertainty through the source term. The expected value $\mathbb{E}$ and covariance matrix Σ of the source term can be studied to present the uncertainty of the pressure field. Since the inertial terms in the Navier-Stokes equations are non-linear, the Monte Carlo method is used to obtain the pressure uncertainty. Source term contains non-linear terms depending on the velocity and vapor void fraction.

Derivation of the uncertainty propagation to the source term (RHS) is straightforward in the Monte Carlo method. To implement Monte Carlo method for uncertainty propagation, one needs to randomly generate realizations of variables, given the posterior distribution of the corresponding variables, e.g. $\Sigma(\boldsymbol{u}|\boldsymbol{u}_{PIV})$, $\mathbb{E}(\boldsymbol{u}|\boldsymbol{u}_{PIV})$ [34, 53]. Here, the realizations of the variables are generated using the Cholesky decomposition of the covariance matrix. The Cholesky decomposition can be written as follows:

$$\Sigma(\boldsymbol{u}|\boldsymbol{u}_{PIV}) = LL^T \tag{4.96}$$

Then, the lower-triangular matrix L is multiplied by vectors of uncorrelated random realizations extracted from Gaussian distribution with standard deviation and expected value of one and zero, respectively [28]. Next, the source term is computed for each vector realization. Finally, the source term's standard deviation and expected value can be evaluated, given distinct realizations of the source term.

In the present dissertation, the pressure field is constructed using the PIV data. It is assumed that the velocity field is unknown, and there is no prior estimation of the velocity field in the PIV measurements locations. The assumptions mentioned above result in the following equations for the expected value and covariance matrix:

$$\mathbb{E}(\boldsymbol{u}|\boldsymbol{u}_{PIV}) = u_{PIV} \tag{4.97}$$

$$\Sigma(\boldsymbol{u}|\boldsymbol{u}_{PIV}) = R \tag{4.98}$$

In other words, Eqs. (4.97) and (4.98) emphasize the fact that the posterior expected value

and covariance matrix are equal to the velocity field obtained from PIV and its corresponding measurement uncertainty, respectively.

The expected value and covariance for the pressure are derived using the inverse of the Laplace operator, A, and the expected value and covariance of the source term:

$$\mathbb{E}(p) = A^{-1}\mathbb{E}(RHS) \tag{4.99}$$

$$\Sigma(p) = A^{-1}\Sigma(RHS)A^{-T} \tag{4.100}$$

4.8 Favre-averaged Navier-Stokes Equations

In the following two sections, a framework has been developed to identify the dominant mechanism that results in local momentum variation. The data-driven technique begins with the derivation of the general governing equation, which describes the local momentum change resulting from physical processes such as the gradient of pressure, Reynolds stresses, and viscous stresses. Here the terms in the conservation of momentum have been obtained using the data of X-ray imaging, which provides the planar velocity field and local void fraction, accompanied by the numerical simulations of the instantaneous pressure field. Next, Since in many regimes of cavitating flow, some of the terms have pivotal importance in the governing equation balance, it is suggested that the complexity of the model can be reduced in local regions by neglecting some of the physical mechanisms.

Next, it is assumed that each term in the governing equation represents a coordinate system

and the entire terms reconstruct an equation space. Each point in the equation space represents the values of terms in space and time shown, let's say for Favre-averaged momentum equation by a vector with eight entries. The negligible terms will have zero components in some regions. Zero entries make it feasible to dismiss some of the terms in the governing equation. Identifying the regions of the flow field where some of the terms are negligible and have an insignificant contribution to the balance can be implemented using machine learning tools. The following section focuses on the tools used to identify the regions where subsets of the terms describe the behavior of the system.

The dominant balance mechanism of cavitating inception past the throat of the Venturi-type test section has been studied. Terms obtained from Favre-averaged Navier-Stokes equations are represented in the form of equation space. Next, the equation space is clustered, and associated local dominant balance models are presented to conserve the momentum.

The instantaneous velocity may be decomposed into a mass-averaged component and a fluctuating component:

$$u = \tilde{u} + u'' \tag{4.101a}$$

$$v = \tilde{v} + v'' \tag{4.101b}$$

Where mass-averaged for an arbitrary variable ϕ reads:

$$\tilde{\phi} = \frac{\overline{\rho\phi}}{\overline{\rho}} \tag{4.102}$$

Therefore, the Favre-averaging of an arbitrary variable ϕ reads:

$$\tilde{\phi}(x,y,t) = \frac{1}{\overline{\rho}}\frac{1}{T}\int_t^{t+T} \rho(x,y,\tau)\phi(x,y,\tau)d\tau \tag{4.103}$$

The Reynolds-averaging of an arbitrary variable ϕ reads:

$$\overline{\phi}(x,y,t) = \frac{1}{T}\int_t^{t+T} \phi(x,y,\tau)d\tau \tag{4.104}$$

Where T is long relative to the period of the large-scale turbulent fluctuations, here DMD eigenvalues are used to define the time scale of the large-scale turbulent fluctuations.

$$p = P + p' \tag{4.105a}$$

$$\rho = \bar{\rho} + \rho' \tag{4.105b}$$

Favre-averaged momentum equations can be written as follows:

$$\frac{\partial(\overline{\rho}\tilde{u})}{\partial t} + \frac{\partial(\overline{\rho}\tilde{u}\tilde{u})}{\partial x} + \frac{(\overline{\rho}\tilde{u}\tilde{v})}{\partial y} = -\frac{\partial P}{\partial x} + \frac{\partial \tilde{\tau}_{xx}}{\partial x} + \frac{\partial \tilde{\tau}_{xy}}{\partial y} + \frac{\partial \overline{\tau}_{xx}}{\partial x} + \frac{\partial \overline{\tau}_{xy}}{\partial y} \tag{4.106a}$$

$$\frac{\partial(\overline{\rho}\tilde{v})}{\partial t} + \frac{\partial(\overline{\rho}\tilde{v}\tilde{u})}{\partial x} + \frac{(\overline{\rho}\tilde{v}\tilde{v})}{\partial y} = -\frac{\partial P}{\partial y} + \frac{\partial \tilde{\tau}_{xy}}{\partial x} + \frac{\partial \tilde{\tau}_{yy}}{\partial y} + \frac{\partial \overline{\tau}_{xy}}{\partial x} + \frac{\partial \overline{\tau}_{yy}}{\partial y} \tag{4.106b}$$

$$\tag{4.106c}$$

The terms on the left represent the change in mean momentum of a fluid element owing to the unsteadiness in the mean momentum and the convection by the mean momentum, while those on the right-hand side of the equation are the mean pressure gradient, viscosity

stresses, and Reynolds stresses, respectively

$$\tilde{\tau}_{xx} = -\frac{\overline{\rho u'' u''}}{\overline{\rho}} \tag{4.107a}$$

$$\tilde{\tau}_{xy} = -\frac{\overline{\rho u'' v''}}{\overline{\rho}} \tag{4.107b}$$

$$\tilde{\tau}_{yy} = -\frac{\overline{\rho v'' v''}}{\overline{\rho}} \tag{4.107c}$$

Where velocity fluctuating components can be derived as follows:

$$u'' = u - \frac{\overline{\rho u}}{\overline{\rho}} \tag{4.108a}$$

$$v'' = v - \frac{\overline{\rho v}}{\overline{\rho}} \tag{4.108b}$$

$$\overline{\tau}_{xx} = \frac{2}{3}\tilde{\mu}\left(2\frac{\partial \tilde{u}}{\partial x} - \frac{\partial \tilde{v}}{\partial y}\right) \tag{4.109a}$$

$$\overline{\tau}_{yy} = \frac{2}{3}\tilde{\mu}\left(2\frac{\partial \tilde{v}}{\partial y} - \frac{\partial \tilde{u}}{\partial x}\right) \tag{4.109b}$$

$$\overline{\tau}_{xy} = \tilde{\mu}\left(\frac{\partial \tilde{u}}{\partial x} + \frac{\partial \tilde{v}}{\partial y}\right) \tag{4.109c}$$

$$\tag{4.109d}$$

Where $\tilde{\mu}$ is computed as follows:

$$\tilde{\mu} = \frac{\overline{\rho \mu}}{\overline{\rho}} \tag{4.110}$$

4.9 Gaussian Mixture Model

The domain of the Favre-averaged momentum equation is discretized with some interrogation windows representing the space, and time-averaged snapshots, representing the time-averaged steps. Next, the forces due to unsteadiness, advection, pressure gradient, Reynolds stress, and viscous stress terms are evaluated in discretized spacetime points. Each of the terms in the governing equations, e.g., Favre-averaged momentum equations or the Navier-Stokes equations, represents a coordinate in the state-space of the governing equations. The snapshots of the terms in the governing equations can be rearranged into a vector. Finally, the vectors representing each term can be stack in a matrix of forces as follows

$$F_x = [\frac{\partial(\bar{\rho}\tilde{u})}{\partial t}, \frac{\partial(\bar{\rho}\tilde{u}\tilde{u})}{\partial x}, \frac{(\bar{\rho}\tilde{u}\tilde{v})}{\partial y}, \frac{\partial P}{\partial x}, \frac{\partial \tilde{\tau}_{xx}}{\partial x}, \frac{\partial \tilde{\tau}_{xy}}{\partial y}, \frac{\partial \overline{\tau}_{xx}}{\partial x}, \frac{\partial \overline{\tau}_{xy}}{\partial y}] \tag{4.111a}$$

$$F_y = [\frac{\partial(\bar{\rho}\tilde{v})}{\partial t}, \frac{\partial(\bar{\rho}\tilde{v}\tilde{u})}{\partial x}, \frac{(\bar{\rho}\tilde{v}\tilde{v})}{\partial y}, \frac{\partial P}{\partial y}, \frac{\partial \tilde{\tau}_{xy}}{\partial x}, \frac{\partial \tilde{\tau}_{yy}}{\partial y}, \frac{\partial \overline{\tau}_{xy}}{\partial x}, \frac{\partial \overline{\tau}_{yy}}{\partial y}] \tag{4.111b}$$

Where matrix $F_x, F_y \in \mathbb{R}^{n\times k} = [f_{i,j}]$. k is both the number of terms in the governing equations, e.g., $k = 8$ in the Favre-averaged momentum equation or number of clusters. $n = n_w \times n_s$ is the number of spacetime points. where n_s is the number of snapshots, and n_w is the number of interrogation windows. Each row in the matrix F_x and F_y is a point in the state-space whose coordinates are associated with the terms in the governing equations. Where each row, equivalently each data point in the state-space, can be defined by a vector $x_i \in \mathbb{R}^{n_t}$, where n_t is the number of terms in each equation, e.g., $n_t = 8$ in the Favre-averaged momentum equation. Matrix F_x is called some observations of the governing equations. Gaussian Mixture Models (GMMs) assume that these observations can be represented by combining a set of clusters. The GMMs assumes that the Probability

Density Function (PDF) for the observations of data points in matrix F_x is a weighted linear sum of a set of Gaussian distributions:

$$Prob(x_i) = \sum_{p=1}^{k} \alpha_p \mathcal{N}(x_i|\mu_p, \sigma_p) \tag{4.112}$$

The probability that observed point x_i comes from cluster k is defined as follows:

$$\gamma_{i,j} = p(z = j|x = x_i) \tag{4.113}$$

$\gamma_{i,j}$ is defined as the responsibility of the cluster j takes for the data point x_i. Eq. (4.113) is computed for a mixture of Gaussian distribution as follows:

$$\gamma_{i,j} = \frac{\alpha_j \mathcal{N}(x_i|\mu_j, \Sigma_j)}{\sum_{c=1}^{k} \pi_c \mathcal{N}(x_i|\mu_c, \Sigma_c)} \tag{4.114}$$

In this case, the points assigned softly to cluster c can be defined as follows:

$$n_c = \sum_{i=1}^{n} \gamma_{i,c} \tag{4.115}$$

Expectation-Maximization (EM) algorithm [2] has been used to compute the maximum likelihood. The EM algorithm looks for the maximum local likelihood of the parameters of the GMM model. The objective is to determine α_j, μ_j, and Σ_j for each Gaussian probability distribution. An estimate of the Gaussian distribution parameters is using the Expectation-Maximization (EM) algorithm. The algorithm starts by assuming an initial guess of the parameters, α_j, μ_j, and Σ_j, for all clusters. the posterior probability of a data points x_i can

be determined using Eq. (4.114). These step is called "E-step" and it is evaluated for all data points and all clusters, e.g. $i = 1, ..., n$ $j = 1, ..., k$. Next, the weighted-averaged of the mean values and covariance matrices is re-estimated as follows:

$$\mu_c^{new} = \frac{1}{n_c} \sum_{i=1}^{n} \gamma_{i,c} x_i \tag{4.116}$$

$$\Sigma_c^{new} = \frac{1}{n_c} \sum_{i=1}^{n} \gamma_{i,c} (x_i - \mu_i^{new})(x_i - \mu_i^{new})^T \tag{4.117}$$

$$\pi_c^{new} = \frac{n_c}{n} \tag{4.118}$$

This step is called the "M-step." These two steps are repeated iteratively until the log-likelihood converges.

4.10 Phase Transition Modeling

The following Partial Differential Equation (PDE) has been suggested that represents the mass production or destruction term:

$$\dot{m}_v = N(p, p_t, p_x, p_y, u_x, v_y, \alpha_x, \alpha_y, x, t, q) \tag{4.119}$$

N(.) is a nonlinear function of pressure, void fraction, space, time, and system parameters such as density. Given the mass production term, the function N(.) may be prescribed

to model the system's measurements at space and time. It is assumed that some of the parameters are contributing to the physics of the cavitating flow and the rest of the terms are negligible or correlated with noise that promotes the sparsity of such a model. r and ζ_j determine the sparsity of the model, and q is a constant.

$$N = \sum_{j=1}^{r} N_j(p, p_t, p_x, p_y, u_x, v_y, \alpha_x, \alpha_y, x, t, q)\zeta_j$$

The transport equation based on vapor volume fraction reads:

$$\dot{m}_v = \frac{\partial \alpha}{\partial t} + u\frac{\partial \alpha}{\partial x} + v\frac{\partial \alpha}{\partial y} \tag{4.120}$$

Rudy et al. [65] proposed a method capable of discovering the source term in Eq. (4.120), given the spatial and temporal data of the variables. To construct the regression model, firstly, the time and space data of mass transition term, $\dot{m}_v$, are collected into a column vector $U \in \mathbb{R}^{m\times n}$ where m and n represent the time and space points, respectively. Next, a library of linear and nonlinear terms and their partial derivatives, consisting of pressure and void fraction and the derivatives, are collected in $\Theta \in \mathbb{R}^{(m\times n)\times D}$ where D is total number of linear and nonlinear terms. Each column of Θ represents the values of one of the linear or nonlinear terms. The source term field PDE may be expressed as follows:

$$\dot{m}_v = \Theta(U)\zeta \tag{4.121}$$

The linear system of equations mentioned above is solved for coefficients, ζ. U and Θ matrices read:

$$U = \begin{bmatrix} U(\mathbf{x}_1, t_1) \\ U(\mathbf{x}_2, t_2) \\ \vdots \\ U(\mathbf{x}_n, t_m) \end{bmatrix}$$

$$\Theta = \begin{bmatrix} 1 & p(x_1, t_1) & p_t(x_1, t_1) & \dots & p_{xx}(x_1, t_1) \\ 1 & p(x_2, t_1) & p_t(x_2, t_1) & \dots & p_{xx}(x_2, t_1) \\ \vdots & \vdots & \vdots & & \vdots \\ 1 & p(x_n, t_m) & p_t(x_n, t_m) & \dots & p_{xx}(x_n, t_m) \end{bmatrix}$$

The Least Absolute Shrinkage and Selection Operator (LASSO) minimizes the smallest l_2 norm subjected to an l_1 regularization:

$$\underset{\zeta}{arg\,min} \left\| \Theta\zeta - U \right\|_2 + \lambda \left\| \zeta \right\|_1$$

Chapter 5

Verification and Validation of Mathematical Models

This chapter shows the relative error of the simulation implemented using an in-house CFD code; the results of both true pressure field and estimated pressure field are plotted in one graph. In this regard, firstly, compressible form of Navier-Stokes equations are used to compute the pressure field over a transitional boundary layer as it occurs on a flat plate. Direct Numerical Simulation (DNS) of a transitional boundary layer over a flat plate has been implemented, thereby yielding the instantaneous pressure and velocity field, which is assumed to be the true value of variables. The DNS has been developed and implemented at Johns Hopkins University. incompressible Navier-Stokes equations are discretized and solved using a Finite Volume Method (FVM). Given the true velocity vector field obtained from DNS results, the estimated pressure field has been acquired using the in-house CFD code. Accordingly, compressible form of momentum equation is solved for the pressure field. It should be noted that, by definition, a compressible CFD code converges to the incompressible solver, given the fact that the density is a constant.

Additionally, the uncertainty of the pressure computations is presented. The data obtained from the flow field past the throat of the Venturi-type test section is utilized to assess the propagation of the uncertainty from the velocity field and void fraction to the reconstructed pressure. The method was applied to the experimental test case in which the sheet cavity is fully developed; look at the region # 1 depicted in figure 3.4. The covariance matrix of the velocity in the non-cavitating and cavitating regions, accompanied by the covariance matrix of the void fraction extracted from the uncertainty measurements of X-ray imaging, is utilized in the Monte Carlo simulations. The upper bound of the uncertainty assigned to reconstructed pressure has been acquired for non-cavitating and cavitating flow fields.

5.1 Free-stream

The freestream at the leading edge of the plate is assumed to be composed of a uniform velocity, U_∞ and freestream turbulent fluctuations u'_{FST}. Since the turbulent component of the velocity decays as it is transported to the leading edge, the Turbulence intensity adjacent to the leading edge is $Tu = 3\%$.

5.2 Boundary Conditions

A No-slip boundary condition is prescribed at the flat plate wall. A periodic boundary condition is applied at the side endings of the plate to extend the plate to infinity. The continuity boundary condition is applied at the top of the computational domain. Zero pressure gradient is prescribed at the top of the computational domain. An advective boundary condition is considered for the outlet where the plate ends.

5.3 Computational Domain

This section presents the flat plate geometry. DNS of incompressible flow is implemented over a flat plate. The dimensions of the flat-plate is shown in figure 5.1. The half-thickness of the plate is L, and it is used as a reference length scale. Free-stream velocity, U_∞, is used as the reference velocity. As shown in Table 5.1, the length of the plate is $L_x = 1050L$ measured from the leading edge and its width is $L_z = 240L$. Flat plate leading edge has an elliptical shape whose geometry is governed by the following relation:

$$(1 - \frac{1}{AR}\frac{x}{L})^4 + (\frac{y+1}{L})^2 = 1 \tag{5.1}$$

Where AR is the aspect ratio of the elliptical shape, the Reynolds number based on the plate half-thickness, free-stream velocity, and fluid viscosity is $Re_L = 800$.

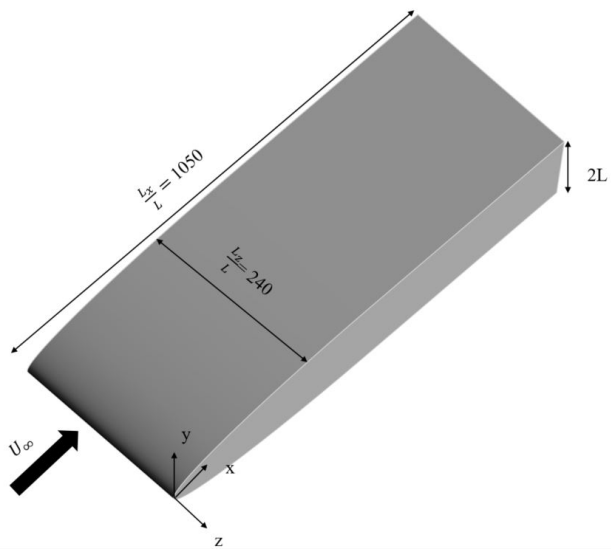

Figure 5.1: The figure represents the flow over a flat plate as a boundary of the computational domain. The solution domain extends $204 \times L$, in the spanwise direction, where L is the half thickness of the plate. The flat plate extends to 1050 half thickness of the plate downstream of the leading edge.

5.4 Computational Mesh

The domain size and grid resolution have been shown in Table 5.1. The number of grid points at the leading edge is 475. Minimum grid spacing, $0.001L$, is applied to the leading edge where the stagnation point is located. The streamwise spacing is $\Delta x^+ = 11.9$. The spacing normal to the wall at the vicinity of the wall is $\Delta y^+_{min} = 0.124$. Within $y^+ < 10$, 29 grid points are accommodated. The spanwise spacing is $0.117L$, and it is uniform in the

spanwise direction. At $x = 1000L$, the spanwise spacing corresponds to $\Delta z^+ = 4.07$. Grid stretching between adjacent cells in both the tangential and normal to the wall is less than 3%.

The simulation time step is $\Delta t = \frac{0.005L}{U_\infty}$. Only the data corresponding to the rectangular domain in the downstream has been utilized for the the validation, and the data in the shallow body-fitted domain adjacent to the leading edge is dismissed. The data used for validation corresponds to $x \in [30.2185, 1000.065]L$, $y \in [0.0036, 26.4880]L$ and $z \in [0, 240]L$.

Table 5.1: computational domain size, number of grid points, and spatial resolution of boundary-layer at $x = 1000 \times L$

$(L_x, L_y, L_z)/L$	(N_x, N_y, N_z)	$\Delta x^+, \Delta y^+_{min}, \Delta z^+$
$(1050, 40, 240)$	$(4097, 257, 2049)$	$(11.9, 0.124, 4.07)$

5.5 Spatial and Temporal Schemes

The First-order Euler scheme is used for both of the simulations. A linear upwind scheme has been employed for the divergence terms to improve the solver instability. For the Laplacian term, a second-order central differencing scheme has been used.

5.6 Results and Analysis

All results in this section are compared against the pressure field obtained from JHTDB [40]. The instantaneous pressure field in the rectangular domain in the downstream obtained from JHTDB and the results of the in-house CFD code have been shown in figure 5.2. It should be

noted that the velocity vector field and pressure field obtained from JHTDB is the true value. Given the true value of the instantaneous velocity vector field, pressure has been estimated using the in-house CFD code. The discrepancy between the black and blue curves in figure 5.2 displays the estimated relative error. A favorable pressure gradient is acquired in both cases in the direction of the flow field. Adjacent to the wall and around $x \approx 0 - 275L$, a laminar inflow region is located, and the instantaneous pressure steadily decreases. Transitional behavior in the pressure fluctuations is observed for $x > 275L$ that corresponds to the viscous sublayer. Strong pressure fluctuations are observed around $x > 370L$ located at the fully developed turbulence downstream. Adjacent to the wall, the pressure obtained from Poisson's equation and DNS agree very well with less than 5% discrepancy in the laminar and transitional regions. The discrepancy grows significantly in the fully developed regions. The significant difference in the fully turbulent region is since DNS uses high-order spatial schemes. According to the theoretical prediction of the boundary layer theory, Along $\frac{y}{L} = 20$ the inertial sublayer occurs at $x > 42L$. The strong pressure fluctuations are observed at $x > 500L$ along $y = 20L$. Since the flow field is located inside the inertial sublayer, pressure fluctuations are not comparably high.

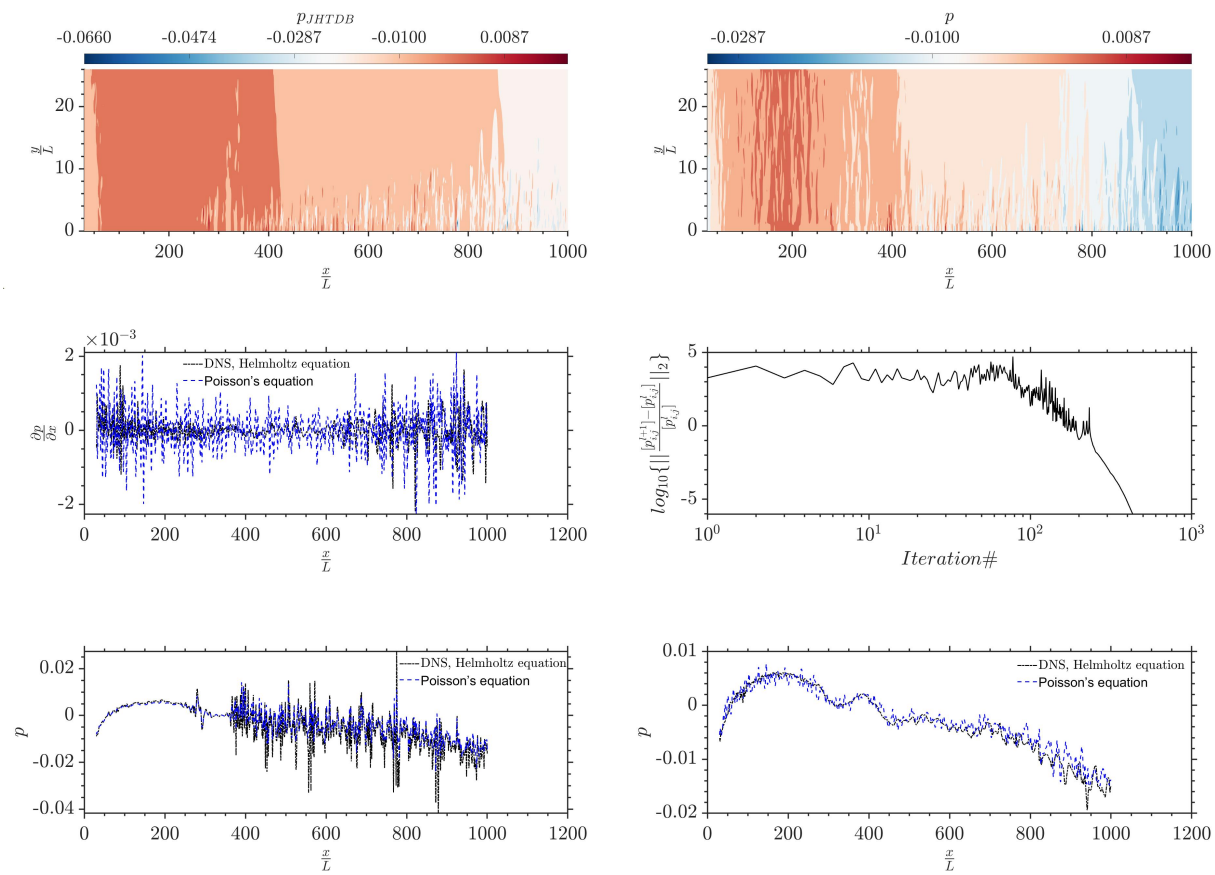

Figure 5.2: Representation of the relative error between the DNS data, which is the true value, and the estimated pressure field obtained from the in-house compressible CFD code (a) Instantaneous pressure distribution of transitional boundary-layer obtained from the Direct Numerical Simulations (DNS) of an incompressible flow over a flat plate [40] at $t = 0.5$ sec. and $Re_L = 800$. (b) Instantaneous pressure distribution obtained from the numerical simulation of compressible form of the pressure Poisson equation, Eq. (4.88). (c) streamwise pressure gradient at $\frac{y}{L} = 20$. (d) Convergence of the pressure field in the L_2 norm. (e) Streamwise pressure distribution on the plate. (f) Streamwise pressure distribution at $\frac{y}{L} = 20$.

In figure 5.3, the solution for the instantaneous pressure gradient vector field at $t \approx 1.5s$ is presented, which illustrates the inception of the vapor sheet past the throat of the Venturi-type test section. The pressure field starts to decrease at the throat of the test section giving rise to the sheet cavity growth depicted through the iso-contours of void fraction. At the interface of the sheet cavity, the magnitude of the pressure gradient vectors acquires the

maximum value, which emphasizes the role of sudden pressure drop before the cavitation inception. The sheet cavity continues to grow along the length of the test section while the magnitude of pressure gradient in the regions with the high void fraction is comparatively lower. In the high void fraction, the wall-bounded sheet cavity, and the interface between liquid and vapor phase, a significant misalignment is observed between the instantaneous gradient of pressure and gradient of density. This misalignment is because the density is a function of both pressure and temperature. This fact emphasizes that the two-phase cavitating flow can not be assumed a barotropic fluid, specifically in the region with a high void fraction, e.g., at the sheet cavity's leading edge. The misalignment between the pressure gradient and the density gradient results in a high vorticity region, i.e., in the vicinity of the liquid-vapor interface and inside the attached sheet cavity. The vorticity generated due to the baroclinity gives rise to a perturbation adjacent to the vapor-liquid interface and the wall. The perturbation on the interface results in velocity discontinuity that gives rise to Kelvin-Helmholtz instabilities at the interface of two phases, and growth of the instabilities eventually creates a coherent attached sheet cavity along the length of the Venturi. Besides, the role of the baroclinic torque is imperative in the production of the eddies and modification of the vapor structures in the sheet cavity. Production of the vorticity in the sheet cavity emphasizes the importance of baroclinic instability. Baroclinic instability provides the required energy for the momentum transport between the liquid and vapor strata. The highly vortical region shows that the presence of the eddies in the sheet cavity results in the mixture of the tracer particles.

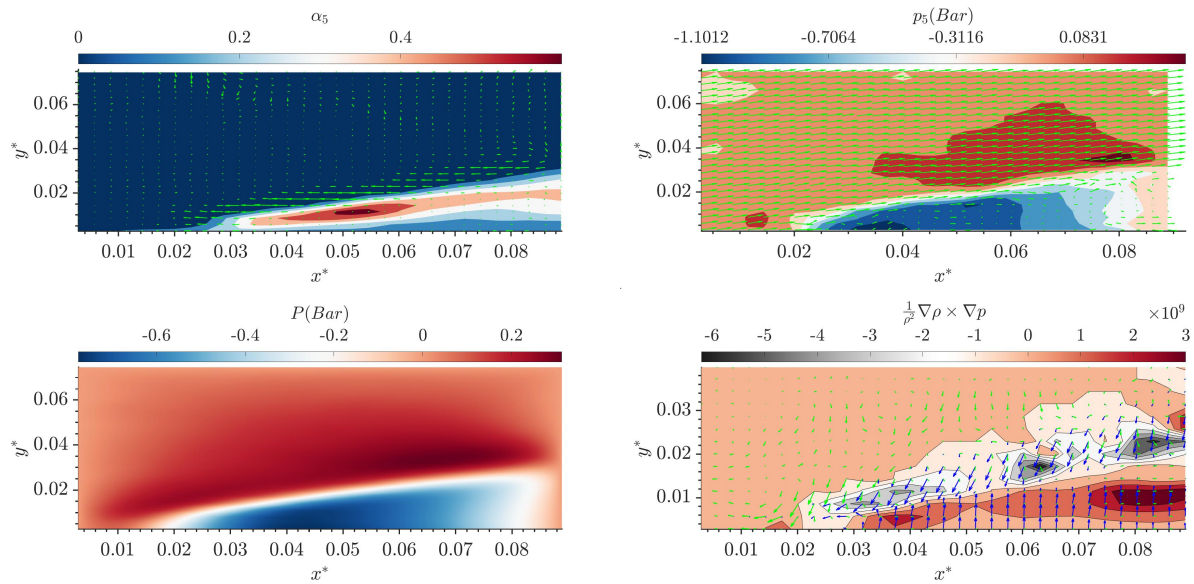

Figure 5.3: Flow characteristics past the throat of the Venturi-type test section at location (1), look at figure 3.4 (a) Sample of the instantaneous pressure gradient vector field overlaid with the contours of the instantaneous gas volume fraction. (b) Sample of the velocity vector overlaid with the contour of the instantaneous pressure field. (c) Time-averaged pressure field at location (1). (d) Sample of instantaneous solenoidal iso-contour depicting baroclinity's high value inside the attached sheet cavity and on the vapor-liquid interface. A high value of baroclinity is the primary mechanism of the attached sheet instability. The misalignment of the pressure gradient vector field (green arrows) and the density gradient vector field (blue arrows) influence the vorticity field. Baroclinic torque is an imperative mechanism of the intermittent vapor jet propagating.

While the previous sections focused on the estimation of the relative error in the numerical scheme as a result of the truncation of the higher-order terms, this section presents the uncertainty that arises in the reconstructed pressure field as a byproduct of the uncertainties in velocity and void fraction experimental measurements. Solution of Eq. (4.91) for the static pressure imposes uncertainties due to the carried uncertainty in the velocity and void fraction fields obtained from the post-processing of the high-speed X-ray imaging. Monte Carlo simulations have been implemented for the cavitating regions and non-cavitating regions to illustrate the propagation of the uncertainty of the measurements in the velocity vector field and void fraction to the pressure field. Figure 5.4 depicts the propagation of the random

velocity and local void fraction uncertainties into the pressure field. The difference between the two figures is corresponding to the measurement uncertainty in the vapor-liquid mixture flow field and the single-phase flow.

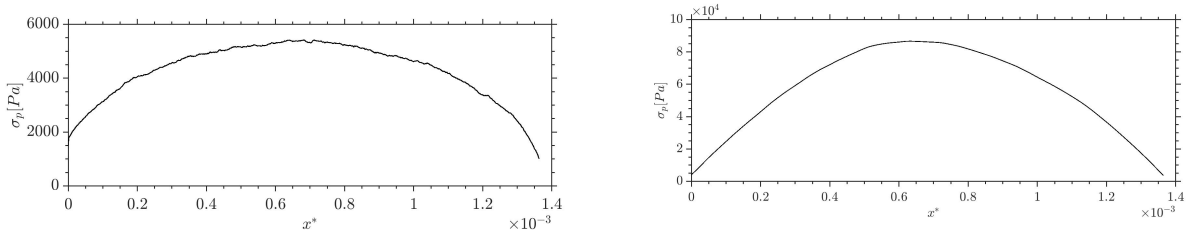

Figure 5.4: Representation of the one-dimensional uncertainty propagation from the velocity vector field and the local void fraction to the pressure field. The measurement uncertainties for the velocity vector field of the liquid-vapor mixture and single-phase flow are $0.46\frac{m}{s}$ and $0.11\frac{m}{s}$, respectively. The uncertainty measurement of the local void fraction is 0.06. Graphs show the standard deviation of the calculated pressure using the Monte Carlo simulations in the (a) single-phase flow and the (b) cavitating flow.

Chapter 6

Data-driven Modal Analysis

6.1 Introduction

In the present chapter, an in-depth analysis of the modes of instabilities in the cavitating flow has been presented by using three distinct data-driven techniques: Dynamic Mode Decomposition (DMD), Proper-Orthogonal Decomposition (POD), and Clustered-based Reduced-Order Modelling (CROM). The multi-modal behavior of the cavitating flow has been studied using DMD. Besides, the initial amplitude, decay rate, and frequency of each instability mode are distilled by analyzing DMD results. The POD time coefficient data is reduced using the Gaussian low pass and bandpass filter. The purpose of reducing the data is two-fold: (1) identifying POD modes associated with distinct instability mechanisms in cavitating flow, (2) showing the energy path and exchange of the TKE between different length scales in the flow field. Besides, the combination of the POD modes of instability can reconstruct the different instantaneous flow regimes, including premature condensation and vapor cloud shedding. In the next step, the non-linear states of the POD time dynamics were studied using FTLE and LLEs to shed light on the stability of the energetic POD modes. FTLE and LLEs reveal the short-term and global stability of the POD time coefficients. The CROM technique takes advantage of the phase-averaging to find the flow patterns, cluster centroid, representing the big population of flow field status. Next, CROM displays the path and the probability of intermittent, spontaneous transition between different regimes (clusters). Ad-

ditionally, CROM Identifies the bifurcation occurrence where the flow regime goes through a drastic change in its pattern. Statistical evaluation of the asymptotic probability distributing shows the time duration spent on each shedding regime.

The velocity vector field of a two-phase cavitating flow in a Venturi-type profile has been acquired through time-resolved Particle Image Velocimetry (PIV). Length scales of the coherent structures are decorrelated using the standard POD algorithm, and most energetic mode shapes are selected. Thanks to the assumption made in the Takens' theorem that time-delayed reconstruction of the state-space conserves the attractors, or the geometrical shape of the original state-space, a time-delayed reconstruction of the original state-space has been obtained. After computation of the delayed reconstruction of the state-space POD time coefficients, the delay for the reconstructed state-space is set to be the local minimum of Average Mutual Information (AMI). Next, the minimum embedding dimensions of the temporal coefficient attractors has been obtained using the False Nearest Neighbor (FNN) algorithm. In the next step, the Rosenstein method has been employed to obtain the Largest Lyapunov Exponent (LLE) and Finite-time Lyapunov Exponent (FTLE) of time coefficients of each of the POD modes. The LLE and FTLE of each POD mode are further analyzed to shed light on the dynamics of the geometry of the attractors in the state-space. Next, the time scales of the coherent structures have been decorrelated using the standard DMD algorithm. Thanks to the time scales decorrelation, the associating frequency and decay rate to each DMD mode shape is presented. The correlation coefficient of the eigenvectors of POD and DMD modes are obtained and further analyzed to complement the identification through POD. Such analysis determines the most probable energy content associated with the frequency content of DMD modes.

Cavitation in a venturi profile has been extensively studied in the past. Thanks to the significant reviews in the literature [54, 62], there is abundant background knowledge on the

cavitation inception, growth, and condensation process past a wedge-shaped profile. The rising interest in the cavitating flow in a venturi profile has been witnessed in the literature; however, understating the complex spatio-temporal structures and the governing dynamics exhibited by this dynamical system has not been studied carefully. Cavitating flow through a venturi shape test section is a proper model for investigating fundamental physics governing the nonlinear state of the two-phase flow fields. It is a complex nonlinear system due to numerous effective system parameters and multiple variables exhibiting some chaotic behavior.

The Reynolds number and free stream cavitation number can significantly influence the system's dynamics, as mentioned above. The cavitation behavior is also governed by some system variables, such as the magnitude of the adverse pressure gradient. Depending on the system parameters and variables impacting the dynamical system, cavitation may occur in some regions of the flow field. Large-scale coherent structures of the cavitating flow, including attached sheet cavitation and cloud cavitation, are incepted for low cavitation numbers and low-pressure areas. Evaporation of the liquid phase occurs due to a strong adverse pressure gradient in the separated shear layer past the venturi throat. Consequently, the accumulation of the vapor phase leads to the formation of the attached sheet cavity. Due to the non-linearity in the system dynamics, such as advective mechanisms, the cavitation regions yield a quasi-periodic behavior resulting in intermittent and stochastic shedding in the form of coherent vapor spatial structures known as the cloud. The attached sheet cavity growth process and growth rate and the onset of the closure of the cavity are profoundly affected by the non-linearity of the dynamical system, thereby making all subsequent events, including (1) the re-entrant liquid phase flow, (2) the shedding of the cloud and (3) condensation of the detached cavities behaving quasi-periodical. The non-linearity of the cavitating

flow has been emphasized in the literature. Recently, Chen et al. [25], using piezoelectric pressure transducers, demonstrated that unsteady pressure pulses obtained from the flow in a convergent-divergent channel are quasi-periodic. They also attributed the occurrence of quasi-periodic to all evolution stages of the sheet to cloud cavitation. This experimental study is reasonably aligned with the experiment implemented by Reboud et al. [39]. Laser Doppler Velocimetry (LDV) measurements of a cavitating flow have also been implemented by Danlos et al. [6] on a venturi profile. This investigation studied the phase portrait obtained from the POD mode time coefficients. The phase portrait implies that the dynamical system governing the cavitating flow is nonlinear, non-periodic, and lives in high-dimensional state-space even in a low-rank framework, including the POD reduced models.

Cavitation stages introduce several instabilities with an array of time and length scales to the system, thereby giving rise to the nonlinear behavior of the flow field. The aperiodic oscillation of the attached sheet cavity length triggers instability in the velocity field and, consequently, pressure fluctuations. This instability has been studied comprehensively by many authors [4, 43, 51, 68, 69, 80]. The velocity difference on the interface of the liquid-phase and the vapor-phase region of the flow field gives rise to another dominant instability associated with Kelvin-Helmholtz mode studied by Lush and Peters [45] and Danlos et al. [6]. This type of instability can be mainly observed in the closure region of the attached sheet cavity and the re-entrant jet. The condensation process and the resultant pressure wave has been studied, and its instability mechanism has been emphasized by Leroux et al. [43].

As mentioned before, since cavitating flow instabilities accommodate an array of distinguishable length and time scales, investigating the switching between different instability modes

is challenging. However, the dimensionality of this complex system can be reduced through proposed methods such as DMD, POD, and CROM. CROM technique takes advantage of two robust data analytic techniques: (1) clustering the phase-state of the dynamical system and (2) transition matrix. The finite-time high-fidelity snapshots of a dynamical system can be represented through a phase portrait. Subsequently, CROM splits this phase portrait into a few clusters, each representing the state of the system statistically. Then, the probability of staying at each state is determined, and the probability values are sorted into a transition matrix. Next, a Markov process is employed to obtain the transition between different states. This process yields a framework through which the instability mechanism and transition between those can be distilled in an unsupervised fashion. Numerous researchers have previously applied the CROM strategy to extract the instability mechanisms statistically. This method can be applied along with DMD and POD to complement the understanding of the instability mechanism. In this regard, CROM separates the dominant instability mechanisms of the dynamical system and obtains the intermittent switching between different instability modes.

Continuous dynamical systems such as fluid dynamics governing equations often can be described in terms of finite degrees of freedom. In this regard, high-fidelity snapshots of some variables defining the dynamical system's state can be decomposed into a set of coherent structures using Dynamic Mode Decomposition (DMD). DMD has been proven to be a robust tool for extracting coherent features of the fluid flow that might facilitate understanding and study of this class of continuous non-linear systems. Orthogonality of the eigenvalues decorrelates the DMD modes, thereby yielding a separation of the time scales of the coherent structures [15]. Separation of the time scales facilitates our understanding of the dominant mechanism of the dynamical system; for instance, one of the brilliant time scale

decorrelations is presented by Noack et al. [10]. They proved that the transient and steady response of the flow field past a circular cylinder could be well-defined through three physically understandable state variables exhibiting significantly different time scales. Besides, DMD spectral analysis yields the growth rate, phase lag, and initial amplitude associated with each mode shape. The initial amplitude of each mode and the phase of the mode, and DMD spectral analysis are connected to the Koopman operator. Koopman operator is an infinite system of linear equations that can define the behavior of a continuous non-linear dynamical system. Likewise, Koopman's observables yield a time scale separation of the continuous system, implying that DMD and Koopman operator power spectral analysis may approximately be an estimation of each other [17].

Moreover, another technique emphasized in the literature, as a reduced-order framework, is POD. POD has been applied previously to decompose the high-fidelity trajectories into hierarchical mode shapes ranked in terms of energy content. This post-processing technique rests on projecting the high-dimensional state-space trajectories on a low-dimensional subspace that conserves the imperative features and energy of the high-dimensional space. POD modes statistically decorrelate [64] eigenvectors representing the mode shapes of the fluid field or the length scales of the coherent structures; however, the behavior of the time evolution of POD modes has not been studied comprehensively in the literature. A better understanding of the complex instabilities in the cavitating flow may be achieved through a close study of the trajectories in state-space and the associated attractors of the POD time coefficients.

6.2 Analysis of the High-speed Images

The periodic shedding of the large-scale cloud accompanied by intermittent small-scale shedding of the vapor structures is observed in the present section. Figure 6.1 depicts the sequential high-speed images from the profile view of the Venturi. In each cycle, the cavitating region grows after the throat of the Venturi section and generates an interface with the liquid phase. The trailing edge of the sheet cavity exhibits strong instability. The trailing edge of the sheet is unstable and gives rise to a series of bubbly coherent structures that are shedding intermittently.

The bottom surface of the sheet at the closure region appears to detach from the wall, and a strong re-entrant jet composed of the liquid phase, shown with the red arrows, is traveling toward the leading edge of the cavity. In the same frame, another re-entrant jet appears on the flow field region with a high void fraction. In the next frame, the sheet cavity length-scale instability leads to the shedding of a partial vapor structure. As a result, the length of the sheet cavity decreases, and the re-entrant flow travels further beneath the cavity and reaches the leading edge. As the partial coherent vapor structure is convicted to the downstream, the structure is distorted due to the pressure gradient. It gives rise to several incoherent vapor structures and finally dissipates out due to the condensation process. Meanwhile, the sheet cavity begins to recover its length by accumulating small vapor structures. The same sequence of events, as mentioned above, is observed until frame 6; shedding of partial coherent vapor structure, distortion of the vapor structure in the downstream, and finally dissipation process. The large-scale cloud cavitation shedding begins in frame 7. At frames 8 and 9, the re-entrant jet impinges on the interface of the cavity at a location very close to the leading edge, then cuts the sheet cavity into two parts and results in the formation of a vapor cloud. The re-entrant jet exists persistently underneath the cavitation, and its

corresponding thickness and velocity fluctuate aperiodically. Based on the flow field images, it is observed that the cloud cavitation is composed of multiple time and length scales. In the present flow condition, the time scales are not necessarily multiple integers of one another; therefore, cloud cavitation shedding occurs quasi-periodically.

The images obtained from high-speed photography may also be used to study the Kelvin-Helmholtz (KH) instability. Due to an interface between vapor and liquid phases, the streams of velocity and the density are distinct in these two regions. The velocity vector field in the region close to the interface of two phases depicts an evident variation of the velocity. The re-entrant jet underneath of the sheet cavity leading edge perturbs the interface of the two streams; look at figure 6.1. Besides, the liquid phase over the sheet cavity also impinges on the interface of the two phases through a vertical velocity component. The flow becomes unstable and gives rise to the (KH) instability, Given a small perturbation on the interface of the two streams of vapor and liquid phases. Without the perturbation, the flow is in neutral stability and acts as two strata with different velocities and densities. After introducing the perturbation on the interface of two layers of flow with a shear effect, the KH instability mixed up the two strata through inertial forces. KH instability uses up the two species' kinetic energy, and the instability evolves until two layers of liquid and vapor begin to mix up. Figure 6.1 shows the nonlinear stage of the KH instability in which the sheet cavity interface is rolling up in a vortical pattern.

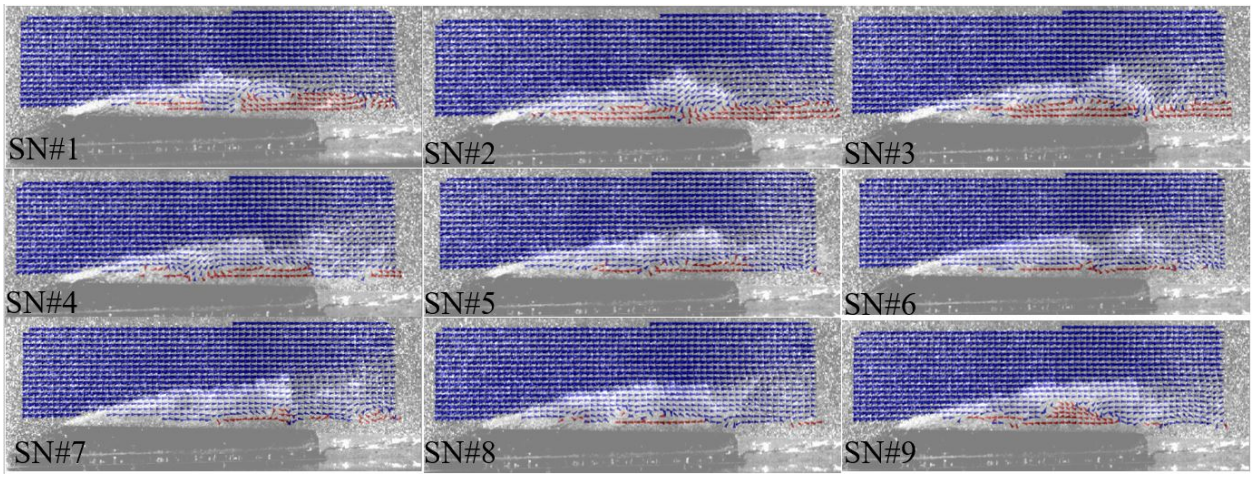

Figure 6.1: Visualization of the velocity vector field overlapped with the raw images from high-speed photography. Illustration of the re-entrant jet, shear instability, intermittent cloud shedding and condensation process as it occurs in a Venturi-type profile at $Re = 15,000$ and $\sigma = 1.95$. The blue (red) vector field depicts the stream-wise velocity (re-entrant jet). Frame # 1-3 depicts a strong re-entrant jet (red arrows) of the liquid phase followed by the intermittent cloud shedding. Frame # 4 illustrates the vapor structures' dissipation as they are convecting on the downstream. Frame # 7-9 shows the convection of the large-scale cloud shedding.

6.3 Technique # 1: Applications of DMD to the Flow Past the Throat of the Venturi Test Section

6.3.1 Application and results of DMD technique

As shown in sections 6.2 and 6.1, in the current flow condition, cavitating flow is composed of multiple shedding scales and possibly with distinct time-scales. The cavitating flow is composed of multiple frequencies due to dominant large-scale shedding followed by low-rank partial shedding. DMD technique isolates the segments of the time signal evolving with a unique frequency. Furthermore, DMD detects the spatially coherent structures associated

with each frequency, thereby yielding a framework through which the cloud shedding scale can be studied. The DMD method achieves this through an approximation of the Koopman operator modal decomposition.

Each snapshot of the given dynamical system, i.e., velocity vector field, can be rearranged into a vector in time, time step k. Likewise, all snapshots may be rearranged into some vectors yielding the sequential, $k = 1, ..., m$, state of the dynamical system. Instead of working with the state measurements obtained from PIV, one may use all possible functions of the PIV measurements called observables and stack them into an infinite vector called functions of measurements. The action of the linear Koopman operator, $\mathcal{K}$, on the observables advances the dynamical system one-time step forward in time, yielding the state of the dynamical system one time step in the future. Koopman operator is a linear, infinite-dimension matrix, and in practice, it needs to be approximated with a finite-dimensional linear matrix. The low-rank behavior of the complex nonlinear data of the flow field is described through spectral decomposition of the Koopman operator. The spectral decomposition of the Koopman operator yields the mode shapes and eigenvalues of the state of the dynamical system. The mode shapes dynamic behavior is linear in time. Therefore, this method yields a spatially coherent structure and the associated unique frequency.

DMD algorithm has successfully been employed to identify the underlying physics from the data of complex flow fields. The technique extracts finite low-rank coherent structures from the high-dimensional dynamical system. The low-rank system contains the major portion of the energy of the high-dimensional system. Such a system is highly interpretable in terms of the length scales of the coherent structures and their corresponding linear time dynamics.

DMD technique complements the previous observations of the KH instability in the cavitating flow extracted from the raw high-speed photography. The sheet cavitation generates

a shear layer formed in the present study due to the discontinuity of velocity between the liquid-phase and high void fraction region. This shear layer gives rise to the KH instabilities that eventually generate coherent structures of the vapor shedding into the wake. To characterize this instability DMD technique has been utilized. DMD technique separates the time scales of distinct instabilities mechanisms. i.e., it separates the time scales of the instabilities that arise from the shear layer velocity discontinuity between two phases and KH vortices shedding (or cloud shedding). Besides, the spatial structures of these instabilities are obtained and visualized through iso-contours of the eigenvectors. The wavenumber of the distinct instabilities is extracted from the iso-contours of the eigenvectors. Furthermore, DMD provides a quantity for the growth (or decay) rate of the KH instability process that eventually leads to the detachment of cloud cavitation.

6.3.2 Analysis and discussion of DMD results

Kelvin-Helmholtz instabilities developed at the interface, and vaporizations and implosions of cavitating structures inside the vortices were observed. DMD technique has been applied to extract the coherent structures from the snapshots of the fluctuating component of the velocity vector field of the liquid phase past the throat of the Venturi profile. Representative DMD mode shapes are displayed in figure 6.2 using the magnitude of the velocity vector field of the liquid phase in the plane of the laser sheet. Figure 6.2 presents the modes associated with the labeled eigenvalues and the initial conditions in figure 6.3. The first two modes correspond to the largest wavenumbers, while the higher modes increasingly show smaller wavenumbers. The first two unstable modes are corresponding to the largest coherent structures. The attached sheet cavity creates an interface with the liquid phase, thereby leaving the liquid phase with a large vortical region that expands over the entire Venturi. These modes are well associated with the Kelvin-Helmholtz instability due to

the velocity difference at the liquid phase interface and the attached sheet cavity. Other unstable modes have significantly emphasized the role of the shedding of the cloud and the condensation process. The unsteady re-entrant cavity with the high void fraction creates an interface with the liquid phase. The attached sheet cavity's length begins to fluctuate aperiodically and closes back at the tip of the cavity to form a re-entrant jet. The re-entrant jet interferes with the cavity and liquid phase interface, resulting in coherent structures in the form of a cloud of vapor. Since the inertial forces govern the back propagation of the jet, it yields a non-linear, quasi-periodic behavior. In this regard, the re-entrant jet may move far back into the upstream to interfere with the root of the attached sheet cavity, thereby resulting in a large-scale cloud shedding. However, the re-entrant jet may also travel a shorter distance and impinge on the sheet cavity closer to the tip of the cavity, thereby giving rise to relatively smaller scale cloud cavitation. The condensation of the cloud cavitation in the high-pressure region of the wake results in highly vortical coherent structures in the velocity vector field of the liquid phase. The cavitating cloud time and length scales vary from cycle to cycle. Consequently, their shedding and condensation process form coherent vortical regions in the liquid phase with a range of time and length scales. DMD separates the distinct modes of instabilities, i.e., the separation of the velocity shear instability and cavitating cloud shedding and condensation process. This separation of the instabilities also demonstrated the non-linear, quasi-periodic behavior of the above-mentioned cavitating flow, look at figure 6.3. The dissipation rate of the secondary instabilities, instability due to the cloud cavitation shedding, is higher than the shear velocity instabilities. DMD decorrelates the time scales and identifies several frequencies associated with one of the mode shapes. The largest coherent structure, mode shape 2, yields very large time scales, $\approx 1.8Hz$. The time scales of the other modes representing the secondary instability, modes 3-12, are ranging from the Strouhal frequency to roughly eight times the Strouhal frequency. The spectrum analysis of DMD shows the role of the inertial forces qualitatively due to the convection and

the subsequent break down of the bigger structure into the smaller structure and eventually the molecular dissipation process. Each mode shows a strong time oscillation, but ultimately, the oscillation dissipates out. Figure 6.4 illustrates that an unstable eigenvalue with a positive real growth rate is not observed since the flow asymptotes to an unstable fix point over the temporal observation. These observations well address the equilibrium condition of the flow due to the dissipation terms. The initial condition of the modes, β values, also displays the mixing energy and coherence measure of associated modes for each coherent structure. Notwithstanding with POD chaotic time dynamics, DMD yields a dynamical system that is linear and overdamped; any initial mixing energy, the initial condition of the modes, of the coherent structure exponentially decays. In this regard, DMD separates the coherent spatial structures possessing the mixing energy that goes through a linear dissipation process through time. The mixing energy available for the small scales is higher than the large scales. DMD model implies that the mixing energy corresponding to each coherent structure diminishes temporally, and the small scales lose energy at a higher rate.

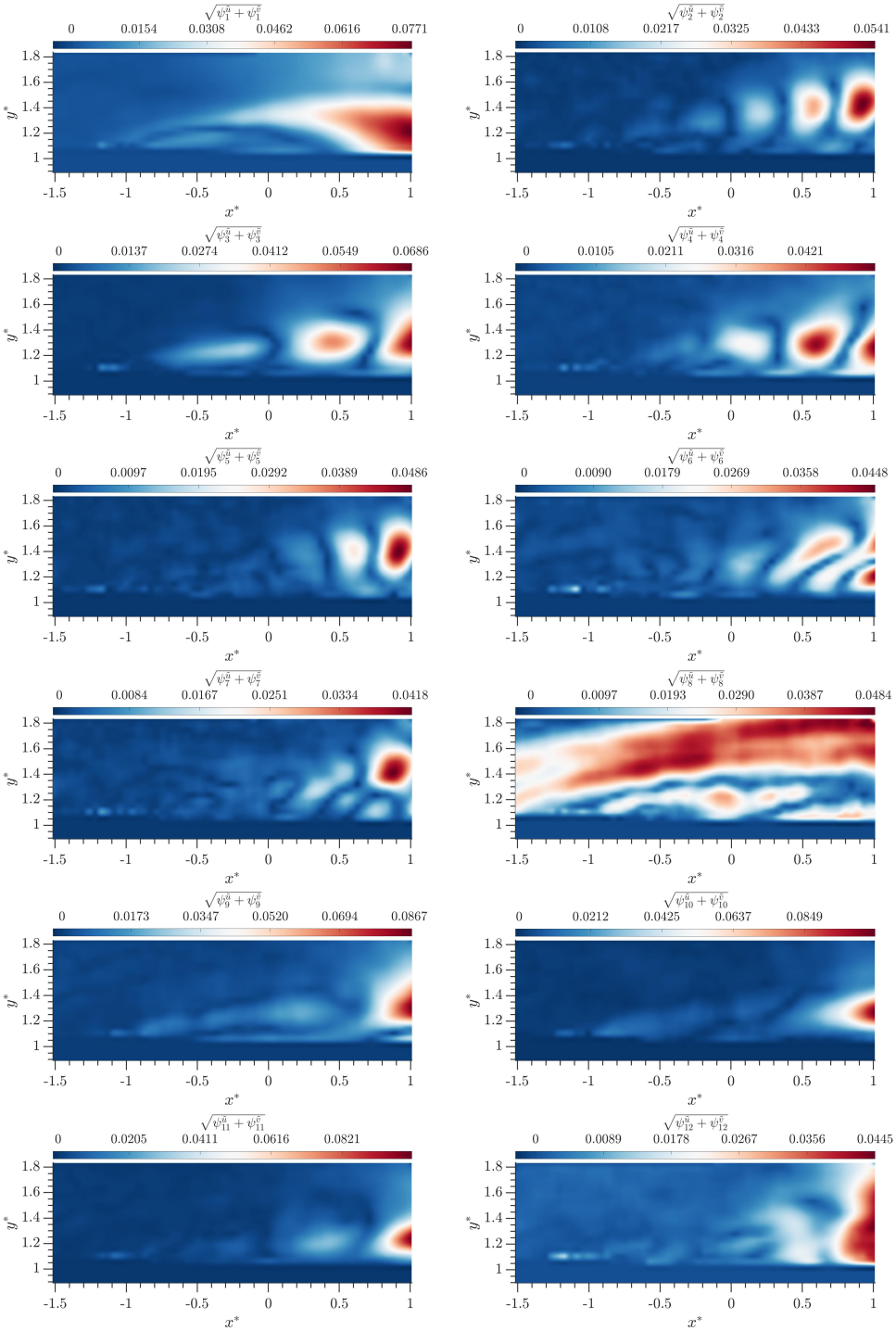

Figure 6.2: Representative of the DMD mode shapes, visualized by the velocity magnitude, for the liquid phase at $Re_h = 15,000$, and $\sigma_{cav} = 1.95$. (a-b) The largest coherent structures correspond to the instability created due to velocity shear on the liquid phase and vapor phase interface, (c-l) unstable branch corresponding to the vortical coherent structures of the liquid-phase induced by quasi-periodic shedding and condensation of the cloud cavitating.

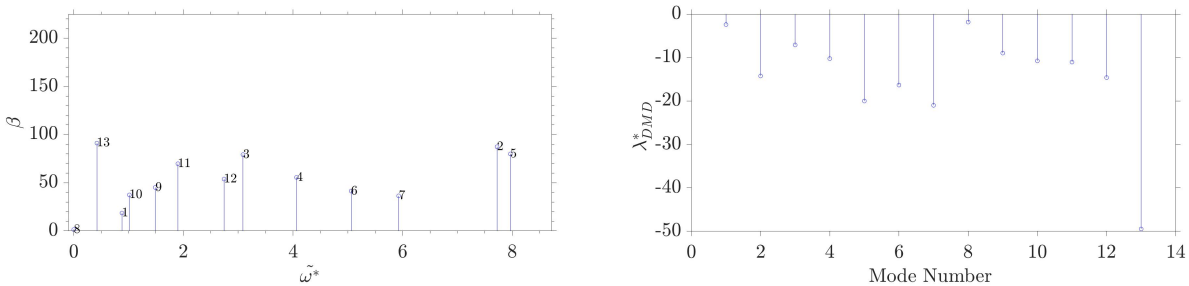

Figure 6.3: (a) DMD spectrum versus the initial amplitudes of the mode shapes associated with the velocity magnitude of the liquid phase at $Re_h = 15,000$, and $\sigma_{cav} = 1.95$. (b) Monotonic decay rate associated with each mode.

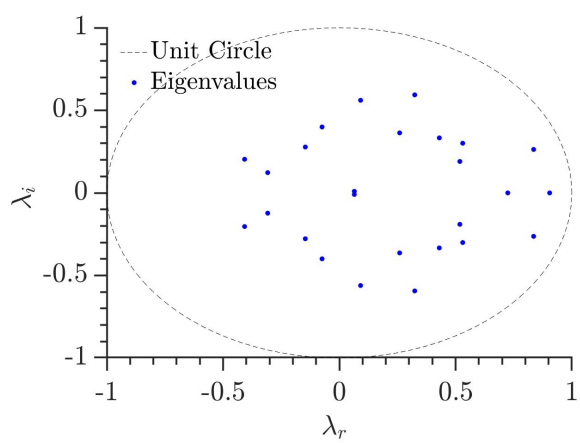

Figure 6.4: Complex eigenvalues of $\hat{A}$ matrix for cavitating flow with $Re =$ and $\sigma_{cav} =$. Eigenvalues lie inside the unit circle implying the convergence, e.g., monotonic decay, of the corresponding mode.

6.4 Technique # 2: Applications of POD to the Flow Past the Throat of the Venturi Test Section

6.4.1 POD technique application

The first modal decomposition technique used in this research is POD. Since each resulting POD mode shape acquires a unique wavenumber, POD is helpful in the study of the length scale of unsteadiness. POD assigns a maximum energy level for each of the POD modes, knows as singular values. As a byproduct of unique wavenumber for each mode shape, the time coefficients are not orthogonal, resulting in impure frequency content consisting of multiple harmonics. The time coefficient of the POD modes represents the TKE budget available instantaneously for each of the modes. This feature of POD determines the distribution of TKE between different length scales. Besides, the time fluctuations of the energy show the energy path between different length scales. The interactions of POD modes, or the energy exchange between different length scales, can be studied using the coherence measure of the time coefficient signal. Similarly, such a technique can be used to study the energy exchange between the mean flow, slowly varying POD modes, and the modes associated with low wavenumbers. Slowly varying POD modes represent the TKE production range that provides the energy of the inertial and dissipation length scales. Correlation between the time coefficients of the production length scales and the inertial and dissipation length scales displays the mean flow energy extracted by low wavenumbers. This study also shows the stresses imposed by the low wavenumbers on the mean flow.

6.4.2 Nonlinear behavior based on POD dynamics

POD is utilized to investigate the mechanism of the energy exchange between different wavenumbers in the flow field. Previous studies have shown that POD modes yield the instantaneous growth of vortex shedding strength and the limit cycle in the phase space [1, 10, 37, 81, 82]. In the previous models, the vortex shedding dynamics are coupled to mean-field in the wake of the bluff body. The fluctuations of the POD time coefficients are represented as energy flux between the small time scales and large time scales representing the vortices and the mean-field drift, respectively.

The POD mode shapes, time dynamics and the associated power spectral are shown in figure 6.5. From the power spectral density of the signal, the coherence measure has been computed. It is seen that the input, POD coefficient one, and output, POD coefficient two, display a relatively strong coherence of 0.8-0.9 over a wide frequency range figure 6.6. Coherence function diminishes at very low frequencies and for high frequencies as well. From the power spectral density, most of the energy has been concentrated in the relatively lower frequencies, in the range approximately from 50 Hz to 700 Hz, where the coherence is high. High coherence implies that a linear relationship exists between the POD modes corresponding to the largest length scales. Besides, the probability distribution of the phase angle between the POD coefficients of modes one and two indicates an intermittent behavior. When mode one oscillations are strong, mode two oscillations are weak, and the converse is also observed, look at figure 6.6. Likewise, POD coefficients associated with modes three and four yield a strong coherence in a comparably shorter range. The PDF of phase angle deviates from the Gaussian distribution, and the peak is lower. It can be cautiously notified that the observations mentioned above indicate that the large scales linearly exchange energy to one another in the corresponding frequency range, or one drives the oscillations of the other. On the other hand, the coherence between any other pairs of the POD coefficients yield

very low values and the associated phase angle displays a uniform PDF, thereby implying that a non-linear relationships govern the energy exchange of the small length scales. For further analysis, the influence of the other variables including the velocity field fluctuations of the vapor phase and pressure fluctuations on the energy exchange process needs to be investigated to improve the confidence of the analysis.

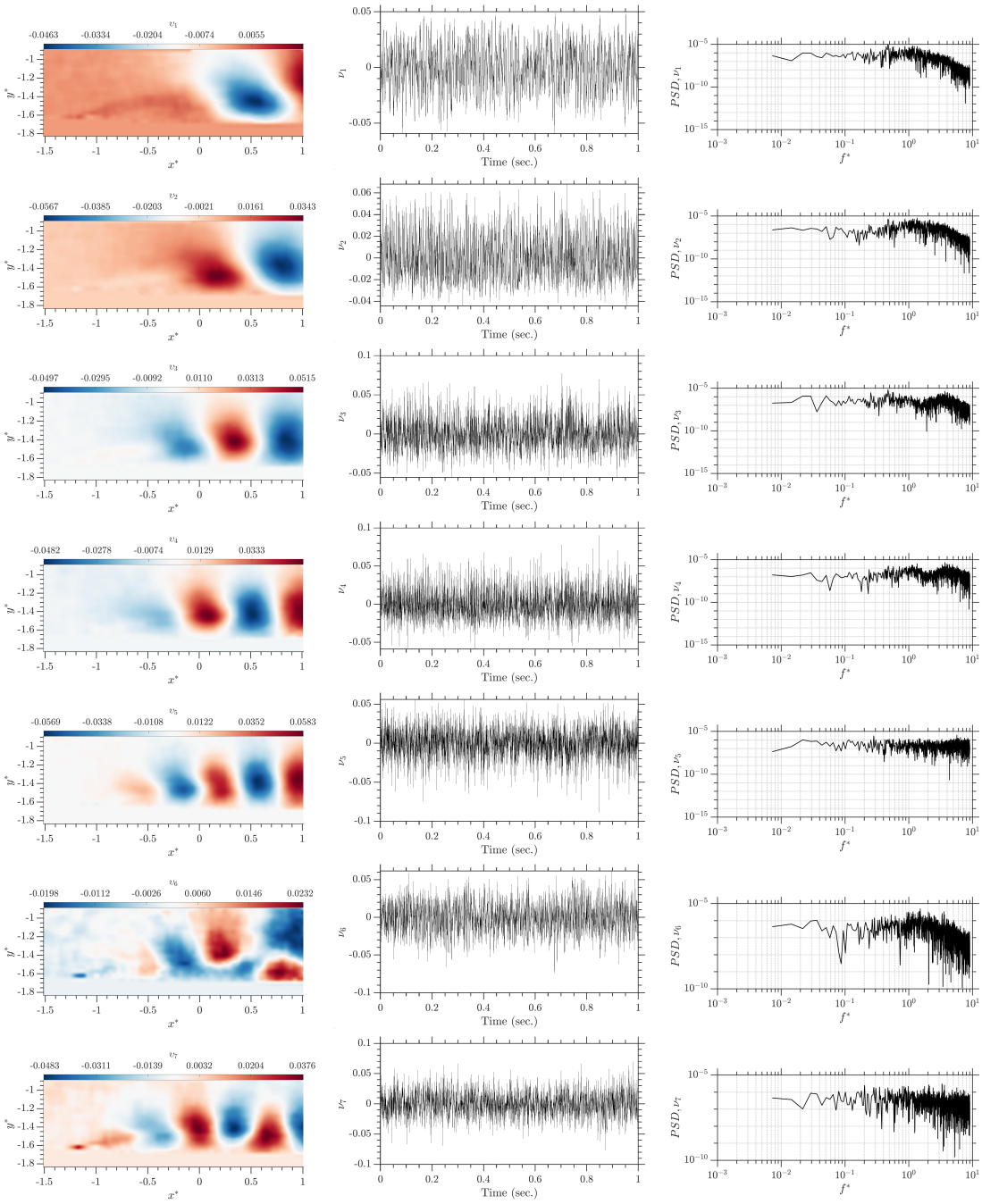

Figure 6.5: (a) POD mode shapes of the liquid-phase velocity components. The flow is visualized using the iso-contours of the transversal velocity component. (b) POD time coefficients of the transversal velocity of the first eight modes. (c) Power spectral of the time coefficients of the transversal velocity of the first eight modes

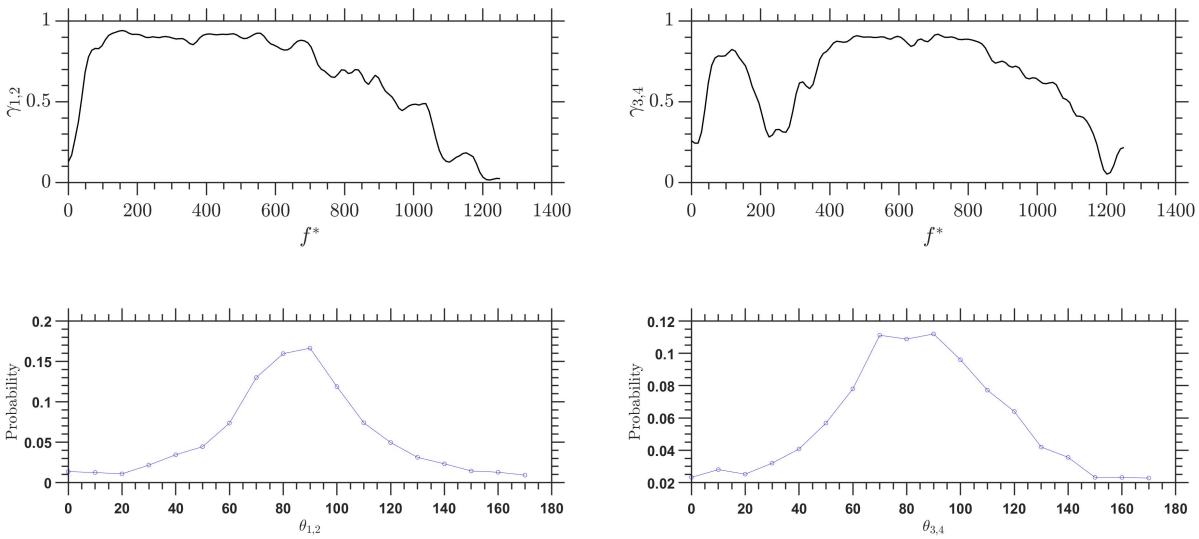

Figure 6.6: The figure depicts the spectrum of the coherence measure associated with the POD mode pairs (a) one and (b) two. The high value of the coherence indicates a linear interaction between the signals, while low coherence indicates a correlation with the nonlinear phenomenon or noise. The figure shows the PDF of the phase difference between the POD time dynamics of mode pairs (c) one and (d) two. The high probability around 90° suggests that the kinetic energy mutually is transferred between the corresponding POD modes.

Additionally, the wavelet coherence can detect the scale of the relationship between two-time series and determine whether that relationship changes in the time-frequency map. This method can be applied to estimate the fraction of the energy of the output that is not obtained or derived by the input at a particular frequency. Besides, it quantifies the output energy, for instance, the region with relatively high values of coherence that is uncorrelated with noise or other inputs. The decomposition via POD yields a broad insight into the instantaneous distribution of mixing energy between distinct length scales and their corresponding time dynamics of the mixing energy. Moreover, it obtains the exchange of the energy between different coherent structures with distinct length scales. Since the high-dimensional data of the velocity field is embedded in four dimensions in the phase-space and the energy interaction between pairs of the first four POD are dominantly linear, the sum of

the energy of these components are studied in this section. Here, the kinetic energy available for the length scales that can interact linearly and in a reversable fashion are investigated. The first and second modes depict the largest length scales possessing the highest energy for the transport of momentum. The instantaneous phase angle between these eddies are $\frac{\pi}{2}$ implying that they mutually transfer energy through a linear mechanism. Furthermore, The wavelength coherence of the first pair of POD is used to identify frequency range within which two time coefficients are covarying. This pair shows a coherence greater than 0.9 in the $f_s^* \approx 0.03 - 1$ bands and for the entire lifetime of the oscillations, with significantly lower coherence outside of these time scales. Low coherence associated with large time scales implies that they are not mutually correlated linearly. The low coherence also suggests that independent processes operates at the large time scales, $f_s^* < 0.03$. The vectors in figure 6.7 indicates the phase lag between first mode pair at short-term time windows. The vectors are depicted where the coherence measure is higher than 0.8. In the 0.05 second cycles, mode one and mode two are about $\frac{\pi}{2}$ out of phase: the peak of the kinetic energy of mode one and mode two are not synchronous in $f^* = 0.03 - 1$. This phase lag appears constant over the higher frequencies, while the phase angle decreases for lower frequencies. The first and the third mode display a high coherence measure for the larger time scales, $f_s^* > 0.25$. The low phase lag and high coherence measure indicates that the peak of the kinetic energy of the modes are concurrent and they interact linearly. These results suggest that in the entire lifetime of the signals modes one through four strong interactions through a linear phenomena. It should be noted that the interactions of mode one with modes two and three occurs in the time scales where the power spectra of both modes show relatively high power. In coherence measure of modes one and four there is low coherency outside of the band,$f_s^* \approx 0.3125 - 0.25$, suggesting that the interaction of mode one and four is either through non-linear processes or noise operates at the smallest and largest time scales. The mode two and mode three show a high coherency in shorter, intermittent time intervals and shorter frequency bands. The

intermittent change in these modes appear as an interval of low coherency for time duration of $0.05sec$, especially in the $f_s^* \approx 0.3125 - 0.125$ band. Besides, the phase lag between the mode two and mode three is $\approx \frac{\pi}{4}$. The mode two and mode four show high coherence in the $f_s^* \approx 0.3125 - 0.125$ band for the entire lifetime of the data and their corresponding phase lag is lower than the previous case. Occasional strong interactions also is observed for the higher and lower time scales than the above-mentioned interval, $f_s^* = 0.3125 - 0.125$. Mode three and mode four show a high coherence in the high frequency band and an intermittent time intervals of high coherence in the low frequency band. These observations suggest that the interactions between time dynamics of modes one, two, three and four are affected by a non-linear terms or uncorrelated noise that is most probably triggered by the time dynamics of mode three and four.

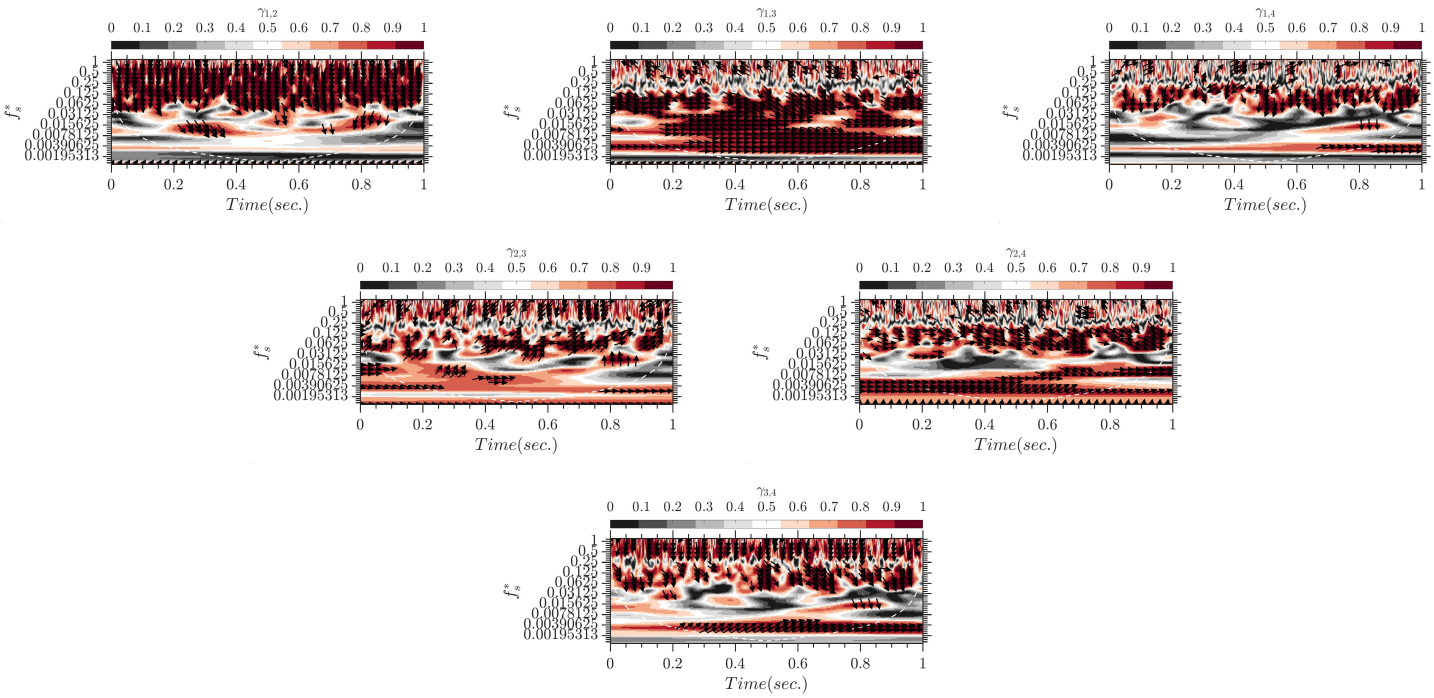

Figure 6.7: The figure presents the wavelet coherence of the first four energetic POD mode coefficients: the scalogram of coherence measure. Contours depict the coherence measures. The vectors indicate the phase difference between POD time coefficients only where the coherence measure is greater than or equal to 0.8. A vertical arrow displays an out-phase pair of signals, and a horizontal arrow denotes an in-phase pair of signals. A dashed white line is used to discriminate between the data susceptible to the edge effects from the graph's high-fidelity region.

In this section, to investigate the dynamics of the mode shapes of POD, the time records, power spectral, and two-dimensional representation phase space of the POD time coefficients are studied. The PDF of the FTLE has been shown to demonstrate the short-term behavior of the POD time coefficients trajectories in the state-space. The LLE of each POD time coefficient has been acquired, and comments have been made on the short-term and global behavior of the phase space trajectories. The first eight POD modes and their corresponding time coefficients and power spectral are shown in figure 6.5. Since POD decorrelates the length scales, each mode shape represents the length-scale of one of the coherent structures; besides, these modes are phase-shifted in the streamwise direction. The power spectral of

each mode yields several peaks, implying the energy is concentrated in distinct frequencies. Since the frequencies corresponding to the peaks value in power spectral are not multiple integers of each other, the temporal coefficients of these modes are quasi-periodic. This well demonstrates that in this regime of non-dimensional system parameters, the frequencies of the modes are not "locked-in"; therefore, the dynamical system never exactly repeats itself. Since the mean period of the first three modes is significantly greater than the high order modes, the time scale of the higher modes is very low. In other words, With an increase in the frequency of coherent structures, their length scales are decreasing.

The state-space of the POD time coefficients of mode pairs and the corresponding numerical simulations obtained from the model, Eq. (6.1), are displayed in figure 6.8. The trajectories of all mode pairs close on themselves, implying that the attractor embedding dimensions are higher than two. The minimum embedding dimension has been acquired employing Eq. (4.58). For $d = 4$, the number of FNN is minimum for all POD modes, implying the attractor can be accommodated in four dimensions. Since the POD coefficients power spectral contains multiple dominant harmonics and cannot be expressed as a ratio of integers, the complete geometry of the attractors cannot be identified from the state-space in two dimensions.

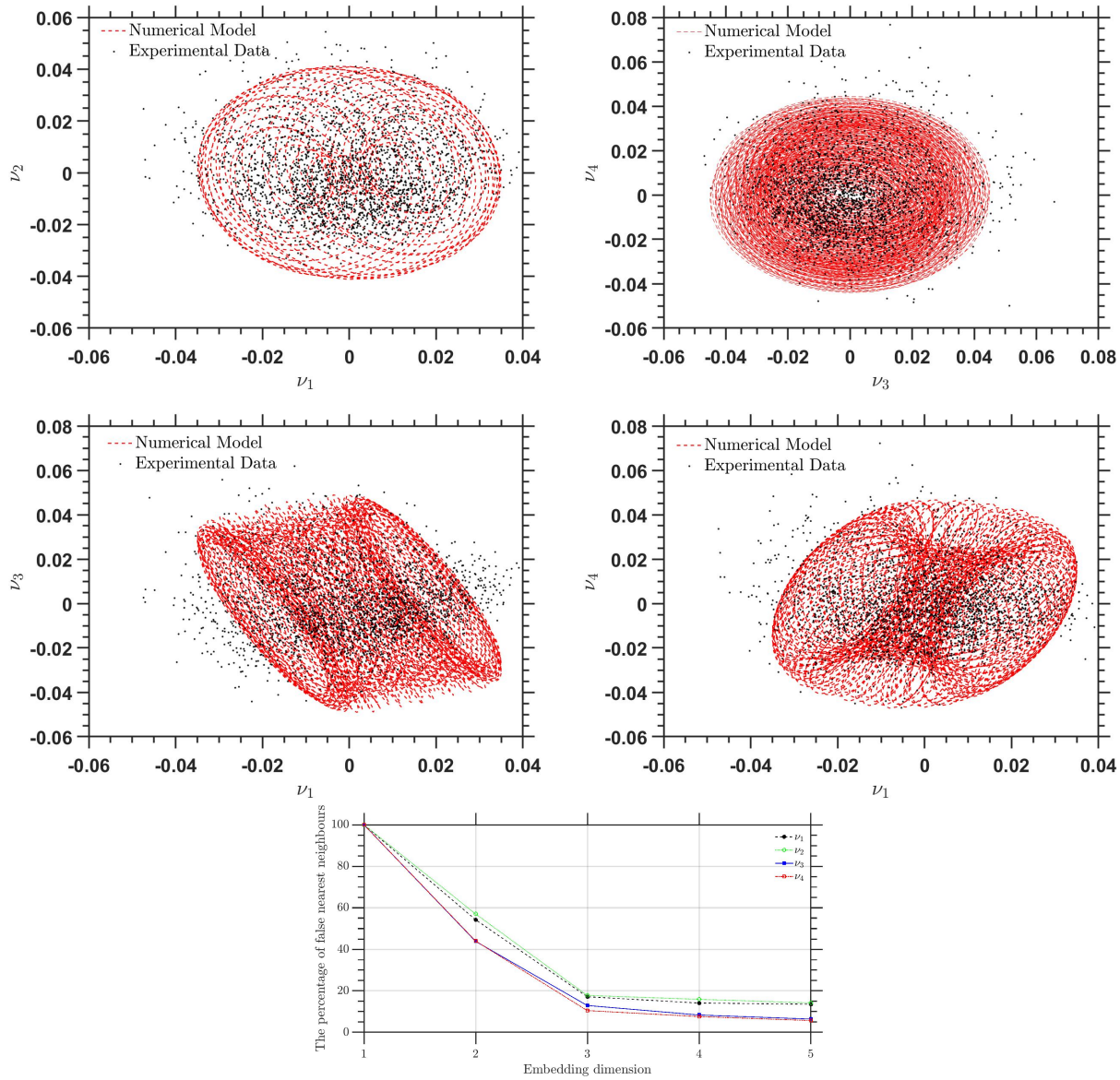

Figure 6.8: Representation of the trajectories in the state space for (a) the first pair, (b) the second pair, (c) modes one and three, and (d) mode one and mode four of the POD time coefficients associated with the transversal velocity. The percentage of the FNN versus the number of embedding dimensions for the first four POD coefficients trajectories in the phase-space. FNN is computed at the symbol points and is connected by linear regression.

$$
\begin{aligned}
\frac{d\nu_1}{dt} &= z_{1,1}\nu_1 + z_{1,2}\nu_2 + z_{1,3}\nu_3 + z_{1,4}\nu_4 \\
\frac{d\nu_2}{dt} &= z_{2,1}\nu_1 + z_{2,2}\nu_2 + z_{2,3}\nu_3 + z_{2,4}\nu_4 \\
\frac{d\nu_3}{dt} &= z_{3,1}\nu_1 + z_{3,2}\nu_2 + z_{3,3}\nu_3 + z_{3,4}\nu_4 \\
\frac{d\nu_4}{dt} &= z_{4,1}\nu_1 + z_{4,2}\nu_2 + z_{4,3}\nu_3 + z_{4,4}\nu_4 + z_{4,16}\nu_1^3
\end{aligned}
\tag{6.1}
$$

To quantify the sensitivity of the nearby trajectories to divergence or convergence in a short time, FTLE has been computed for three distinct intervals of $L = 1, 10, 100$ and for four POD time coefficients. PDF of the FTLE for three distinct intervals are shown in figure 6.9. For a finite swarm of trajectories with a size less than the total samples, the Lyapunov exponent is negative; the trajectories in the state-space of the dynamical system converge into a generic attractor, or the geometry of phase-space is rapidly shrinking. Conversely, for short-time evolution of the trajectories, the Lyapunov exponent is positive, so the trajectories stretched and diverged rapidly in the phases-space, or the geometry of the attractor is dilating. The previous observation means that the dynamical system is chaotic for a finite amount of time, and for some short time, no chaos exists in the system. Thus the dynamical system for some intervals of time is locally unstable yet for others stable. Since the system switches between stable and unstable conditions, the dynamical system exhibits the characteristics of a strange attractor. The LLE of the entire time signal of the POD time coefficients demonstrates the global stability of the modes. The values on Table 6.1 show that modes 1, 2, 3, and 5 are globally stable, while modes 4, 6, 7, 8 are globally unstable. The coherent spatial structures of POD mode shapes represent the highly vortical regions in the flow. Thus, the structures provide an intuition of the mixing length scales and their hierarchy regarding the available

total mixing energy corresponding to each length scale. Besides, the POD time dynamics exhibit the time fluctuation of the strength of the mixing corresponding to each length scale. Since the dynamical system governing the POD time coefficients exhibits the characteristics of a strange attractor with at least a short-time positive Lyapunov exponent, thus a chaotic mixing occurs in this flow field.

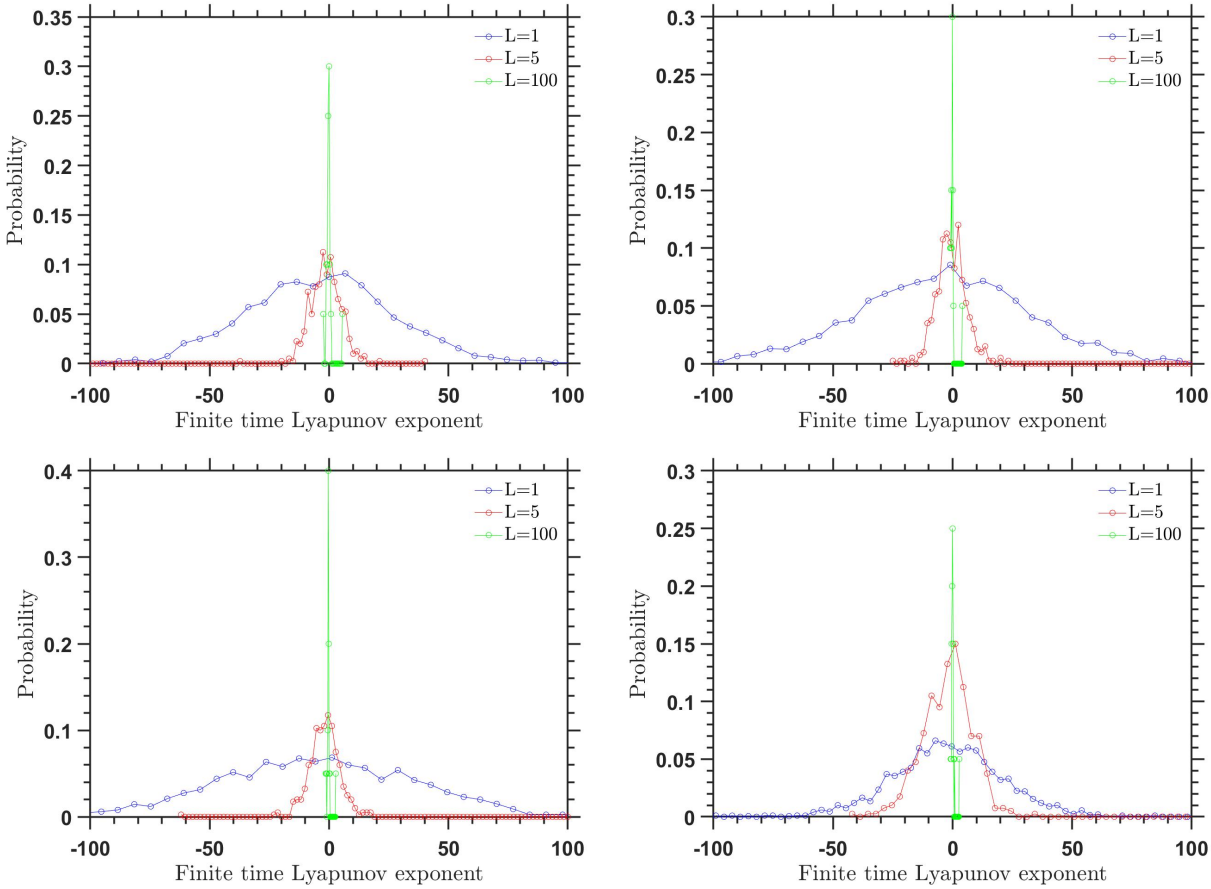

Figure 6.9: FTLE distribution function associated with POD time dynamics of the first four modes for the different realization of time interval samples, $L = 1, 10, 100$.

Table 6.1: LLE, embedding dimensions, mean period, number of the period for the entire sample, and time lag for the time evolution of the temporal coefficients of POD modes.

POD temporal coefficients	$\alpha_1(t)$	$\alpha_2(t)$	$\alpha_3(t)$	$\alpha_4(t)$	$\alpha_5(t)$	$\alpha_6(t)$	$\alpha_7(t)$	$\alpha_8(t)$
Lag τ (ms)	2	1.2	1.2	0.4	0.4	1.6	1.2	0.8
T_{mean} (ms)	8	8	16	2	1	5	2	5
N_T	$125T$	$125T$	$63T$	$500T$	$1000T$	$200T$	$500T$	$200T$
Embedding dimension	4	4	4	4	4	4	4	4
LLE	-0.0267	-0.0757	-0.0350	0.0275	-0.0286	0.0466	0.0579	0.1057

6.4.3 POD time dynamics modeled via system of ODEs

In this section, a reduced-order model is developed for the time dynamics of POD mode coefficients. This model contains the first four dominant modes obtained from the POD algorithm mentioned above. i.e., it accounts for the first four harmonics associated with the highest length scales. In the following, a system identification approach has been performed that addresses the structure of the dynamical system and further tunes the parameters. The POD of the high-fidelity instantaneous velocity field yields mode shapes and time dynamics. The signals representing the time dynamics of the modes are utilized to obtain a system of ODEs. Here it is assumed that the domain is sufficiently large that the first four length scales are conserving energy, and they only exchange energy between each other.

Since the conservation of mass equations and momentum equations for both species are fairly sparse polynomial forms, only a few terms of the polynomial may describe the physics of the problem. To make the proposed model interpretable, the tuning of the coefficients, ζ_i, are subjected to l_1 regularization with varying $\lambda_{reg.}$. Each realization of $\lambda_{reg.}$ provides a dynamical model, for example, an ODE, with different closure coefficients. Besides, as λ_{reg}

increases, the number of non-zero closure coefficients increases, thereby yielding a more complex model that is highly exposed to overfitting. In this regard, for the different realization of $\lambda_{reg.}$, the performance of the model in terms of the Mean Squared Error (MSE) and the uncertainty bar is evaluated. Figure 6.10 illustrates the cross-validation error for the POD time dynamics for different realization of $\lambda_{reg.}$ It is assumed that the uncorrelated noise has been eliminated in the regularization process, and the shape of the attractor obtained from the ODEs is not affected by an external perturbation source such as noise. The probability distribution of time dynamics of the first four energy-carrying POD modes obtained from the numerical simulation and experimental data have been depicted in figure 6.11.

The first ODE, Eq. (6.1), defines the growth rate of the kinetic energy of mode one depending linearly on the instantaneous amplitudes of modes one to four. Mode one draws energy from mode two and is damped by modes three and four. The second mode only extracts energy from mode three and is damped by modes one and four. Table 6.2 shows the coefficients of the model of POD time dynamics.

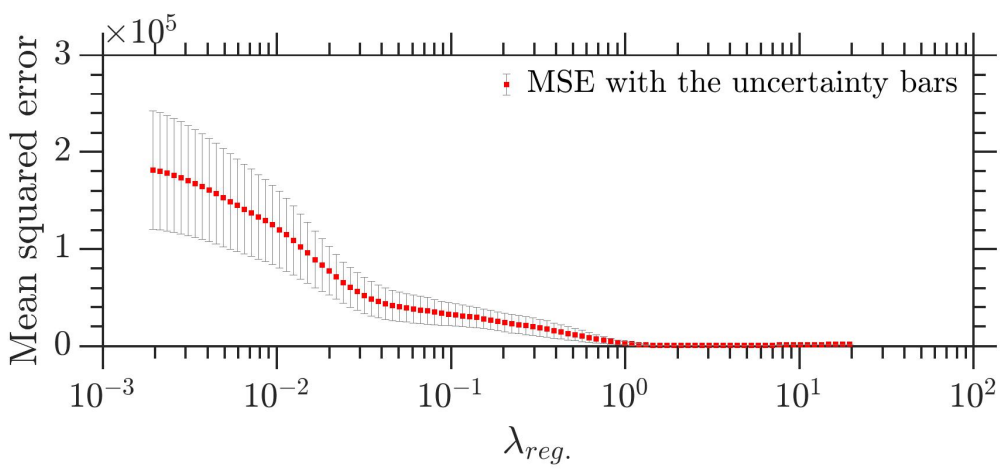

Figure 6.10: Ten-fold cross-validation error for the POD time dynamics for different realization of $\lambda_{reg.}$. Mean Squared Error (MSE) is obtained via cross-validation (red square-shaped dots) and one-standard-deviation grey bars associated with the uncertainty band.

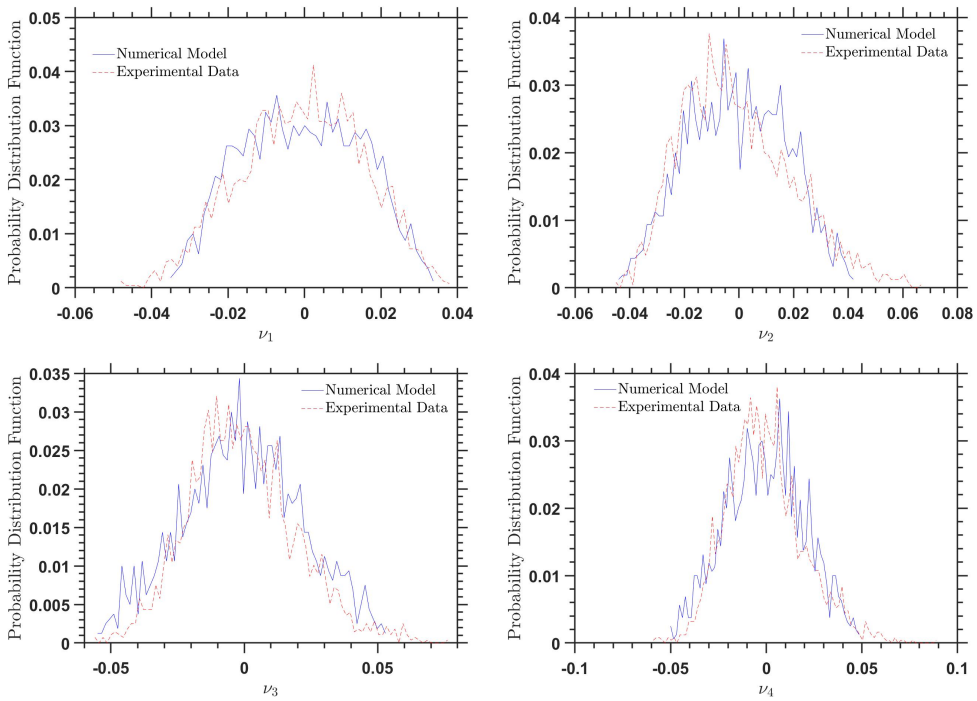

Figure 6.11: POD time dynamics probability distribution functions associated with modes (a) one, (b) two, (c) three, and (d) four obtained from the experimental data (dashed, red line) and the numerical simulation of the coupled ODEs dynamical model (solid blue line).

Table 6.2: Values of the coefficients defining the model of the POD time dynamics, Eq. (6.1)

$z_{1,1} = 0.00062$	$z_{1,2} = 1153.134$	$z_{1,3} = -152.663$	$z_{1,4} = -86.338$
$z_{2,1} = -1153.758$	$z_{2,2} = 0.00011$	$z_{2,3} = 892.651$	$z_{2,4} = -299.965$
$z_{3,1} = 156.564$	$z_{3,2} = -875.581$	$z_{3,3} = 0.00013$	$z_{3,4} = 1814.536$
$z_{4,1} = 59.616$	$z_{4,2} = 278.634$	$z_{4,3} = -1763.784$	$z_{4,4} = 0.00015$
$z_{4,15} = 31818.929$			

6.4.4 Interactions of the POD length scales

Figure 6.12 shows the spatio-temporal structures of the first two POD modes from low-frequency drift flow, the time dynamics, and the PSD of the associated modes. These modes

are associated with the lowest wavenumbers. The spectra of the modes coefficients exhibit a dominant peak at $f_s^* = 0.48$ followed by several sub-harmonics and super-harmonics. Since dominant frequencies of mode one become close to mode two, the phenomenon of lock-in happens. The wavelength of the structures is approximately similar, and its length scale is comparable with the length of the test section. Clearly, the time dynamics of all the drift modes show aperiodic oscillations with intermittent modulation in the peaks. These modes are corresponding to the energy-carrying modes with very low wavenumbers. It is observed that the time dynamics of mode two are influenced by a drift flow whose time scale is on the order of 0.4 sec. The intermittent modulation in the time dynamics demonstrates that these modes have acquired stochastic kinetic energy.

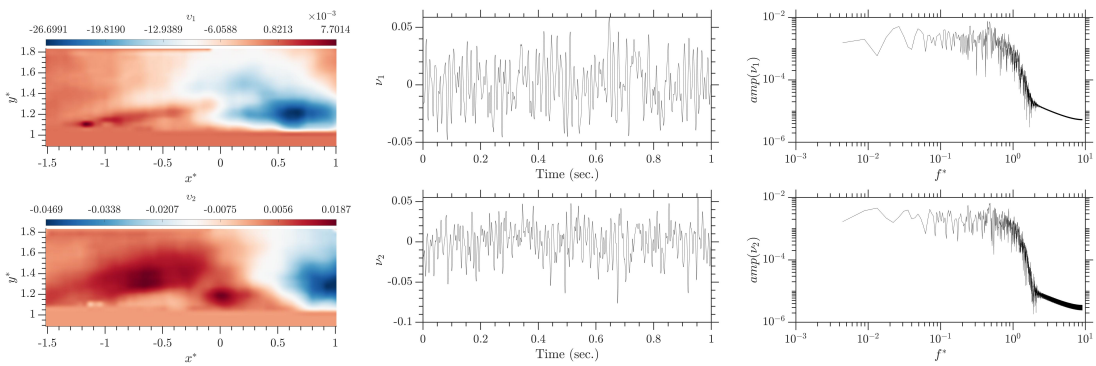

Figure 6.12: (a) 2-dimensional (2D) POD mode shapes of slowly varying drift flow. Shown are the iso-contours of the transversal velocity components. (b) Time fluctuation of the first two POD modes, (c) and the associated spectrum. Time fluctuation of the modes represents the fluctuations of the available energy of the corresponding mode.

Figures 6.13 and 6.12 show the spatio-temporal structures of the first two POD modes from KH instability, and the first five POD modes associated with the vapor cloud-shedding, the time dynamics, and the PSD of the associated modes. The wavenumbers are larger than the drift flow modes. It is expected that the slow varying drift flow, KH instability, and cloud-shedding are linked via a TKE energy exchange mechanism. The high energy drift oscillations are the key aspect of oscillations due to KH instability and cloud cavitation.

In this section, the connection between the mechanisms mentioned above of instability is examined. A significant exploration is presented on the phase relationships between the modes time dynamics to shed light on the expected causality links.

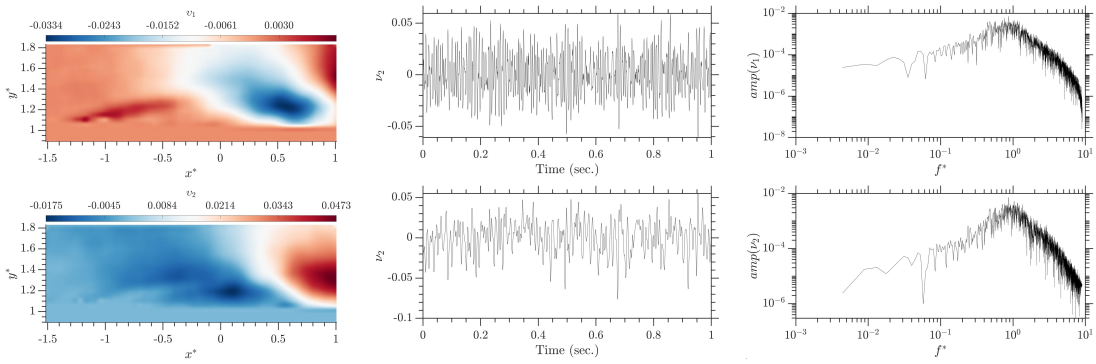

Figure 6.13: (a) (2D) POD mode shapes of KH instability. Shown are the iso-contours of the transversal velocity components. (b) Time fluctuation of the first two POD modes, (c) and the associated spectrum. Further information can be found in figure 6.12

The coherence plots between the modes shape of the drifting flow and the KH instability has been shown in figure 6.14. There is a cone shape of occurring regions of significant coherence, $f_s^* \approx 0 - 0.5$. There are intermittent occurring regions of significant coherence at $f_s^* \approx 1 - 2$. Straight-down vectors are indicating the lead of drift flow with respect to the KH instability. This observation demonstrates a particular period when drift energy is high, while the energy budget of KH instability is low. Due to the lead of drift flow signal, it provides the energy of KH instability through a linear process. The second mode, the drifting flow, and KH instability yield an opposite behavior: KH instability leading the drifting flow. The broadband high coherence measure between KH instability and drift flow is associated with their almost unvarying exchange of TKE at low wavenumbers. On the other hand, the significant coherence measure between KH instability and cloud shedding modes is time-variant. At $f_s^* \approx 0.25 - 1$, arrows indicating the relative phase relation are pointing left, e.g., an anti-phase relationship, or pointing down, showing that the KH signal is leading the cloud shedding signal. High coherence time intervals are intermittent and only

yield significant coherence aperiodically. There is an aperiodic energy exchange between the KH instability and cloud-shedding modes that rise to intermittent shedding regimes in the flow field.

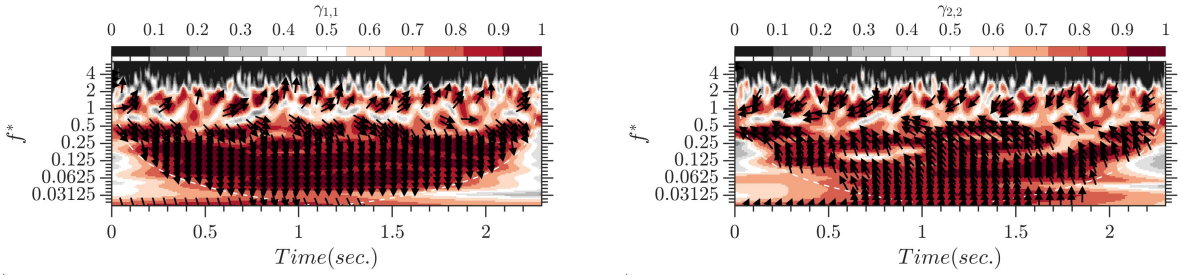

Figure 6.14: Representation of the linear link between the POD modes of low wavenumber drift flow and KH instability. The wavelet coherence between drift flow and KH instability time dynamics: the scalogram of coherence measure. The first subscript defines the mode number of the drifting flow, and the second subscript represents the mode number of the KH instability. Further explanation of the graph is illustrated in figure 6.7.

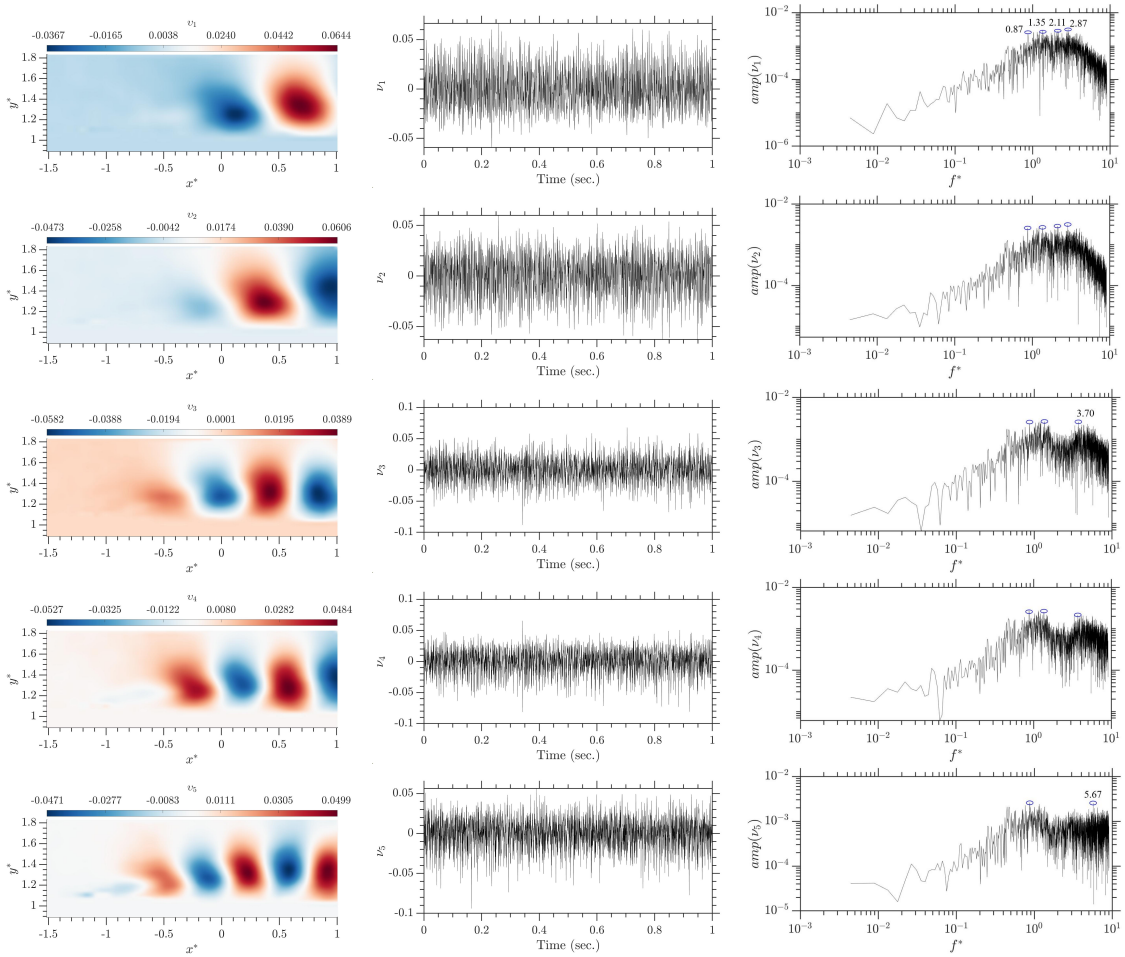

Figure 6.15: (a) (2D) POD mode shapes are associated with high-frequency cloud shedding. Shown are the iso-contours of the transversal velocity components. (b) Time fluctuation of the first two POD modes, (c) and the associated spectrum. Further information can be found in figure 6.12.

Cavitating flow shows some dominant oscillatory behaviors shown in the previous analysis. For instance, slow varying drift flow, KH instabilities, and vapor cloud-shedding are some of the dominant oscillatory dynamics observed in the flow field. Oscillating coherent structures can define cavitating flow with low-frequency drift flows and the modulation of the high-frequency oscillation of the KH instabilities and vapor cloud-shedding. In practice, the combination of POD modes associated with KH instabilities and vapor cloud shedding can reproduce different regimes observed in the cavitating flow past the throat of the Venturi-test

section. Figure 6.16 displays three dominant flow patterns occurring in the cavitating flow.

- The preceding observation shows that the velocity vector field's oscillations inside the attached sheet cavity are comparably low. In contrast, these oscillations are significant at the leading edge of the attached sheet cavity. Frames $\#2-4$: Premature condensation of the vapor cloud has been observed in the leading edge of the attached sheet cavity. As a consequence of the condensation, the length of the attached sheet cavity oscillates rapidly. In frames $\#2-4$, the interaction of the first pair of POD associated with the vapor cloud-shedding explains velocity vector field fluctuations as premature condensation occurs, look at figure 6.17. In these snapshots, the amplitude of both POD modes associated with cloud-shedding is greater than %65, while the amplitudes of the other modes are insignificant. The previous result is due to the fact that POD pairs' wavelengths are shifted. The phase-shifted relationship may lead to destructive (constructive) interference of the modes that result in low (high) amplitude oscillations.

- frames $\#8-18$: Large-scale vapor cloud is transported to the downstream where the pressure field is comparably higher than the throat of the test section—the pressure recovery results in the collapse of the bubbly structures. In frames $\#8-18$, the amplitude of the first POD associated with the cloud-shedding is high, while amplitudes of all other modes are comparably low, look at figure 6.17. The observation mentioned above emphasizes that the transversal velocity fluctuations on the downstream region are significantly higher than the other flow regions.

- frames $\#20-46$: small-scale vapor cloud is shedding on the downstream. Since the pressure increases along the length of the test section, vapor structures go through distortion, and they dissipate in the wake. In this case, it is observed that the amplitude

of the pair of modes corresponding to KH instability and slowly varying drift flow is high. In contrast, the amplitude of the modes corresponding to cloud shedding in most of the snapshots is low.

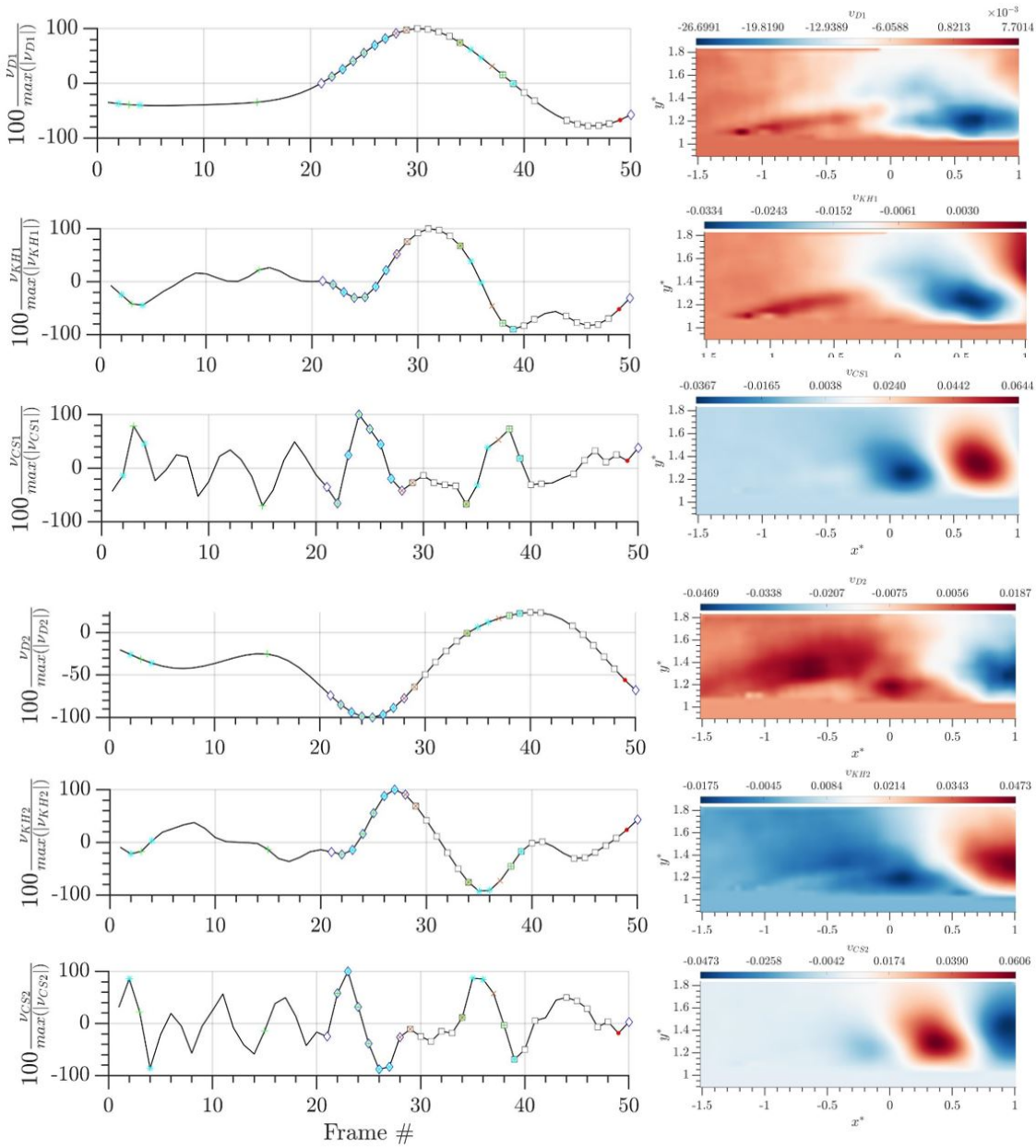

Figure 6.16: POD time dynamics of the drifting flow, KH instabilities, and cloud-shedding POD mode pairs. Red circles (blue diamond) display the snapshots where the amplitude of the first (second) POD mode of drift flow is greater than %65. Gray squares (orange crosses) display the snapshots where the amplitude of the first (second) POD mode of KH instabilities is greater than %65. Green plus signs (cyan asterisks) display the snapshots where the amplitude of the first (second) POD mode of cloud-shedding is greater than %65. First two dominant POD modes of the drifting flow, attached sheet cavity, and cloud shedding. The flow is visualized through the contours of the transversal velocity component.

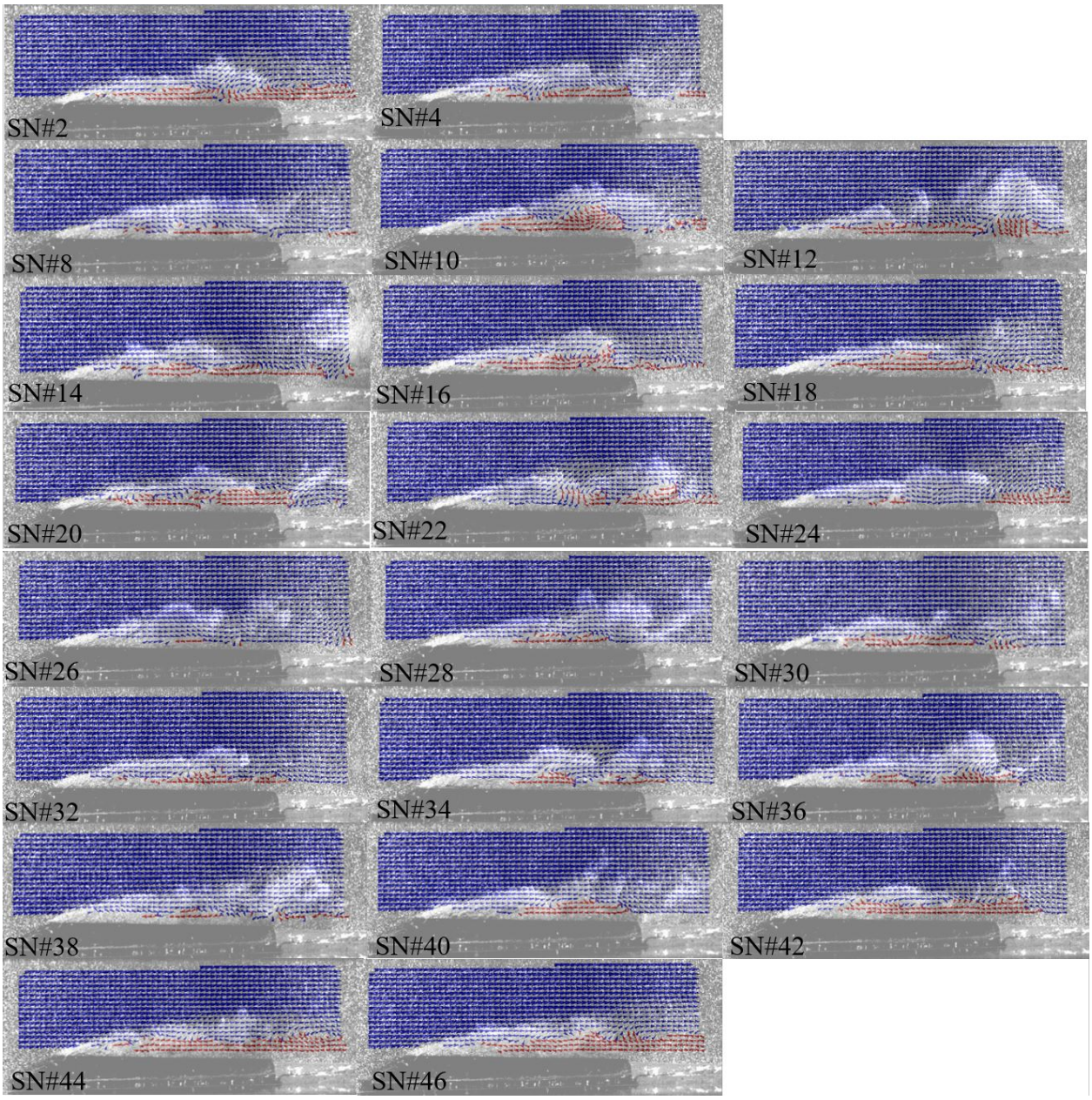

Figure 6.17: The figure illustrates the visualization of the velocity vector field overlapped with the raw images from high-speed photography. The blue (red) vector field depicts the stream-wise velocity (re-entrant jet). (a) Representation of the premature condensation of the cloud at the leading edge of the attached sheet cavity (frames 2-4). (b) Representation of the large-scale cloud cavitation convection and the consequent condensation due to the pressure recovery at the outlet (frames 8-18). (c) Representation of a series of intermittent small-scale clouds shedding (frames 20-46).

6.5 Technique # 3: Applications of CROM to the Flow Past the Throat of the Venturi Test Section

6.5.1 Application of CROM technique

Cavitating flow as it occurs past the throat of the Venturi-type section yields several modes, flow patterns, with intermittent switching between the modes. The attached sheet cavity growth and the cloud shedding are inherently aperiodic, resulting in a flow field composed of multiple modes—cavitating flow composed of distinct dominant flow patterns known as the centroids of the CROM technique. The CROM technique can investigate intermittent transitions between the flow patterns. CROM technique statistically extracts the preceding flow patterns giving rise to the current flow pattern, so one may use it to study the mechanism causing the transition from one flow regime to the other. The results obtained from CROM are employed to extract the mechanisms resulting in flow pattern transition. CROM is an approximation of the Perron-Frobenius Operator (PFO). PFO is a linear and infinite-dimension operator in terms of probability density functions (PDFs), and in practice, CROM yields a finite-dimensional approximation of PFO. CROM splits the data set in the phase space into dissimilar, non-overlapping clusters, each of which is represented via a centroid. Each of the centroids represents the mode shape of the corresponding cluster. Data points in the phase space close to a centroid are labeled with the name of the corresponding centroid. Therefore, the centroid mode shape represents the flow pattern of the data points inside of its cluster. In other words, the data points inside a cluster yield a similar flow pattern which is represented via the corresponding centroid. CROM technique primary outcomes are as follows: (1) clustering of the phase space to create some centroids, mode shapes (2) discovering the mechanism that explains the transition of the current status of the flow field

to the future status. Since the data points inside a cluster are similar and dissimilar to the data points outside the cluster, the intermittent transition from one flow pattern to the other flow pattern can be extracted.

6.5.2 Analysis and discussion of CROM results

In this section, the results of the CROM strategy applied to the velocity vector field obtained from PIV measurements of the cavitating flow are investigated. CROM algorithm initially is applied to the instantaneous velocity obtained from the PIV measurements. The cluster analysis splits the data in the phase space into 20 clusters. The dissimilarity between the clusters is maximum, and the similarity between the points inside each cluster is maximum. In case that the behavior of the flow is periodic, the discretization process of the phase-space yields the same result as the phase-averaging process. However, for cases where the non-linearity in the dynamical system hinders a well-developed periodic behavior, the clustering process may extract the dominant convective mechanisms and the transitions between these mechanisms.

The geometry of the clusters may also be studied by plotting a Voronoi diagram. Here the geometry of the clusters can be accurately defined in 4 dimensions. Since the POD time coefficients attractors can accommodate in four dimensions, the two-dimensional Voronoi diagram can only depict a drastic approximation of the cluster geometric shape. As shown in figure 6.18 the points in the 2D phase space are located inside of an incorrect region, implying that the cluster can only be accommodated in the higher dimensions.

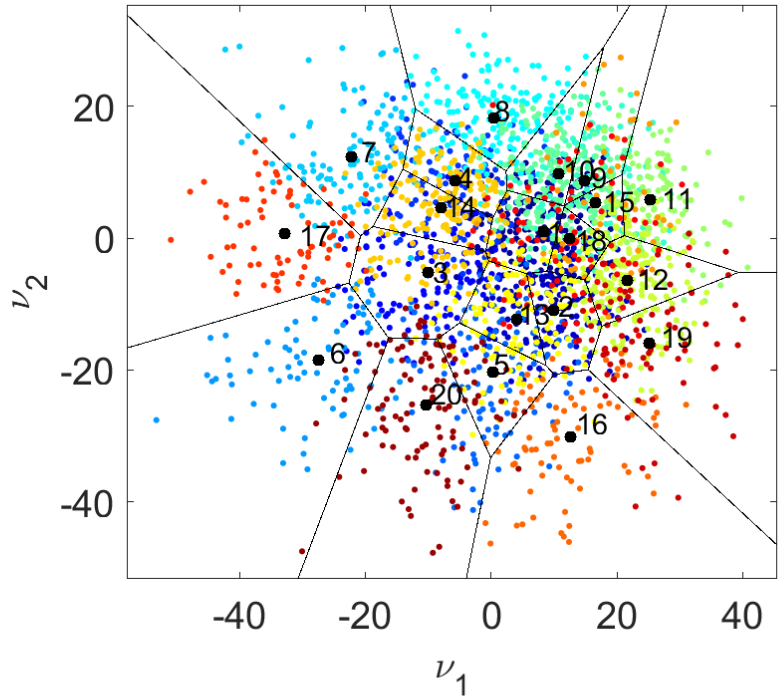

Figure 6.18: The figure shows the Voronoi diagram of the clusters, the cluster centroids (solid black bullets labeled with numbers), the data points (solid color dots) projected in the two-dimensional space of the first two POD time dynamics ν_1 and ν_2. Clusters are discriminated through different colors assigned to the dots. Dots trespassing the borders of the corresponding cluster indicate that the attractor lives in higher dimensions.

Snapshots taken from the flow display fluctuation of the attached sheet cavity length giving rise to successive irregular small cloud shedding. Patterns and geometry of the sequential cloud shedding seem to change from cycle to cycle, implying that the growth of the attached sheet cavity and consequently the shedding process is aperiodic. In this regard, CROM cluster shape modes are examined closely to study the effect of the aperiodic cloud shedding on the coherent spatial structures. The associated transition probability matrix is shown in figure 6.19. $p_{\tilde{j}k'}$ provides the probability to move from a particular state located in cluster $\tilde{j}$

to another state inside of cluster k'. The red color and bigger geometric structures mean that the probability for a particular transition is high. The cluster shape mode vectors determine the mean status of all snapshots in a particular cluster. In this study, the snapshots are grouped into 20 clusters, thereby creating 20 CROM mode shapes, figure 6.20. The first four clusters, $k' = 1 - 4$ seem to be associated with sequential convective behavior through which two coherent structures with negative velocity values are transported upstream of the flow field. On the other hand, mode shapes for clusters $k' = 5 - 9$, and $k' = 11 - 20$ display a sequential convection of three coherent structures. These two clusters exhibit a similar pattern; however, the contours of the positive and negative values of the transverse velocity correspond to each set of clusters are significantly different. Next, a Markov graph can be extracted from the transition probability matrix depicting the transitions between preceding different flow states. Since the matrix presented is not sparse, the full rank Markov graph and the associated transition are complex, thereby yielding numerous connections, making the model's study difficult. For this reason, some of the connections with very low probability values are ignored, which does not improve the understanding of the dominant transition mechanisms shown on the graph. It should be noted that the arrows represent the direction of the transition from one state to another. Based on the Markov graph, figure 6.21, an inner-group cycle exists for both triple structure shedding and pair shedding processes. Furthermore, since a direct switch between these groups exists, an irregular alternation of states is conceived due to intermittency in the dynamical system. Cluster $k' = 10$ mode shape displays a vortex merging process, thereby making it distinctive. This cluster acts as an intermediate state between the other three groups. This analysis demonstrates that all states in the dynamical system may be accessed via another state that implies some level of inherent chaotic behavior. In other words, the future status of the system is likely very sensitive to the current status, and very negligible changes in the current status may result in a radically different dynamical behavior in the next time steps.

Likewise, the distance matrix analysis yields an understating of the similarity inside a set of clusters and dissimilarity outside of them. The cluster group, $k' = 1 - 4$, associated with the *Pair* structures distance to the *triple* structures convection, let say $k' = 6 - 9, 13 - 18$, is comparably high. In contrast, the double structure inner-cluster distance between the mode shape vectors is minimum. Moreover, The inner-cluster distance between the mode shape vectors of the $W - Triple$ structures is significantly higher than the corresponding distances inside of groups *Triple* and *Pair*.

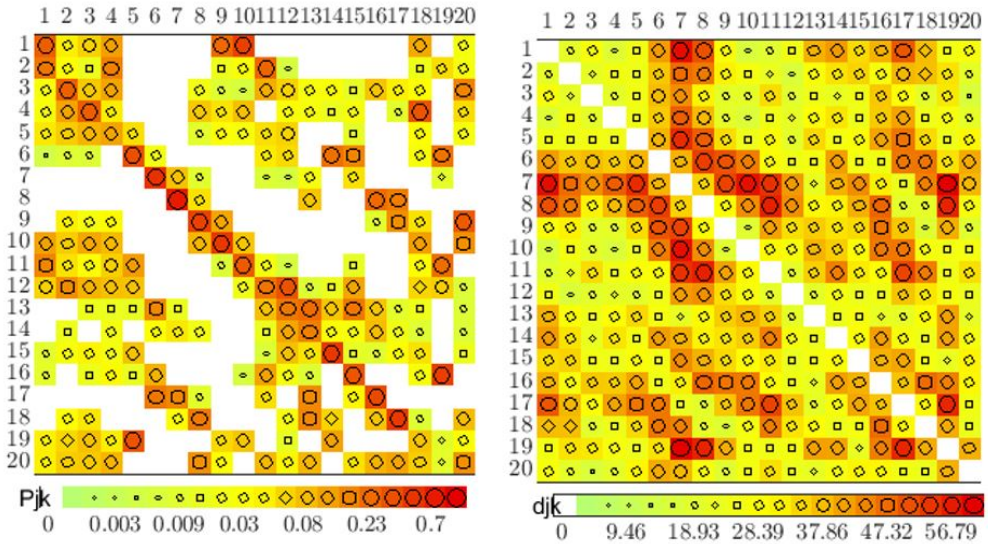

Figure 6.19: (a) CTM and (b) cluster centroid distance matrix. Simplification of the connectivity between the cluster centroids yields Three cluster dominant groups, figure 6.21, $k' = 1, 2, 3, 4$, $k' = 5, 6, 7, 8, 9$, and $k' = 11, 12, 13, 14, 15, 16, 17, 18, 19, 20$. One transition cluster $k' = 10$ that is associated with the vortex pairing is observed in the matrices.

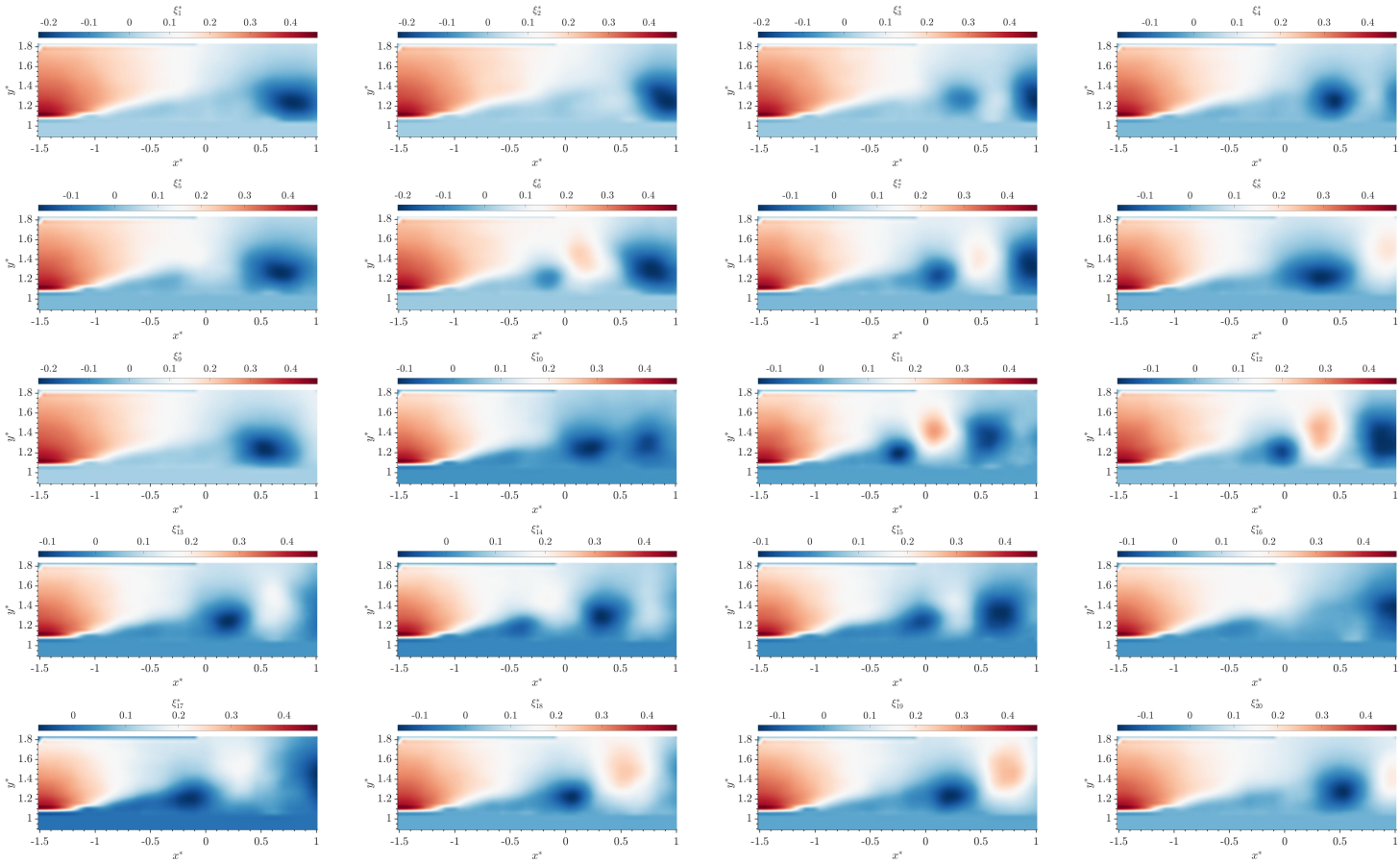

Figure 6.20: CROM mode shapes, corresponding the cluster centroid $\kappa = \{c_1, c_2, ..., c_{k_{tot}}\}$. The colors show the contours of positive (red) and negative (blue) velocity for each cluster centroid. The flow is coming from left to right.

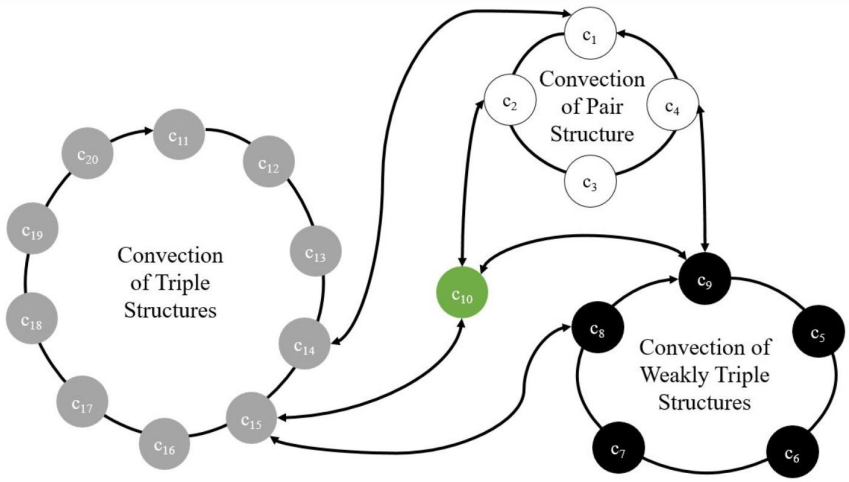

Figure 6.21: CTM schematic diagram of the velocity field associated with the liquid phase. The arrows indicate the direction of the possible transitions. A threshold is chosen to simplify the connectivity diagram. The diagram depicts three cyclic cluster groups associated with the convection of coherent triplet structures (gray and black clusters) and pair structures (white clusters). The green cluster represents an intermittent phenomenon that occurs as a consequence of the bifurcation point.

The evolution of the probability distribution can be determined by studying the map of eigenvalues of the CTM, figure 6.22. Eigenvalues are located inside of a unit circle, implying that all eigenvectors decay asymptotically. The largest eigenvalue $\tilde{l}_{CTM,1} = 1$ and the corresponding eigenvector $\omega_{CTM,1}$ is associated with the stationary probability distribution. The dominant eigenvalue and the converged probability distribution are equal to each other, figure 6.22. The long-term evolution of P_∞ converges to a unique matrix, so the system is *ergodic*. Despite, the system is highly sensitive to the initial point in the state space, as shown previously, the ensemble mean converges to the time mean, implying the dynamical system is statistically reproducible. The preceding observation also demonstrates that the geometry of the state-space is reproducible.

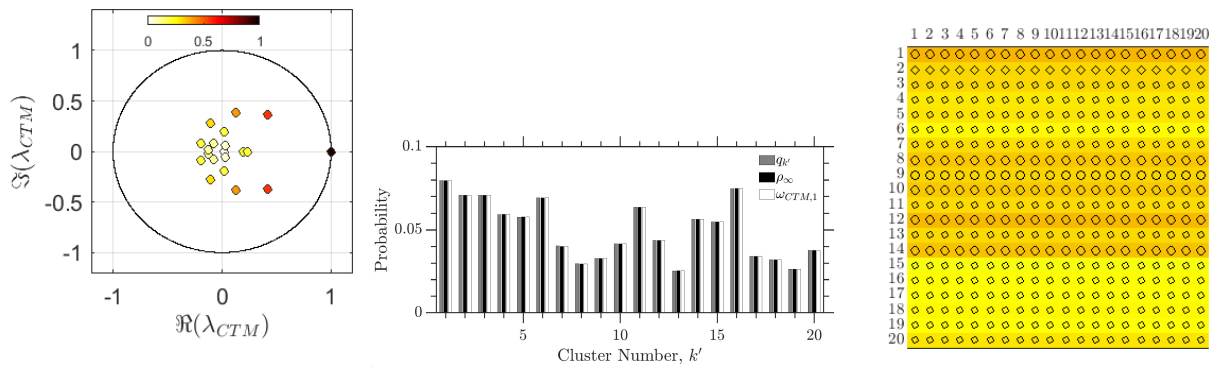

Figure 6.22: Stability analysis of the CTM: (a) complex eigenvalues of CTM with the largest eigenvalue equals to +1. The color bar displays the absolute value of the eigenvalue (b) $q_{k'}$ the initial probability distribution of the data, ρ_∞ corresponds to the asymptotic PDF, the eigenvector $\omega_{CTM,1}$ associated with the dominant eigenvalue (c) converged CTM. All eigenvalues are located inside of the unit circle implying that the dynamical system is *ergodic*.

6.6 Conclusions on the Modal Analysis of the Cavitating Flow

The chapter presents the instabilities mechanism in the cavitating flow as it occurs on a Venturi-type test, the section using planar velocity vector field. Three data-driven techniques are applied to the fluctuating component of the velocity, and the following results have been obtained:

- Modal decomposition through DMD yields modes of instabilities: (1) corresponding to the velocity difference across the liquid-vapor interface (2) related to the vapor cloud shedding. Since the frequency contents of different vapor cloud instability modes are incommensurate, quasi-periodic behavior of the vapor cloud shedding was demonstrated. Kelvin-Helmholtz instabilities are shown to acquire a higher decay rate, lower frequency ratio, and lower initial energy than vapor cloud instabilities.

- The low pass and bandpass filters applied on the fluctuating component of the velocity vector field separated the length scales in the flow field. The length scales' time dynamics reveal three distinct instabilities: slow-varying drift flow, instability due to the vapor-liquid velocity shear, and the vapor cloud shedding. The path of the TKE energy is tracked; accordingly, the energy loss by the mean flow is transferred to the slow-varying drift flow which distributes this energy to the smaller length scales including the velocity shear instability and the shedding of the vapor cloud. Study of the LLEs of POD energetic modes, modes 1-3, time dynamics demonstrates that the largest length scales are globally stable. Although, the time dynamics in a short period of time shows some level of chaos, the system asymptotical becomes periodic. Finally, combination of the energetic POD modes is utilized to reconstruct the instantaneous status of the flow field. In this regard, the premature condensation occurred on the trailing edge of the attached sheet cavity and the vapor cloud shedding is accurately predicted using the combination of the POD modes.

- The instabilities in the form of coherent structures that are the byproduct of the vapor cloud shedding are studied using the CROM technique. Results obtained from CROM technique revealed the dominant patterns in the flow field by means of phase-averaging. Four dominant flow regimes are identified; modes of instabilities are related to the convection of the coherent structure in the wake of the attached sheet cavity. Fundamental changes (bifurcation) in the flow regime are assigned to the occurrence of particular clusters that were tagged and studied separately. Path and probability of transition between different dominant flow regimes are shown. It has been observed that 68% of the time, triple structures are formed and transported toward the outlet. On the other hand, 28% of the time, a pair of coherent structures is formed and convected downstream. A bifurcation cluster has been identified that acts as an intermediate

between the dominant flow regimes mentioned above.

Chapter 7

Dominant Physical Mechanisms

7.1 Introduction

The chapter investigates the turbulent energy cascade as it occurs in the attached sheet cavity and the free stream. A term-by-term inspection of the equation governing the averaged kinetic energy in the turbulent fluctuations is presented to track the mean flow kinetic energy path. In this regard, the underlying physical mechanisms impacting the local rate of change of turbulence kinetic energy following the mean flow in the compressible flow are enumerated, and the dominant mechanisms are distilled. Besides, the effect of the liquid-vapor phase change on values of shear production, transport of the TKE, pressure work, and pressure-dilatation is investigated and further compared against the free-stream flow. It is shown that the production of Turbulence Kinetic Energy (TKE) resulting from high shear stress in the sheet cavity imparted more instability to the flow than other physical mechanisms. The pressure fluctuation is comparable to the velocity fluctuations and contributes to the reduced transport of turbulence kinetic energy at the liquid-vapor interface. Finally, to shed light on the role of pressure work and pressure-dilatation terms in the turbulent energy cascade, the reversion of the sign in values of these terms is highlighted. It is demonstrated that the pressure-dilatation and pressure work is more effective than the dissipation term and contribute to the dissipation in the attached sheet cavity.

The following section presents mechanisms causing time-averaged momentum variation in the sheet cavity and the perturbed free stream. The mechanisms diminishing or increasing the momentum in different regions of the flow field are enumerated. The role of the isotropic and anisotropic stresses in the destabilization of the attached sheet cavity is demonstrated. Besides, the stresses applied on the fluid elements in cavitation inception and transport are highlighted.

Next, dominant, underlying mechanisms causing the local momentum variation in different regions of the flow field are presented. In complex fluid flows, the local behavior of the flow can be described accurately by the balance between a few dominant physical processes in the governing equations [38]. In the present chapter, identifying the dominant balance relations in the cavitating flow has been implemented using Gaussian Mixture Models (GMMs). Then the maximum variance for each cluster has been approximated using Sparse Principal Component Analysis (SPCA). Points in the equation space are obtained from the X-ray data acquisition, accompanied by numerical simulations of the instantaneous pressure field. The pressure distribution in a Venturi-type test section is estimated using the Ultra-fast Time-resolved Particle Image Velocimetry (TR-PIV) and local void fraction obtained from X-ray imaging. Poisson's equation obtained from the conservative form of compressible momentum equation is solved to result in the instantaneous snapshots of the pressure field. The dominant balance model suggests that the turbulence anisotropy is significant in the regions where the local void fraction level is high, i.e., attached sheet cavity and near wake where cavitation break-up occurs. The level of turbulence anisotropy rapidly decreases in the free stream and the boundary layer, proving that the isotropic turbulence delineates the flow field's dynamics in the free-stream and boundary layer. The pressure fluctuation is comparable to the velocity fluctuations and contributes to the reduced transport of turbulence kinetic energy at the liquid-vapor interface.

In the last section, the dominant forces instantaneously applied to each element of fluids are investigated. It is shown that the flow field can safely be assumed inviscid. Acceleration terms in each flow field region are shown to be in balance with the isotropic pressure forces. Additionally, it has been demonstrated that the pressure gradient forces introduce instability to the flow field where the attached sheet cavity is formed. The degree of the correlation between the terms in the dominant balance model is depicted that further demonstrates the role of the pressure gradient forces in the causation of the attached sheet cavity instability and the advective acceleration in the free stream.

7.2 Exact Compressible Turbulence Kinetic Energy Equation

In this section, the mechanism of the kinetic energy dissipation is inspected using equations that govern the mean flow kinetic energy and the average kinetic energy of the fluctuations. The exact equation governing the mean Turbulence Kinetic Energy (TKE) is extracted by multiplying the instantaneous momentum equation by the Favre fluctuating velocity component and then time averaging:

$$\frac{\partial}{\partial t}(\overline{\rho}k)+\frac{\partial}{\partial x_j}(\overline{\rho}\tilde{u}_j k) = \overline{\rho}\tilde{\tau}_{ij}\frac{\partial \tilde{u}_i}{\partial x_j}-\overline{\tau_{ji}\frac{\partial u_i''}{\partial x_j}}+\frac{\partial}{\partial x_j}(\overline{\tau_{ji}u_i''}-\overline{\rho u_j''\frac{1}{2}u_i''u_i''}-\overline{p'u_j''})-\overline{u_i''}\frac{\partial P}{\partial x_i}+\overline{p'\frac{\partial u_i''}{\partial x_i}} \quad (7.1)$$

where TKE is defined as follows:

$$k = \frac{1}{2}(\overline{u''^2} + \overline{v''^2}) \tag{7.2}$$

Eq. 7.1 is the energy balance or energy-budget equation for TKE. The left-hand side of the equation expresses the unsteady time-averaged density-weighted TKE and convection of the TKE. The right-hand side terms represent the mechanisms that enforce changes to the TKE in the differential level. ETKE equation terms are defined as follows:

- $\frac{\partial}{\partial t}(\overline{\rho}k)$ is the rate of change of turbulence kinetic energy due to non-stationary signal of the mean flow.

- $\frac{\partial}{\partial x_j}(\overline{\rho}\tilde{u}_j k)$ is the rate of change of turbulence kinetic energy due to the advection by the mean flow.

- $\frac{\partial}{\partial x_j}(\overline{\tau_{ji}u_i''} - \overline{\rho u_j'' \frac{1}{2} u_i'' u_i''} - \overline{p' u_j''})$ is the diffusion of kinetic energy due to the molecular processes, the turbulent fluctuations, and pressure fluctuations, respectively.

- $\overline{\rho}\tilde{\tau}_{ij}\frac{\partial \tilde{u}_i}{\partial x_j}$ is the rate of production of TKE extracted from the mean flow.

- $\overline{\tau_{ji}\frac{\partial u_i''}{\partial x_j}}$ is the rate of dissipation of TKE due to the molecular processes.

- $\overline{u_i''}\frac{\partial P}{\partial x_i}$ is the pressure work term. If the velocity and pressure are in the same direction work term is positive.

- $\overline{p'\frac{\partial u_i''}{\partial x_i}}$ is pressure dilitation. This term defines expansion or contraction of the fluid element in all direction at the same time.

Diffusion due to the pressure fluctuations represents the spatial transport of TKE by pressure fluctuations. Instantaneous viscous stresses also play a role in the spatial transport of the TKE; this term was introduced previously as the molecular diffusion of TKE. At the scale

of an infinitesimal volume of the fluid, pressure and viscous diffusion terms introduces an acceleration to the adjacent elements and results in the transportation of the TKE. The other mechanism that gives rise to the spatial transport of TKE is turbulent stresses. The TKE can be directly transported to other regions through turbulent fluctuations. The turbulence diffusion terms in a fluid volume in space transport the energy from regions with high TKE regions with low TKE. In an Eulerian perspective, the transport terms are only responsible for distributing the energy in the domain of the dynamical system. Statistically, the above-mentioned diffusive-type mechanism will only be applied to smear out the energy from regions of higher kinetic energy to lower. These terms neither produce nor dissipate the TKE energy in the lifetime of the dynamical system. Therefore, the accumulation of the TKE in some regions of the flow is smoothed out via diffusion terms.

The third term in Eq. (7.1) is the shear-production term representing the rate of transfer of the kinetic energy from mean flow to turbulent fluctuations. The non-zero shear production inside the sheet cavity demonstrates that the mean flow shear is non-zero, and the turbulence must be significantly anisotropic. The preceding fact also indicates that the level of the anisotropic turbulence in the sheet cavity is higher than the free-stream; therefore, the energy input rate inside of the sheet cavity is higher. In some sense, the mean shear deforms the large-scale eddies in the regions with high void fractions and feeds them with significant energy. The shear stress gives rise to the production of the TKE. Then the kinetic energy is transferred down to the smaller eddies through the turbulent energy cascade and finally is dissipated by viscous forces as heat at the small scales, Kolmogorov scales. As mentioned above, the fourth term in Eq. (7.1) is the viscous dissipation of TKE. The sign of the shear production and the viscous dissipation is different, and their magnitudes for most of the regions are typically similar, thereby balancing each other in the Eq. (7.1). Production term is the only means by which energy is exchanged between the mean flow and fluctuations.

The TKE production term and the pressure correlation term transfer energy from the mean flow to the TKE. Since the dissipation value is negative through the entire field, the energy is irrecoverable, and TKE loss eventually occurs due to the transfer of this energy into internal energy. However, the dilatation term may result in a reversible exchange between interior and kinetic energies. In this regard, pressure-dilatation and pressure work affect the cascade process by reversing the kinetic and internal energies at distinct scales. On the other hand, the viscous effect results in the dissipation of the kinetic energy as heat. Figure 7.1 shows the computed terms of exact compressible turbulence kinetic energy equation in the cavitating flow as it occurs in the Venturi-type profile.

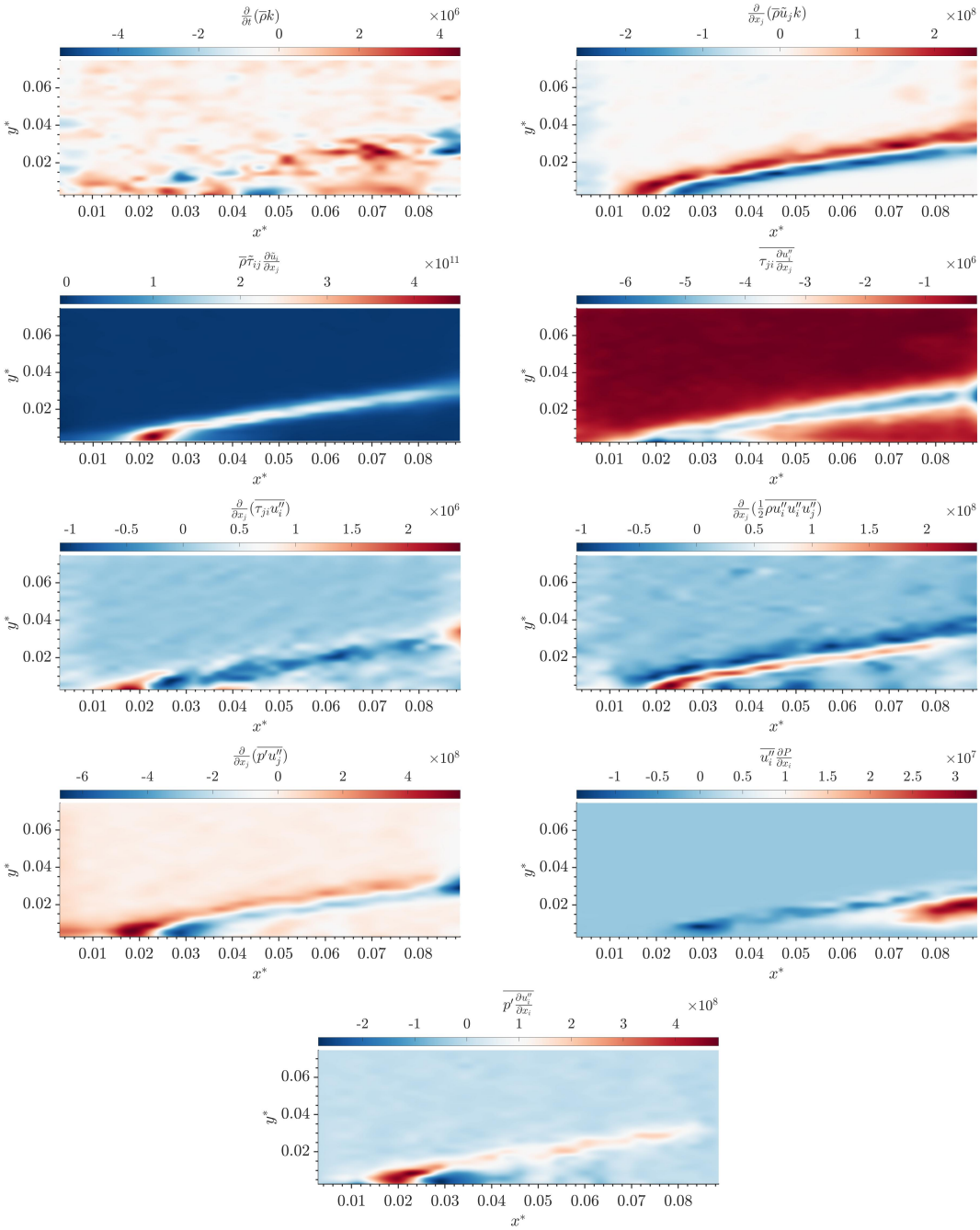

Figure 7.1: Representation of the exact turbulence kinetic energy equation for the cavitating flow (a) rate of change of TKE due to the instability in the mean flow (b) rate of change of TKE due to the advection of the mean flow(c) Rate of production of TKE extracted from the non-stationary signal of the mean flow (d) fluctuating viscous stresses work against the fluctuating strain rates or deformation of the fluid material or velocity deformation rate. (e) Transport of TKE due to the viscous stresses (f) Transport of the TKE due to the velocity fluctuations. (g) mechanism of transportation of the TKE due to the pressure fluctuations.

7.3 Favre-averaged Momentum Equation in a Cavitating Flow

High-resolution data obtained from simultaneous measurements of the planar velocity vector field and the void fraction and the numerical results of the pressure field are utilized to compute the terms in Favre-averaged momentum equation, figure 7.2. It is observed that, in the cavity sheet, the momentum goes through a drastic reduction as a result of the advection of the mean flow changes. Besides, the dominant mechanism of the momentum variation is advection which is two orders of magnitude higher than the instability mechanisms. In the vicinity of the throat, the instability increases the momentum, while this mechanism tends to reduce the momentum away from the throat. Since the mean pressure gradient is very strong inside the sheet cavity, it causes the most dominant stress applied to this region's fluid element. The strong gradients give rise to the coherent vortical structures that are advected downstream with the mean flow. It is also shown that the pressure gradient is negative, implying that tensile stress is applied to the fluid element inside the sheet cavity; therefore, the element goes through an expansion, which is the main factor leading to the vapor structure deformation. As expected compared to the viscous stresses, the Reynolds stresses apply a greater load on the fluid elements. It is also displayed that away from the sheet cavity where the gradients of the field are relatively small, viscous stresses and Reynolds stresses do not contribute significantly to the dynamics. It can safely express that outside of the cavitating flow, an inviscid balance between acceleration term, advection terms, and external stresses exist. Besides, the viscous terms impact on the dynamics of the flow field is negligible. Thus, the coherent structures formed in the flow field will be transported downstream with an insignificant energy loss. Both Reynolds stress anisotropy, isotropic part of Reynolds stress, and viscous stresses apply a tensile load on the liquid-vapor

interface that contributes to the inception of the cavitation. On the other hand, these terms apply a compression load on the elements inside of the sheet cavity. The strong tensile stresses applied to the elements adjacent to the cavitation flow causes a major reduction in the momentum. It should be noted that Reynolds stresses are one order of magnitude less than the mean pressure gradients isotropic stress.

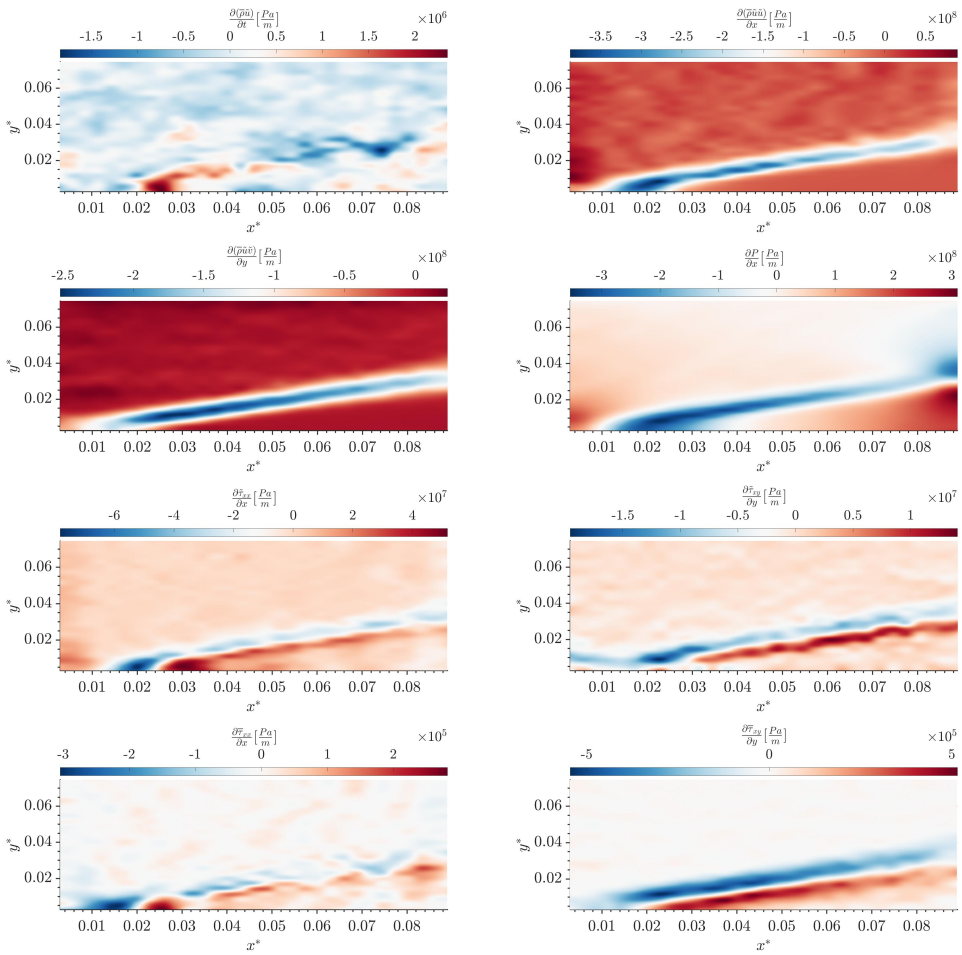

Figure 7.2: Representation of the Favre-averaged momentum equation where the sheet cavity is formed. (a) rate of change of momentum of the fluid element as a result of the mean flow instability. (b-c) rate of change in momentum of the fluid element owing to the advection as it occurs in the mean flow. (d) the isotropic stress applied as a result of the mean pressure field gradient. (e-f) Reynolds stresses as a result of the fluctuations in the velocity vector field. (g-h) Viscous stresses are applied to the fluid element due to the molecular processes.

7.4 Favre-averaged Momentum Transport Dominant Mechanisms in Transition to Cavitating Flow

In this section, the dominant balance forces of an internal flow going through a transition to cavitating flow have been investigated. For this purpose, the data obtained from X-ray imaging has been utilized. Figure 7.5 depicts the equation space clusters and associated dominant balance models for the Favre-averaged momentum equation. The method identifies regions corresponding to high void fraction, wall-bounded layer, free stream, vapor-liquid interface. In practice, the spatial domain of the cavitating flow may be broken down into distinct regions where only some of the terms are dominantly contributing to the momentum balance equations. For instance, anisotropic turbulence is not observed in the free stream; conversely, pressure gradient and TKE spatial changes apply significant forces to the fluid element. At the high void fraction region, rotation or buoyancy effects play an essential role in giving rise to strong anisotropic turbulence. Since turbulence is isentropic in the red, green, and blue regions, Reynolds stress tensor in the governing equations of Reynolds stress transport may be replaced by TKE. Besides, some regions of the flow field depict independence to the unsteadiness. For instance, part of the liquid-vapor interface, the flow adjacent to the wall at the throat, and the free stream flow are in a steady state. In the purple region located inside the high void fraction region, mean pressure gradients and Reynolds stresses apply a compressive load on the fluid element that leads to the recovery of the momentum. On the other hand, in the red region representing the liquid-vapor interface, since isotropic and anisotropic part of the stresses due to the velocity fluctuations and the mean pressure gradients apply a tensile load on the elements, momentum reduction occurs.

Another method to interpret the GMM is by extracting the covariance matrices, look at figure 7.3. The color bar indicates which terms are not contributing to the dominant bal-

ance made in each cluster. Since the number of clusters is set to 6, the redundant clusters are not observed. The regularization value is set to 10^7. The norm of the discarded terms in the cluster region determines the residuals of the inactive terms. Cluster # 1 depicts the region where the vapor concentration is significant. It can be observed that the flow field in this region is unsteady, and pressure gradients and Reynolds stresses apply notable accelerations leading to momentum transport in the form of advection. Cluster # 2 depicts the free stream flow where the correlation between the unsteady and other terms is negligible; therefore, flow can be safely modeled as a steady flow. It can be observed that the strong gradient of pressure primarily derives the momentum variation in the free stream. Clusters # 3 and 5 depict the liquid-vapor interface. A strong correlation exists between the pressure gradients and the instabilities mechanism. Therefore, it is observed that the compressive stress applied by the pressure gradients force is the mechanism giving rise to the instabilities on the liquid-vapor interface. Cluster # 6 falls into the region where the cavitation concentration is significant. Isotropic stresses applied by the mean pressure gradients are the primary mechanism governing the momentum flux and cause the instabilities in the flow field. The covariance matrix shows that the Reynolds stresses are correlated with the unsteady term and the advection terms. The isotropic and anisotropic parts of the stresses due to the velocity fluctuations are of secondary and tertiary importance in the transport of momentum by the mean flow field and introduce the instabilities to the flow field.

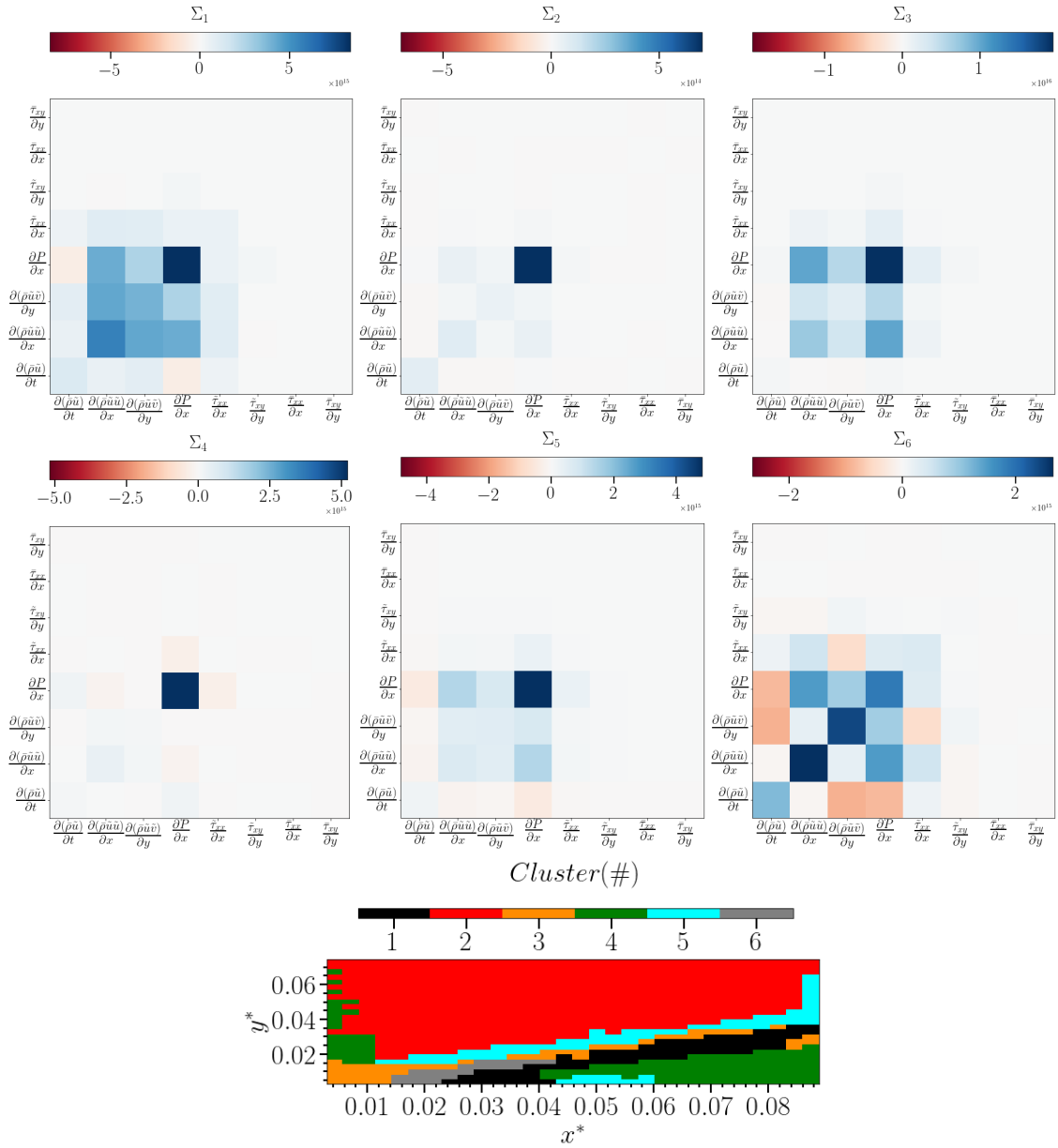

Figure 7.3: The figure presents the Identification of the dominant terms on the Favre-averaged momentum equation in x-direction represented by covariance matrices inferred by the GMM. Covariance matrices depict dominant terms in separate regions: region (1) volume fraction is significantly high, region (2) freestream, regions (3), (5) interface of the liquid and gas phases, region (4) wall-bounded cavitating flow, and region (6) where most of the terms are contributing to the balance.

To describe the correlation between the forces in the Favre-averaged momentum equation,

figure 7.4 depicts the equation space clusters of the Favre-averaged momentum equation in the cavitating flow. Sets of points have significantly reduced correlation in equation space's specific directions that show the signature of the dominant balance phenomenon in different regions of the flow field. Equation space representation identifies the local balance relations between the forces applied to an element of the fluid in the corresponding local region. For instance, the black cluster shows a strong linear correlation between pressure gradients, Reynolds stresses, momentum transport due to the instabilities, and the advection by the mean flow field. Compared to the black cluster, the points in the red and green clusters show randomly distributed points in the equation space. The weak correlation between the terms in the red and green clusters was previously shown in the graph of the covariance matrix, where the pressure gradients were the primary mechanism driving the transport of the momentum, and other mechanisms were deactivated. In the yellow cluster, the strongest correlation is observed in the plane of the pressure gradient and the advective terms, where the points can be collapsed into a linear curve. The same observations can be made for the blue cluster: the pressure gradients depict a linear correlation with the unsteady and advective terms. In practice, GMMs application to the data points creates redundant clusters that can suffer the interpretability of the provided model, figure 7.4. To solve the preceding issue, SPCA, which uses l_1 regularization, is employed. SPCA yields parsimonious dominant balance models by dismissing the insignificant terms in the equation space. Clusters that are representative of the dominant balance regime are interpretable via the direction of the maximum variance. SPCA is applied to the set of points in each GMM cluster, and the active terms in the cluster are defines as the terms that have non-zero entries in the sparse approximation to the leading principal component, figure 7.5.

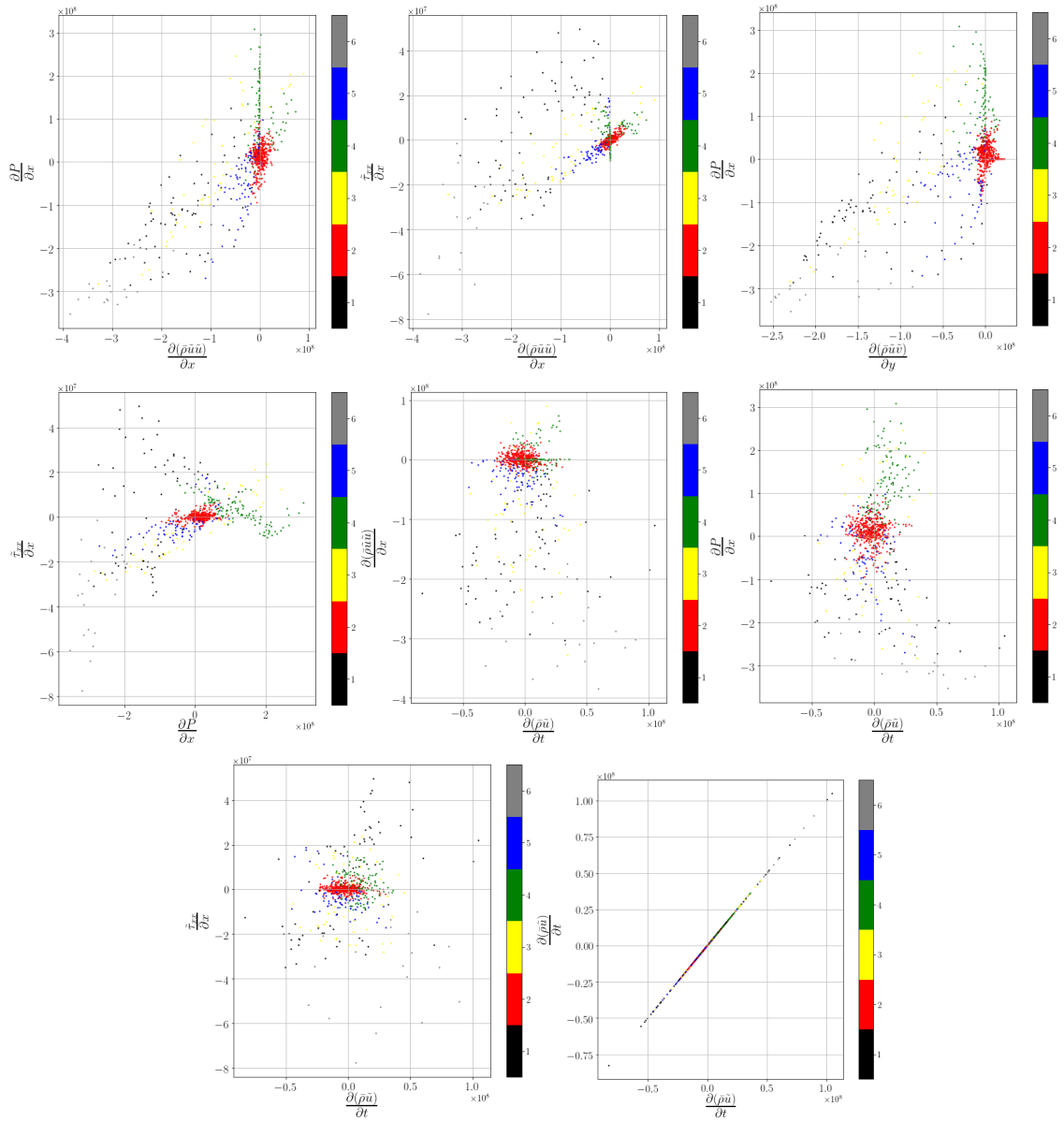

Figure 7.4: Visualization of the equation space associated with Favre-averaged momentum equation in the cavitating flow. The equation space representation enables clustering and sparse approximation of the momentum equation. Extraction of distinct geometrical structures in the space corresponding to dominant balance terms is feasible. The equation space represents the correlation of the forces in momentum equation in non-overlapping regions of the flow field. The dominant forces in each region can be extracted and the balance between different forces can be studied.

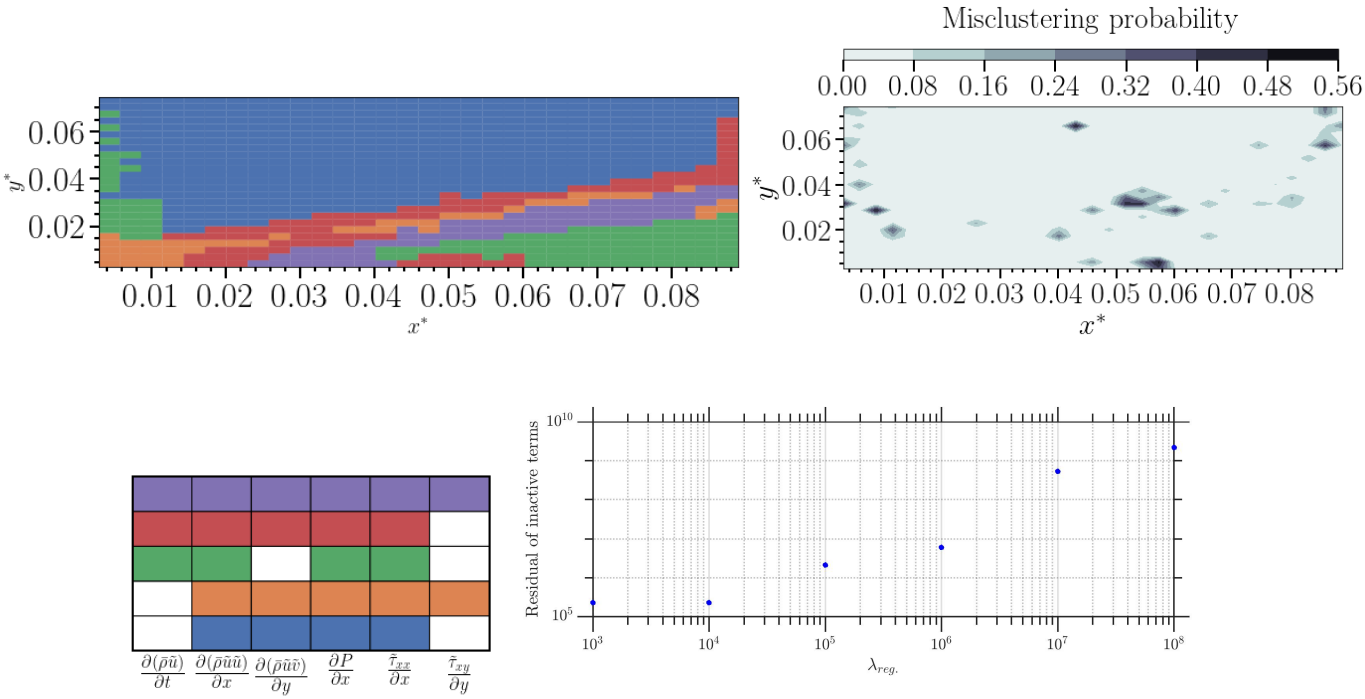

Figure 7.5: Schematic of the dominant balance identification applied to a cavitating flow for $\lambda_{reg} = 10^7$. The equation space is associated with the Favre-averaged momentum equation in the x-direction. (a) The entire domain is segmented using the balance models shown in (c). The segmentation enables the identification of distinct regimes of flow. GMM probabilistic model enables investigation of the clustering uncertainty. (b) Summation of the uncertainty associated with the models that cannot be accommodated in the balance relation. (d) Residuals of the inactive terms in the models as a Sparse Principal Component Analysis (SPCA) regularization function.

7.5 Compressible Momentum Transport Dominant Mechanisms in Transition to Cavitating Flow

Figure 7.6 displays the dominant balance model of the cavitating flow. To eliminate the redundant clusters and identify the sparse balance models in each cluster, SPCA is applied to the points in each GMM cluster. The leading principle component gives the direction of maximum variance; nonzero components in the sparse approximation correspond to active

terms in that cluster. The dominant balance model obtained in this section suggests that the free stream, the orange region, is inviscid and acceleration terms balance pressure gradient force in the form of wall-normal and stream-wise advection. Orange cluster indicates the free stream flow where unsteadiness is negligible. Adjacent to the bottom wall, the stream-wise advection terms balance with the pressure gradient, represented by the blue region. It is observed that unsteadiness is emphasized in the regions with a high void fraction represented by the green cluster. Like the time-averaged governing equation, strong isotropic stresses applied by the instantaneous pressure gradients drive the flow field's instabilities. It can be expressed that the primary mechanism causing instabilities in the velocity vector field inside of the attached sheet cavity at the wake of the throat is the presence of a strong pressure gradient. Visualizing the equation space helps to extract the underlying linear relationship between different terms in the momentum equation, look at figure 7.7. As expected, the variation in the instantaneous momentum of a fluid element due to the instabilities is correlated with the pressure gradient for the green cluster. Conversely, for the other two clusters, the points in the equation space are randomly distributed, showing no meaningful linear correlation between the pressure gradient and the time-dependent acceleration term. Since the points in the equation space corresponding to the viscous terms are distributed randomly, the viscous terms show the lowest correlation with the other terms. It can be observed that the pressure gradient shows a linear correlation with the advective acceleration for all of the clusters.

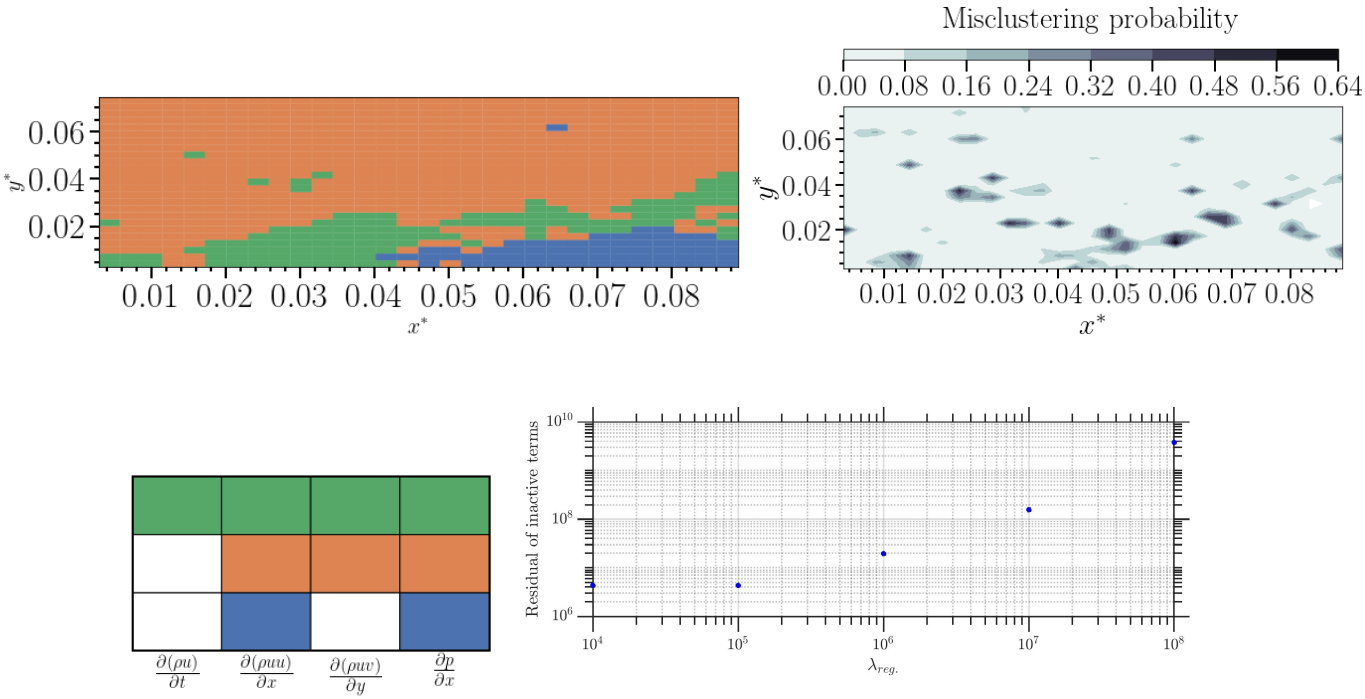

Figure 7.6: Schematic of the dominant balance identification applied to a cavitating flow for $\lambda_{reg} = 10^7$. The equation space is associated with the compressible momentum equation in the x-direction. (a) The entire domain is segmented using the balance models shown in (c). (b) Summation of the uncertainty associated with the models that cannot be accommodated in the balance relation. (d) Residuals of the inactive terms in the models as a Sparse Principal Component Analysis (SPCA) regularization function.

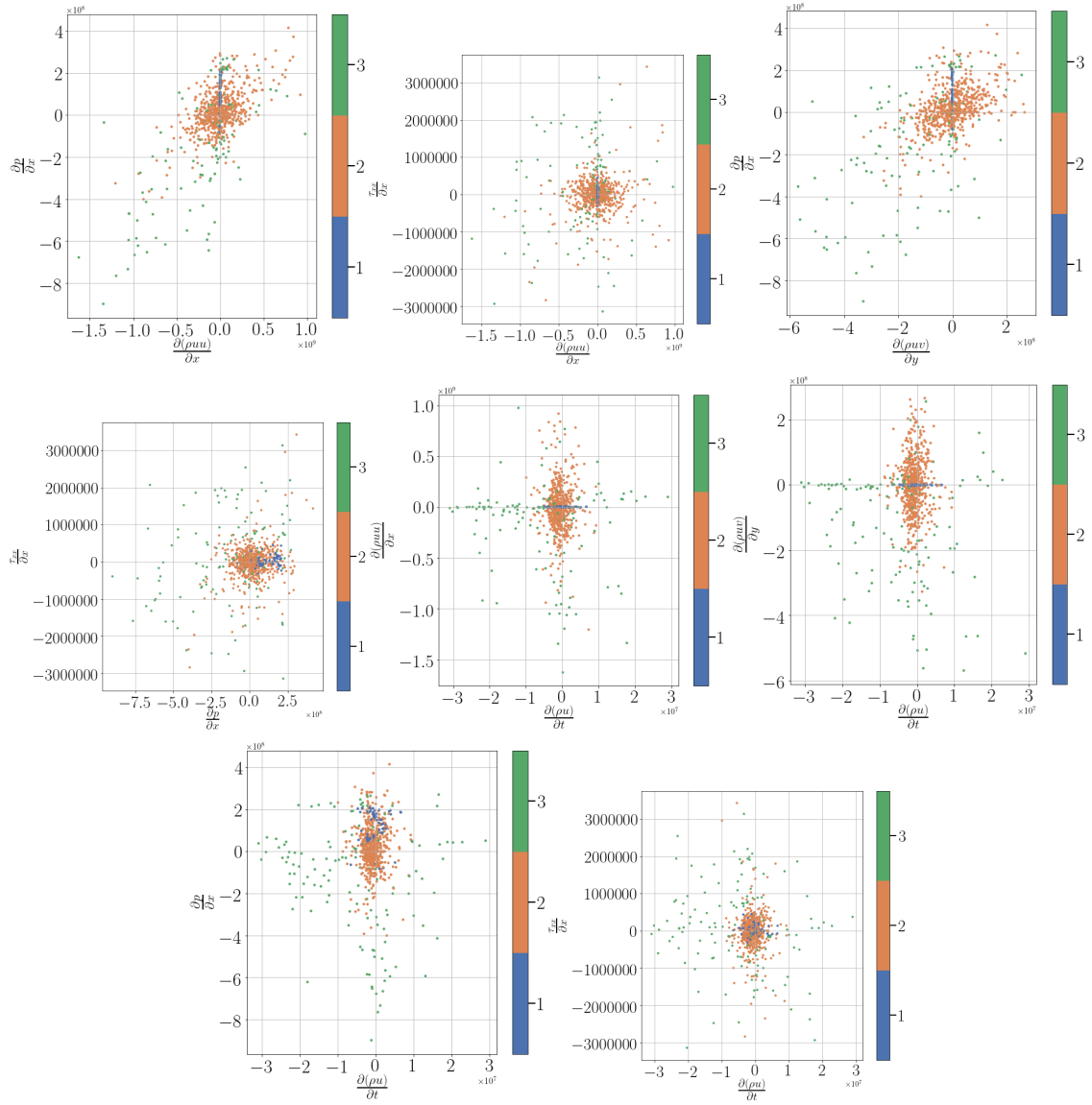

Figure 7.7: The figure presents the visualization of the equation space associated with the compressible momentum equation in the cavitating flow. SPCA is employed to the set of points in each GMM cluster and. For further information look at figure 7.4

7.6 Conclusions on Dominant Physical Mechanisms on Venturi-type Profile

This chapter investigates the physical mechanisms governing the variations in the TKE attached sheet cavity, liquid-vapor interface, and the non-cavitating free-stream flow. It is shown that the numerical method mentioned above employing the TKE budget equation implies the following outcomes:

- The highest rate of the shear stress production occurs on the liquid-vapor interface where the velocity difference between the free-stream and the attached sheet cavity is significant. Since the magnitude of the production term is high compared to the other terms, the shear stress introduces the most significant impact on the instabilities in the flow field.

- Pressure fluctuations delay the redistribution of the TKE on the interface of the two phases. On the other hand, velocity fluctuations contribute to the transport of the TKE from regions with high levels to low-level regions.

- Dissipation term is shown to have the most negligible impact among other mechanisms. Therefore, the loss of kinetic energy due to the exchange of the TKE into internal energy does not play an essential role in the variation of the TKE.

Additionally, the dominant time-averaged stresses enforcing the spatial and temporal variation of the momentum past the throat of the Venturi section are scrutinized. According to the numerical results obtained from the Favre-averaged momentum equation, the following findings are extracted:

- Strong pressure gradients give rise to instability in the flow field, increasing the mo-

mentum adjacent to the throat, while this instability diminished the momentum in the near wake of the throat.

- The pressure gradients apply tensile stress on the fluid elements located inside the attached sheet cavity that causes the transport of the void fraction and growth of the vapor structures.

- Since the viscous stresses in the flow field is three orders of magnitude lower than the Reynolds stresses and pressure gradients forces, the energy loss resulting from the deformation of the eddies in the flow field can be neglected.

- Anisotropy and isotropic part of Reynolds stress enforce a tensile load added up to the isotropic pressure gradients. Therefore, Reynolds stresses influence the transport of void fraction, and they can improve the production of the vapor phase at the liquid-vapor interface.

In the following two sections, the dominant forces in different regions of the flow field and their effect on the momentum transport resulting from the advection and instabilities are extracted utilizing GMMs. GMMs numerical results can be summarized as follows:

- The primary mechanism of the instabilities in the sheet cavity is the intense anisotropic stress that is caused as a result of the buoyancy force.

- In the cavitating flow, a strong correlation between the pressure gradients and the instabilities mechanism is observed. Isotropic and anisotropic stresses applied on the fluid element due to the mean pressure gradients and the temporal fluctuations of velocity cause strong instabilities inside the sheet cavity and at the liquid-vapor interface.

- In the non-cavitating flow, the momentum flux occurs as a result of the advection.

Since the isotropic terms, including the isotropic Reynolds stress and the mean pressure gradients, are dominant in the non-cavitating flow, the anisotropic turbulence can be safely neglected. Besides, the flow field in this region is independent of temporal variations implying a steady state.

- The results obtained from the balance of the forces in the momentum transport equation confirm the time-averaged momentum transport equation. Accordingly, the instantaneous pressure gradients forces inside the sheet cavity are correlated with the mechanism of the instabilities.

Chapter 8

Data-driven Discovery of Phase Transition Field Equation

8.1 Introduction

In the study of the inception of the cavitation, it is imperative to consider the liquid composition. Depending on the impurity of the liquid phase, different scenarios might occur as the flow field variables change. For instance, in case of a rapid drop of the pressure, liquid may cross the thermodynamic saturation without necessarily going through the phase transition process. The pressure recovery in the far-field may not result in the phase change of the vapor phase. In the conditions mentioned above, the flow field is called to be in metastable equilibrium. In this flow condition small disturbances in the flow field or adding impurity to the liquid result in a phase transition. The inception of the cavitation occurs where the tensile strength of the liquid is small [14]. The cavitation inception can be grouped into two forms: homogeneous and heterogeneous inception. The thermal activities govern homogeneous cavitation inception within the flow field, resulting in small-scale voids in the medium. On the other hand, large-scale cavitation formation is governed by surface tension. High surface tension prevents the growth of the small scales voids in the pure liquid. In contrast, the heterogeneous cavitation inception occurs in an impure liquid medium where

the local surface tension is significantly small. Since the water is composed of impurity in the current experiments, the tensile strength of the liquid phase is small locally. Therefore, given that the pressure field crosses the thermodynamic saturation curve the large-scale cavitation occurs. In other words, in practice, the inception of the cavitation is governed by the thermodynamic saturation curves, and the metastable equilibrium does not happen in this flow condition. Impurity in the tap water results in heterogeneous cavitation inception, and accumulation of nuclei leads to large-scale vapor structures. In the current chapter, it is assumed the cavitation inception occurs when the pressure field crosses the saturation pressure, and the metastable state does not happen. To further improve the understanding of the cavitation inception, one may need to know the composition of the water. The preceding description implies that the thermodynamic saturation curves are valid for a particular composition of water that needs to be determined in advance. In the current research, it is assumed that the cavitating flow is composed of a mixture of the vapor and liquid that behaves as a single species; for instance, the relative motion between the phases is negligible, so the phases move simultaneously with the same velocity. Besides, it is assumed that the two phases are in mechanical equilibrium: the local pressure field for both species is the same. It is also assumed that the flow goes through an isothermal process, and the density of the vapor phase dependence on the pressure field is insignificant.

Furthermore, cavitation bubbles transporting past the throat of the Venturi depend on the pressure gradient. Figure 3.4 depicts the scanning positions. Pressure gradient intensities in the first region depend highly on the location. Besides, the pressure gradient interaction with the vapor structures is strong in the first and second regions of the flow field. Here it is instructive to assume that the pressure is acting on the liquid phase as a tensile force. To cause a rupture in the liquid phase, a pressure field exceeding the local tensile strength is necessary. Impure water cannot tolerate tension and will cavitate in the flow field region

where tensile stresses acting on the fluid exceed the tensile strength. The previous tensile force acting on the bulk liquid phase is sufficient to counteract the attractive forces available in the region where the initial nuclei are present. The approach mentioned above is very intuitive in the interpretation of the volume fraction spatial and temporal changes. In regions one and two, the pressure gradient acting on the bulk liquid dictates the spatial rate of tensile stress in the field, balanced with the spatial and temporal changes in the void fraction field. The governing equations illustrate that the rate of change of tensile stress determines the rate of production or destruction of the liquid phase. The spatial rate of change of tensile stress is implicitly correlated with the rate of change of the fluid element volume or the growth of the nuclei, which requires moderate tensile stress to keep growing. In other words, the spatial rate of change of tensile stress determines how fast the element of fluid is contracting or expanding in cartesian coordinates. In another viewpoint, the spatial rate of change of tensile stress determines the growth rate of holes in the flow field. The preceding analysis is very similar to the solids' behavior: the solid's failure occurs in the region where nucleation exists. Similarly, in this case, the inception and propagation of the crack occur in the weak spots located adjacent to the nucleation. Therefore, the flow field imposes varying pressure gradients on vapor structures traveling in the flow. The pressure gradient changes the structures of the vapor phase significantly, and it results in the vapor structure's growth or condensation depending on the location and time. In this sense, the instantaneous cavitation propagation and evolution can be defined through the local tensile strength of liquids.

This chapter presents the numerical modeling of the cavitation inception, break-up, and shedding as it develops in a Venturi-type section. An emphasis is placed on comparing the void ratio transport and production (destruction) of void ratio in both time and space. In this regard, instantaneous void ratio, 2-D velocity vector field, and static pressure are

utilized to implement cavitation modeling and validation. Validation and comparisons are implemented with X-ray measurements accompanied by the pressure results obtained from simulations.

As discussed in the previous chapters, cavitating flow evolution is aperiodic. It is assumed that the void transport equation governs the mass transfer between phases. A mass term or void fraction term is added to the right-hand-side of the mass transfer equation:

$$\frac{\partial \alpha}{\partial t} + u\frac{\partial \alpha}{\partial x} + v\frac{\partial \alpha}{\partial y} = \dot{m}_v \tag{8.1}$$

The mass term consists of closure parameters that are tuned through the data-driven technique mentioned in section 4.10, and the performance of the model is compared against the other models. Euclidean norms of the models are compared with each other. Various formulations of the mass transfer equation have been proposed, each of which simulates the mass transition process in a particular region of the flow field.

Modeling the cavitating flows past the throat of the Venturi-type section is challenging: as mentioned in the previous chapters, the flow mentioned above is composed of distinct regimes with complex aperiodic evolution that cannot be described through equilibrium thermodynamic relations. Although the numerical formulations of cavitation flow have been investigated thoroughly [8, 16, 27, 29, 33, 49, 56, 57, 60], the performance of the current models may be enhanced using data-driven techniques. The application of the data-driven technique allows us to extract the dominant physical terms governing the phase transition in each region of the cavitating flow. Likewise, the method identifies dominant terms mentioned in the classical cavitation models or is new terms improving our understanding and modeling performance. The fluid is assumed a homogeneous mixture of vapor and liquid in

all interrogation windows. The mixture of the two phases can be treated as a single fluid, given that the local velocity and pressure of the phases are in equilibrium.

8.2 Phase Transition Modeling in Distinct Regions of Cavitating Flow

As discussed, the void fraction and velocity vector field obtained from X-ray measurements are used in phase transition modeling. Initially, POD reduces the noise in the experimentally measured velocity vector field and void fraction field. In the second step, the void fraction transport equation is solved to obtain the instantaneous rate of phase transition in each interrogation window. Next, given the pressure field from the numerical simulation and the X-ray data, including the instantaneous void fraction and velocity vector field, phase transition modeling in distinct regions of the flow field has been implemented. In other words, given the spatial and temporal data of mass transition term $\dot{m}_v$, the best fit model is obtained using the LASSO method. As it was shown in section 4.10, the LASSO method performs the variable selection subject to a regularization parameter, $\lambda_{reg.}$ promoting sparsity of the resultant model. LASSO method improves the accuracy of the suggested model in terms of l_2 norm. At the same time, it promotes the physical interpretation of the model by penalizing less correlated terms or correlated to the noise corresponding to the coefficients close to zero. Initially, $\lambda_{reg.}$ small number where the l_1 penalty term does not promote any sparsity; therefore, the model contains all of the terms in the library. An increase in $\lambda_{reg.}$ results in the elimination of the uncorrelated terms whose coefficients are close to zero, so the complexity of the model decreases with an increase in $\lambda_{reg.}$. Here the model with the lowest number of terms and small l_2 norm is selected. Figure 8.1 illustrates the norm two obtained from the discrepancy between the experimental data and the numerical simulations.

Only the terms that are most correlated to the phase transition terms are selected as part of the LASSO method. A library of the candidate's linear and non-linear terms is selected to fit a model to the aforementioned data. Three variables are assumed to play a role in void fraction transport and phase transition phenomenon: pressure field, void fraction level, and instantaneous velocity vector field. The library consists of the polynomial functions of the system variables or any non-linear combination of the variables. Besides, the first and second spatial derivatives of the variables are accommodated in the library. In selecting the windows acquiring void fraction, only the grids that acquire more than 5% vapor are taken into account in modeling. The cavitating flow is broken down into four regions with different characteristics; look at the regions one to four in figure 3.4. After the throat of the section, the production of the vapor phase is the dominant mechanism of the transition process. Since the evaporation is dominated in this region, a high concentration of the vapor phase is observed in the region #1.

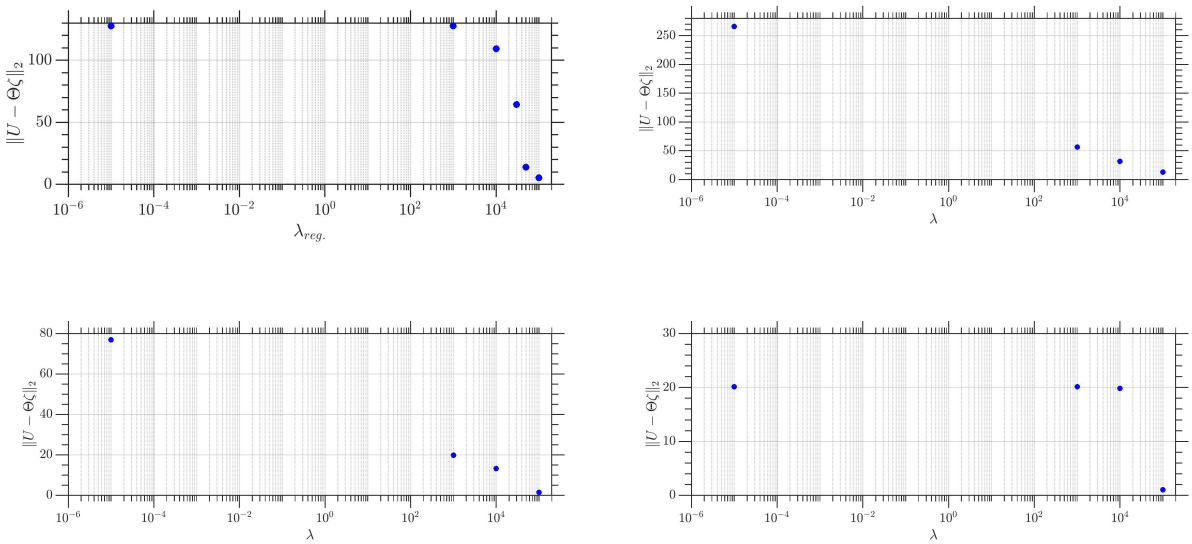

Figure 8.1: Norm two obtained from the discrepancy between the void fraction transport relation, $\frac{\partial \alpha}{\partial t} + u\frac{\partial \alpha}{\partial x} + v\frac{\partial \alpha}{\partial y}$,and vapor phase transition model, $\dot{m}_v$ in different regions of the flow field: (a) inception of the cavitation (b) vapor phase shedding, (c) break-up of the vapor phase and (d) condensation of the vapor structures. Models suggested for each region is presented in Eqs. (8.2)-(8.5).

Figure 8.2 depicts the gradient of pressure in the first region of the cavitating flow. Strong pressure gradient in this region causes spatial and temporal changes in the void fraction field.

$$\frac{\partial \alpha}{\partial t} + u\frac{\partial \alpha}{\partial x} + v\frac{\partial \alpha}{\partial y} = \psi_1 \sqrt{\frac{p_\infty}{\rho h_t^6}} \frac{h_t}{p_\infty} \frac{\partial p}{\partial y} \tag{8.2}$$

$$\frac{\partial \alpha}{\partial t} + u\frac{\partial \alpha}{\partial x} + v\frac{\partial \alpha}{\partial y} = \psi_1 + \psi_2 \frac{\partial v}{\partial y} + \psi_3 \alpha + \sqrt{\frac{p_\infty}{\rho_l h_t^6}} \frac{h_t}{p_\infty} [\psi_4 \frac{\partial p}{\partial x} + (\psi_5 + \psi_6 \alpha) \frac{\partial p}{\partial y}] \tag{8.3}$$

The spatial rate of change of tensile stress applied on the initiated nucleation of cavities results in a rupture in the fluid. Next, this void region is filled with vapor.

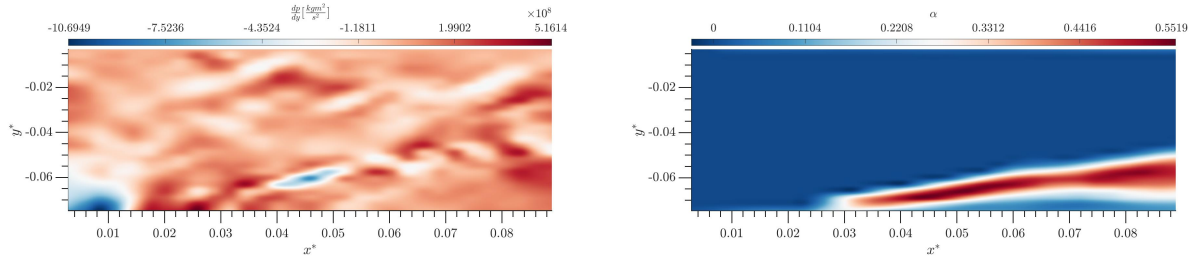

.

Figure 8.2: Representation of the non-equilibrium cavitation model suggested for region # 1 where the vapor phase is massively generated due to the high-pressure gradient. (a) the pressure gradient mainly governs the mass transition term.

According to the transport equation shown in Eq. (8.3), the rate of change of the void fraction depends on the divergence of the velocity. The preceding behavior is also observed in the third region, where the divergence of the velocity is the only mechanism of the phase transition:

$$\frac{\partial \alpha}{\partial t} + u\frac{\partial \alpha}{\partial x} + v\frac{\partial \alpha}{\partial y} = \psi_1 \alpha \frac{\partial u}{\partial x} \tag{8.4}$$

The local void fraction spatial and temporal changes enforce significant changes in the other variables of the flow field, such as the static pressure and pressure gradients. On the other hand, Eqs. (8.3) and (8.4) imply that the instantaneous velocity divergence is correlated with the void fraction changes. For instance, in the region where the void fraction is high, infinitesimal local patches of negative divergence of velocity are observed that implies the local expansion of the fluid elements, look at figures 8.3 and 8.4. The expansion causes a local increase in the vapor phase. On the other hand, in the regions where the compression of the fluid element occurs (positive velocity divergence), vapor structures are destroyed. The magnitude of the velocity divergence determines the magnitude of the compression

or expansion. For example, in regions with higher velocity divergence, the destruction of the vapor phase occurs at higher rates. Since the velocity and void fraction divergence are correlated, the speed of sound affects the void fraction transport implicitly. The active terms in the different regions suggest that the spatial and temporal changes of the void fraction are introduced by the rate of change of tensile stress, look at figure 8.6. In the first region and the locations where the vapor phase accumulates significantly, orange and red clusters, void fraction variation occurs both spatially and temporally. Besides, this variation is caused by the rate of change of tensile stress applied to the fluid elements. On the other hand, since vapor structures transport is intermittent adjacent to the wall, the void fraction is only a function of time; look at the green region in figure 8.6. It should be noted that α is zero in the blue region and the flow field is incompressible, thereby yielding no meaningful balance between the provided terms. The analysis of the dominant balance mechanism, applied to the flow field past the throat of the Venturi-type section, proves that in the regions where α is non-zero, the tensile stress is the dominant mechanism in the flow field that results in temporal and spatial changes or in one sense distribution of the void fraction field. The tensile stress distribution activates the temporal and spatial changes in the region with a concentration of void fraction. On the other hand, the applied tensile stress only causes temporal variation of the void fraction in the wake of the throat and the vicinity of the wall. The orange region depicts the region of the flow field where the unsteadiness in the void fraction is insignificant; therefore, a balance between the spatial derivatives of the void fraction and the tensile stress is acquired. Figure 8.7 illustrates that the rate of change of void fraction is balanced by the rate of change of the fluid element volume and the applied tensile stress. Once the fluid element enters the second region where the vapor cloud shedding occurs, it goes through rapid extension and contraction due to varying tensile stress. The expansion and contraction of the fluid elements manifest themselves in terms of spatial and temporal variation of the void fraction; look at the red cluster in figure 8.7. The variables

mentioned above are very intuitive: strong gradient pressure induces a strong divergence of velocity. Consequently, the divergence of velocity causes gradients in the void fraction. In some sense, tensile stress implicitly affects the distribution of the void fraction in the flow field. This clustering also shows other regions with distinct dominant balance models, such as temporally non-varying void fraction region (blue cluster), non-advective region where the void fraction transport does not occur due to the flow motion (orange region). Since, in some regions of the flow field, the concentration of the vapor phase is insignificant, the flow field is non-advective due to zero gradient of void fraction. The preceding observation proves that the void fraction time variation in an infinitesimal fluid element is balanced by the sink or source of the vapor structures caused by the variation in tensile stress and volume changes of the fluid element. Figure 8.9 displays the role of the velocity divergence on the void fraction transport. Contraction occurred due to the changes in the fluid element volume, causing the condensation of the vapor phase. On the other hand, expansion of the fluid element is the only mechanism causing the production of the cavitation structures. A unidirectional advection term is activated in the blue and orange clusters, implying that the void fraction transport resulting from the advection mechanism is dominant in one direction, and the transport process in the other direction is negligible. For instance, in the orange cluster closer to the bottom wall, the advection occurs in the x-direction. Green cluster shows a balance between temporal changes of void fraction in an element, redistribution of the void fraction due to the advective terms and generation or destruction of the vapor phase. The green cluster is very intuitive in understanding the underlying mechanism of the transport of void fraction. As a result of the expansion of the fluid element, vapor structures are generated in an element. Part of the vapor structures accumulates in the element, giving rise to the temporally varying void fraction. The rest of the vapor structures are carried away to the other locations.

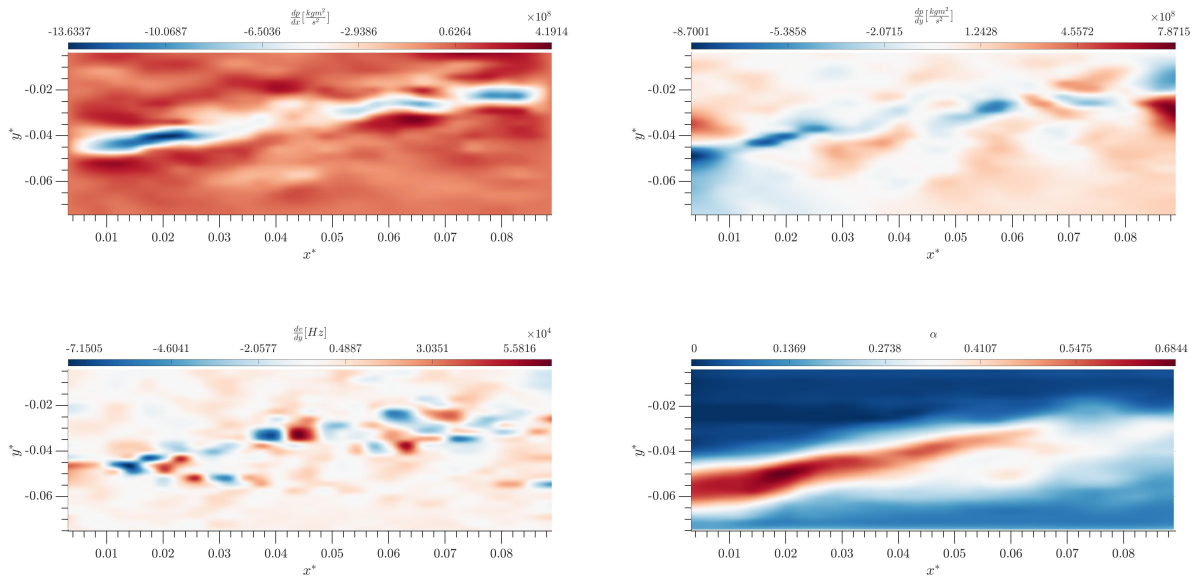

Figure 8.3: Representation of the non-equilibrium cavitation model suggested for region # 2 where the shedding of cloud cavitation is initiated. (a), (b) negative (positive) pressure gradient patches result in a sudden drop (increase) of the pressure field. The negative pressure gradient is the forerunner of cavitation structures production. A strong negative pressure gradient is observed at the liquid-vapor interface, where the pressure gradient is the dominant mechanism in cavitation production. (c) Divergence of the velocity represents the second mechanism of the production or condensation of the vapor structures. The negative (positive) patches of the divergence of the velocity delineate an expansion (contraction) of fluid element leading to production (destruction) of the vapor phase. (d) Instantaneous snapshot of the field of the void fraction in the near wake of the throat.

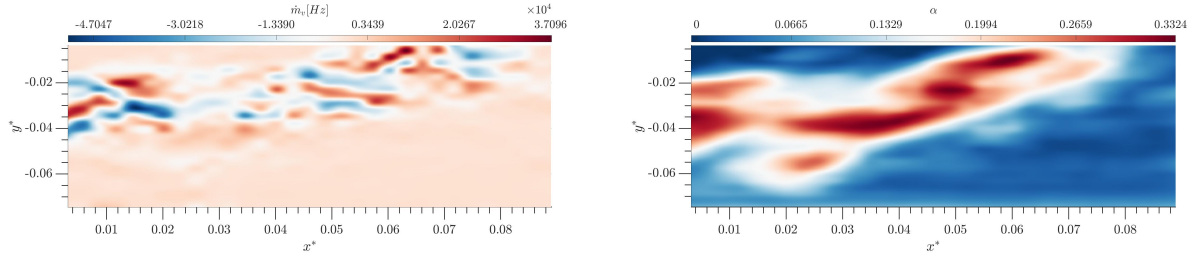

Figure 8.4: Representation of the non-equilibrium cavitation model suggested for region # 3 where the cavitation break-up occurs. (a) the divergence of the velocity mainly governs the mass transition term. For further information, look at figure 8.3 (b) Instantaneous snapshot of the field of the void fraction where the cavitation break-up occurs.

Figure 8.5 presents the effect of the pressure recovery on the condensation rate. In the near-wake of the throat, as the vapor structures pass on into the high pressure field, the vapor structures go through a condensation followed by bubbles collapse. The governing equation of the condensation process in the near-wake reads:

$$\frac{\partial \alpha}{\partial t} + u\frac{\partial \alpha}{\partial x} + v\frac{\partial \alpha}{\partial y} = \sqrt{\frac{p_\infty}{\rho_l h_t^6}}\frac{1}{p_\infty}p^2(\psi_1 + \psi_2 p) \tag{8.5}$$

The static pressure field determines the rate of destruction of the vapor phase. The cubic static pressure term causes a rapid condensation of the vapor phase. Figure 8.9 illustrates two condensation regimes: balance between non-linear pressure field and the spatial and temporal changes in the void fraction field. Since region # 4 is far from the test section geometry changes, the pressure gradient and velocity divergence terms are not included in the balance emphasizing that the production of the vapor structures does not occur in this region.

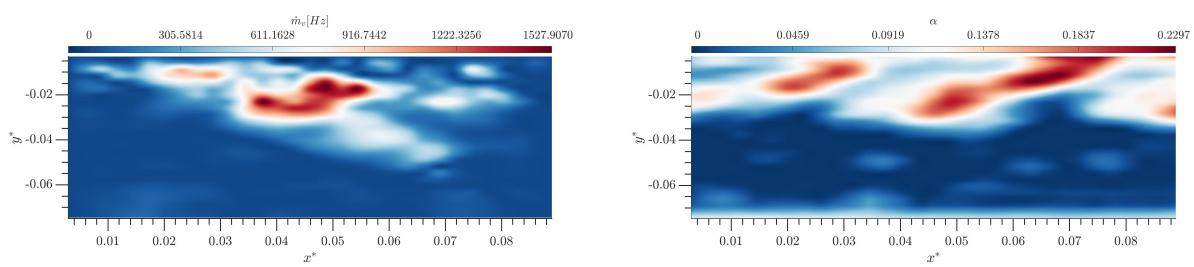

Figure 8.5: Representation of the non-equilibrium cavitation model suggested for region # 4 where the pressure recovery occurs. (a) the pressure field mainly governs the mass transition term. Since the pressure drops in the near wake, condensation of the vapor structures occurs. (b) Instantaneous snapshot of the field of the void fraction in the near wake of the Venturi-type section throat.

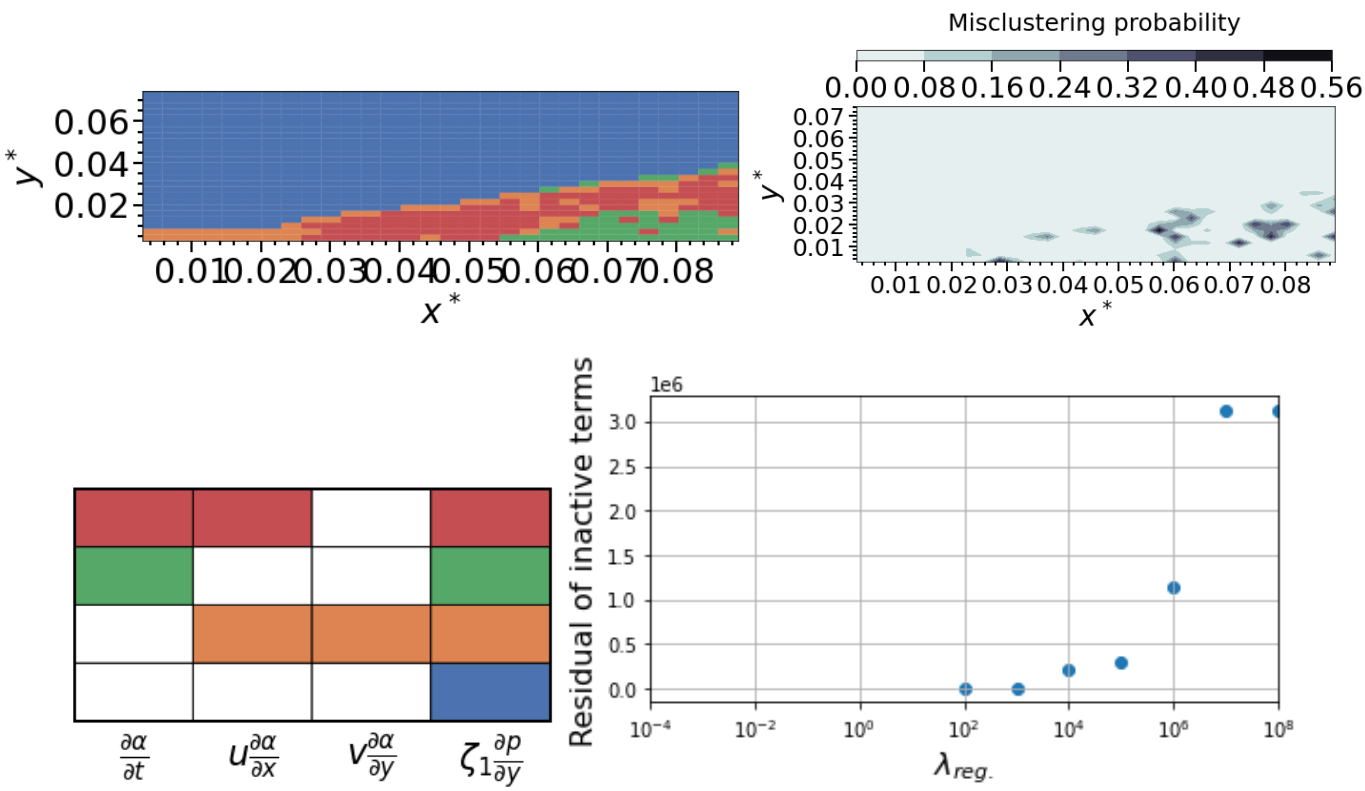

Figure 8.6: Schematic of the dominant balance identification applied to a cavitating flow for $\lambda_{reg} = 10^3$. The equation space is associated with the void ratio transport equation that governs cavitating flow right after the throat of the Venturi-type section. For further information look at figure 7.5.

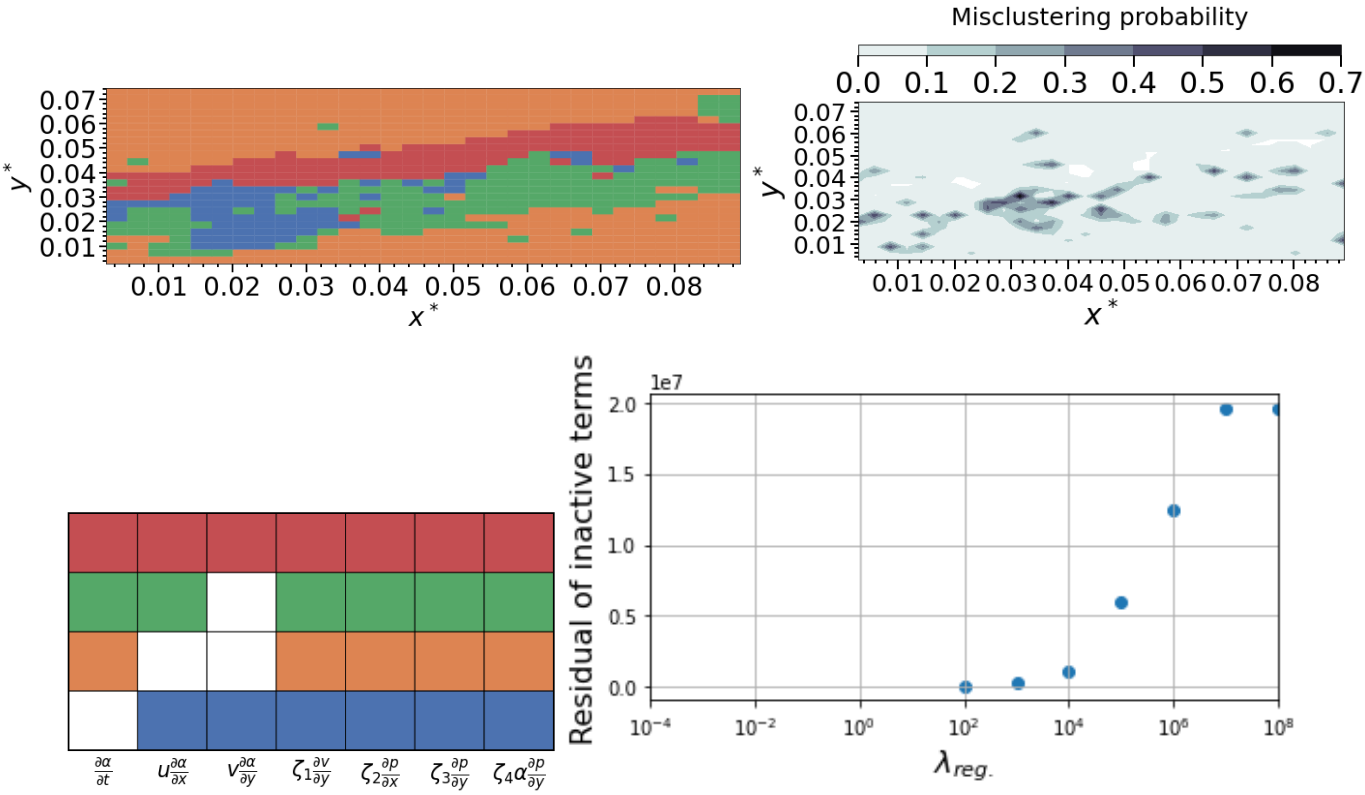

.

Figure 8.7: Schematic of the dominant balance identification applied to a cavitating flow for $\lambda_{reg} = 10^3$. The equation space is associated with the void ratio transport equation that governs cavitating flow where the vapor cloud shedding occurs. For further information look at figure 7.5.

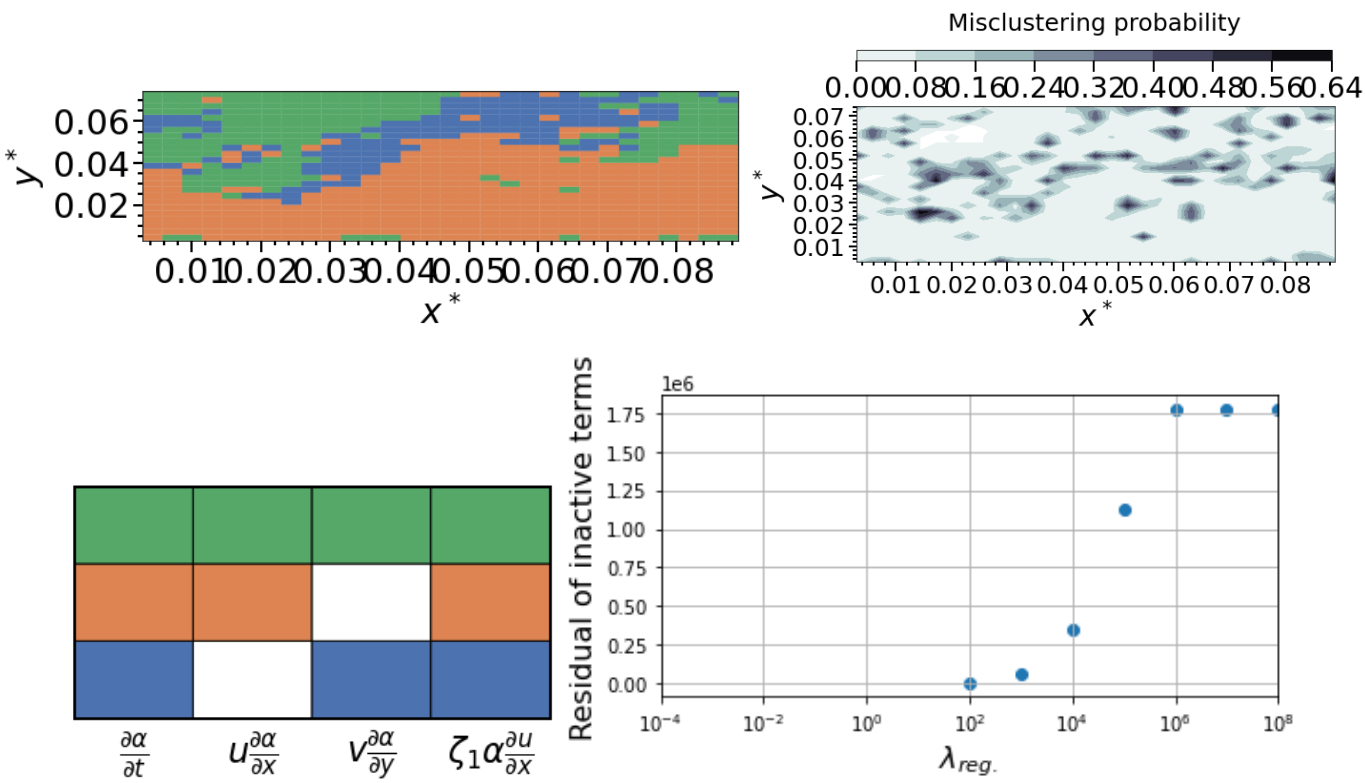

.

Figure 8.8: Schematic of the dominant balance identification applied to a cavitating flow for $\lambda_{reg} = 10^2$. The equation space is associated with the void ratio transport equation that governs cavitating flow where the cavitation break-up initiates. For further information look at figure 7.5.

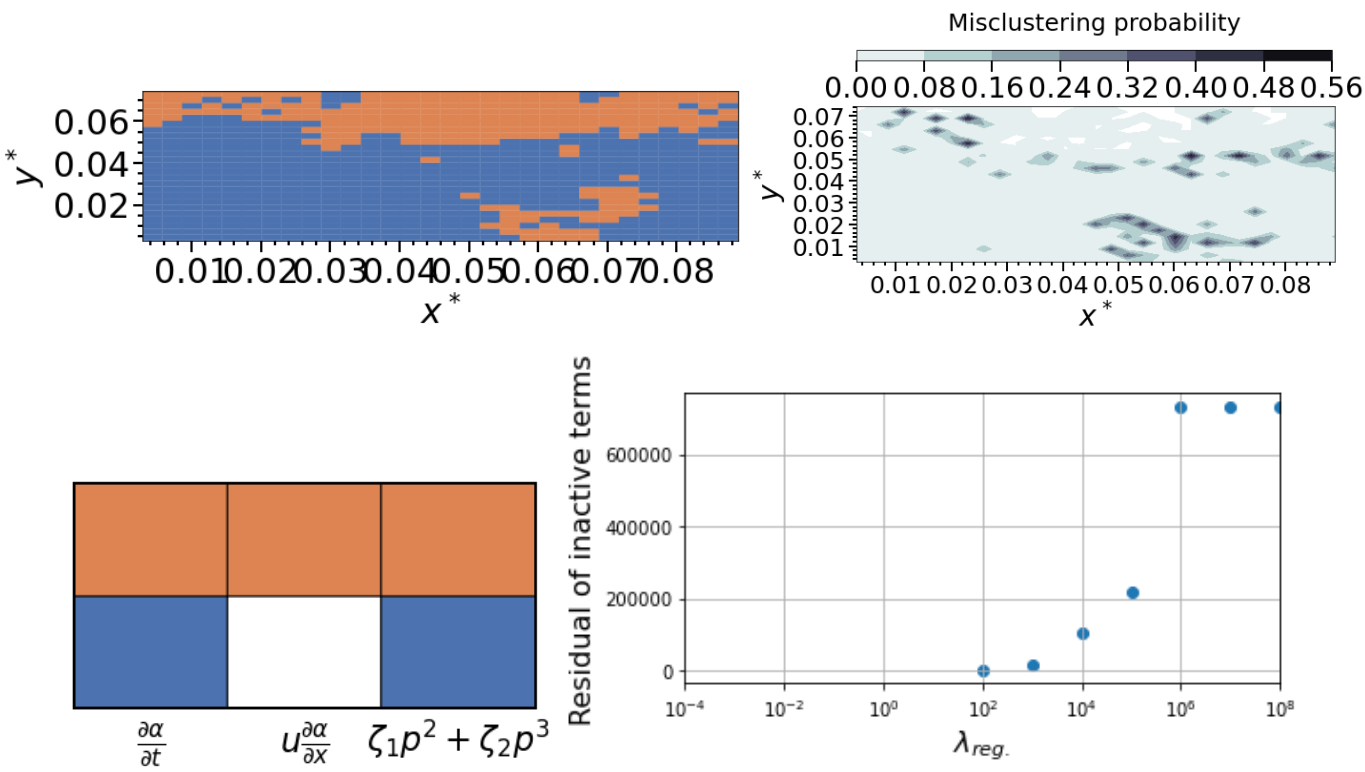

.

Figure 8.9: Schematic of the dominant balance identification applied to a cavitating flow for $\lambda_{reg} = 10^3$. The equation space is associated with the void ratio transport equation that governs cavitating flow in the near wake, where the pressure recovery imposes the condensation of the vapor phase. For further information look at figure 7.5.

Chapter 9

Conclusions and Future Research Directions

9.1 Conclusions

In chapter 6, a priori physical information extracted from the analysis of the raw high-speed images illustrates the dominant cavitating flow regimes. The observations demonstrate that the cavitating flow is aperiodic. Besides, numerous flow regimes are identified from the raw images as follows:

- Length of the attached sheet cavity oscillates significantly, and the maximum length changes in each cycle.
- Since the re-entrant jet convection is distinct in each cycle, the vapor cloud shedding pattern and scale are distinct.
- The small-scale vapor structures dissipate in the high pressure field region, while downstream larger structures collapse where the pressure field is comparably higher.

Furthermore, data-driven techniques are applied to the planar time-resolved PIV to investigate the transitions between distinct regimes of cavitating flow as it occurs in a Venturi-type

profile. Three data-driven techniques are used on the PIV data to shed light on the transition mechanisms.

Analysis of the DMD results yields the modes of instabilities. These modes are shown to be corresponding to the dominant flow patterns. Besides, similar to the Fourier transform, it has been demonstrated that the mode's isolated frequency is imperative in identifying the mode. Since DMD obtains the best fit linear model that sends the current status of the dynamical system to the future, each instabilities monotonic decay rate and their corresponding initial amplitude can be extracted. Following results are obtained applying the DMD technique on the PIV measurements:

- Modes corresponding to the Kelvin-Helmholtz instabilities developed at the interface of the two phases acquire higher decaying rate, lower frequency ratio, and lower initial amplitude.

- Instabilities modes corresponding to the vapor cloud shedding and the condensation of the vapor phase in downstream acquire lower decay rate, higher frequency, and higher initial amplitude.

CROM technique has identified three dominant flow regimes: (1) convection of a pair of coherent structures, (2) convection of triple (3) weakly triple structures. The transition matrix obtained from CROM displays the path of the transition between cavitating flow regimes. Bifurcation clusters, representing the precursor of the regime change, are illustrated—the probability of regime change or the time duration that the flow pattern changes are extracted. Besides, the time duration that the flow field remains in each pattern is extracted. The CROM analysis shows that the regime transition is tightly connected to the vapor cloud shedding, governed by the dynamics of the re-entrant jet. Besides, analysis of the POD results complements the underlying mechanisms of the transition between distinct regimes.

Separation of the length scales thorough POD deterministically revealed the path of transition between distinct instabilities. Application of the POD on the filtered data revealed the following instabilities:

- Premature condensation causes high amplitude oscillations in the closure region of the attached sheet cavity.
- Collapse of the bubbly structures gives rise to the Instabilities in the downstream region.
- The velocity and density discontinuity on the interface of the two phases lead to the KH instabilities.
- Energy transfer from the mean flow to the high-frequency fluctuations known as Drift flow instabilities.

In chapter 7, GMMs, along with SPCA, are used to cluster the force points in the Favre-averaged momentum equation space. The preceding data-driven technique facilitates the segmentation of the flow field into regions where a subset of the forces in the momentum equations are essential. Following results are obtained from learning dominant forces in the cavitating flow:

- The study mentioned above suggested the regions of the flow field where the turbulence anisotropy plays the central role in the balance between forces in an infinitesimal fluid element.
- Instabilities resulting from the formation of the attached sheet cavity and the cavitation break-up give rise to anisotropy terms. Strong anisotropic turbulence shows that the rotation level is significant inside the attached sheet cavity.

- Isotropic turbulence is the main force contributing to the balance in the governing equation, specifically in the free-stream and boundary layer.
- Pressure gradient reduces the rate of transport of TKE where the liquid-vapor interface is located.
- Pressure-dilatation and pressure work can reverse the cascade of energy.
- It is observed that the transport of kinetic energy due to the velocity and pressure turbulent fluctuations is more efficient than the transport through molecular processes.

Chapter 8 focuses on the modeling of the liquid-vapor phase transition. A few assumptions have been placed for the modeling as follows:

- The process happens rapidly; therefore, it is assumed that the process is isothermal.
- Density of the species is constant and independent of pressure.
- The two phases are well mixed up, and the mixture is assumed to be homogeneous.

As the initial step in the modeling, void fraction transport is assumed to be balanced by a phase transition term. Then, it is suggested that the rate of change of void fraction in an infinitesimal element of fluid is correlated with three distinct mechanisms:

- Spatial rate of expansion (contraction) of the fluid element.
- Spatial rate of change of tensile stress applied on the fluid element
- Absolute compressive stress applied on the fluid element.

It is shown that the first two mechanisms are both responsible for the destruction and production of the vapor phase, and they are functions of time and space. The last mechanism

is responsible for the condensation of the vapor phase, and it occurs in the regions where the pressure value is comparably high.

9.2 Future Research Directions

Besides the research outline states in the previous section, the following topics can be studied further to improve our understanding and modeling of the cavitating flows:

- The suggested models for the void fraction transport can be combined to obtain one unified equation valid for the entire domain. In this regard, a blending function needs to be defined that bridges the near-throat relations to the other regions of the flow field where the vapor cloud shedding and cavitation break-up occur. The blending function requires an explicit measurement of some variables in the system, such as void fraction. In other words, the blending function explicitly depends on a variable that uses the preceding variable to blend the near-throat formula with the formulas of the other regions. The blending function can predict the variables of the flow field in a variety of regimes.

- Although in the current study it is assumed that the flow field is viscous, the limited resolution of the camera was a barrier that might underestimate the viscous terms in the governing equations significantly. Based on the boundary layer theory, the role of the viscous stresses are significant in the vicinity of the wall; however, since the spatial resolution was limited in the vicinity of the wall, the viscous stresses are underestimated. Besides, higher spatial and temporal resolution is required to shed light on the underlying physics of the viscous stresses in distinct regions of the cavitating flow.

- Investigation of the effect of the collapse of the vapor cloud on the evolution of the

attached sheet cavity

Bibliography

[1] *Reduced-Order Modelling for Flow Control.* R. Noack, M. Morzynski, and G. Tadmor. Springer, Wien, New York, 2011.

[2] N. M. Laird A. P. Dempster and D. B. Rubin. Maximum likelihood from incomplete data via the em algorithm. *Journal of the Royal Statistical Society: Series B (Methodological)*, 39:1–22, 1977.

[3] H. Li A.K. Singhal, M.M. Athavale and Y. Jiang. Mathematical basis and validation of the full cavitation model. *J. Fluids Eng.*, 124:617—624, 2002.

[4] Hiroharu Kato Akihiro Kubota and Hajime Yamaguchi. A new modelling of cavitating flows: a numerical study of unsteady cavitation on a hydrofoil section. *Journal of Fluid Mechanics*, 240:59–96, 1992. doi: 10.1017/S002211209200003X.

[5] H.L. Swinney A.M. Fraser. Independent coordinates for strange attractors from mutual information. *Physical review A*, 33(2):1134, 1986.

[6] Florent Ravelet Olivier Coutier-Delgosha Farid Bakir Amélie Danlos, Jean-Elie Mehal. Study of the cavitating instability on a grooved venturi profile. *J. Fluids Eng.*, 136(10), 2013. doi: 10.1115/1.4027472.

[7] R.E.A. Arndt. Cavitation in vortical flows. *Annual Review in Fluid Mechanics*, 34(10): 143—175, 2002.

[8] G.Y. Wang B. Huang. A modified density based cavitation model for time dependent turbulent cavitating flow computations. *Chinese Science Bulletin*, 56:1985—1992, 2011.

[9] Aleš Raidl B. Kliková. Reconstruction of phase space of dynamical systems using method of time delay. *Proceedings of the 20th Annual Conference WDS 2011*, 2011.

[10] M. MORZYŃSKI G. TADMOR B. R. NOACK, K. AFANASIEV and F. THIELE. A hierarchy of low-dimensional models for the transient and post-transient cylinder wake. *Journal of Fluid Mechanics*, 497:335–363, 2003.

[11] Y. Iwata T. Ikohagi B. R. Shin. Numerical simulation of unsteady cavitating flows using a homogenous equilibrium model. *Computational Mechanics*, 30:388—395, 2003.

[12] G. Birkhoff and E.H. Zarantonello. *Jets, Wakes, and Cavities.* Academic Press Inc., 1957.

[13] Eric Goncalvès Boris Charrière, Jean Decaix. A comparative study of cavitation models in a venturi flow. *European Journal of Mechanics B/Fluids*, 49:287–297, 2015.

[14] C.E. Brennen. *Cavitation and Bubble Dynamics.* Oxford University Press, 1995.

[15] M. Achintya C. Souvick and S. Swarnendu. Stability study of laminar flame using proper orthogonal decomposition. *in n^3l – International Summer School and Workshop on Non-Normal and Nonlinear Effects in Aero- and Thermoacoustics,*, pages 18—21, 2013. doi: https://doi.org/10.1115/FEDSM2009-78407.

[16] J.Z. Feng C.L. Merkle and P.E.O.Buelow. Computational modeling of the dynamics of sheet cavitation. *In Proceedings of 3rd International Symposium on Cavitation, Grenoble*, 2:307—311, 1998.

[17] SHERVIN BAGHERI PHILIPP SCHLATTER CLARENCE W. ROWLEY, IGOR MEZIĆ and DAN S. HENNINGSON. Spectral analysis of nonlinear flows. *Journal of Fluid Mechanics*, 641:115–127, 2009. doi: 10.1017/S0022112009992059.

[18] J. Dang. Numerical simulation of unsteady partial cavity flows. *PhD thesis, Delft University*, 3, 2001.

[19] P.B. Whalley D.R.H. Beattie. A simple two-phase fractional pressure drop calculation method. *International Journal of Multiphase Flow*, 8:83–87, 1982.

[20] L. Cordier A. Spohn-M. Segond M. Abel G. Daviller J. Östh S. Krajnović E. Kaiser, B. R. Noack and R. K. Niven. Cluster-based reduced-order modelling of a mixing layer. *Journal of Fluid Mechanics*, 754:365–414, 2014.

[21] Leonhard Euler. Théorie plus complette des machines qui sont mises en mouvement par la réaction de l'eau. *Mémoires de l'académie des sciences de Berlin*, 10:227–295, 1756.

[22] J.P. Franc. Partial cavity instabilities and re-entrant jet. *In CAV2001: Fourth International Symposium on Cavitation. California Institute of Technology, Pasadena, USA*, 2001.

[23] J.P. Franc and J.M. Michel. *Fundamentals of Cavitation*. Kluwer Academic Publishers, 2004.

[24] S. Fujikawa and T. Akamatsu. Effects of the non-equilibrium condensation of vapour on the pressure wave produced by the collapse of a bubble in a liquid. *Journal of Fluid Mechanics*, 97:481—512, 1980.

[25] C. L. Hu-B. Huang G. H. Chen, G. Y. Wang and M. D. Zhang. Observations and measurements on unsteady cavitating flows using a simultaneous sampling approach. *Experiments in Fluids*, 56(32), 2015. doi: 10.1007/s00348-015-1896-8.

[26] Y.C. Wang G.E. Reisman and C.E. Brennen. Observations of shock waves in cloud cavitation. *Journal of Fluid Mechanics*, 355:255—283, 1998.

[27] I.H. Sezal G.H. Schnerr and S.J. Schmidt. Numerical investigation of three dimensional cloud cavitation with special emphasis on collapse induced shock dynamics. *Physics of Fluids*, 20, 2008.

[28] Bruce P. Gibbs. *Advanced Kalman Filtering, Least-Squares and Modeling: A Practical Handbook*. Wiley, 2011.

[29] Eric Goncalvès. Numerical study of expansion tube problems: Toward the simulation of cavitation. *Computers & Fluids*, 72:1–19, 2013.

[30] O. Coutier-Delgosha Guangjian Zhang, Ilyass Khlifa. A comparative study of quasi-stable sheet cavities at different stages based on fast synchrotron x-ray imaging. *Physics of Fluids*, 32, 2020.

[31] Park Warn-Gyu-Merkle Charles L. Ha, Cong-Tu. Multiphase flow analysis of cylinder using a new cavitation model. *Proceedings of the 7th International Symposium on Cavitation, CAV2009*, 2009.

[32] H. Helmholtz. On discontinuous movements of fluids. *The London, Edinburgh, and Dublin Philosophical Magazine and Journal of Science*, 36:337–346, 2009.

[33] U. Iben. Modeling of cavitation. *Systems Analysis Modeling Simulations*, 42:1283—1307, 2002.

[34] Daniele Ragni-Artur Palha1 Richard P. Dwight Iliass Azijli, Andrea Sciacchitano. A posteriori uncertainty quantification of piv-based pressure data. *Experiments in Fluids*, 12(72), 2016.

[35] ITTC. Final report of the specialist committee on computational method for propeller cavitation. *In Proceedings of 22nd International Towing Tank Conference*, 3, 1999.

[36] G. H. Schnerr J. Sauer. Development of a new cavitation model based on bubble dynamics. *Journal of Applied Mathematics and Mechanics*, 81(S3):561–562, 2011.

[37] B.R. Noack J.A. Bourgeois and R.J. Martinuzzi. Generalized phase average with applications to sensor-based flow estimation of the wall-mounted square cylinder wake. *Journal of Fluid Mechanics*, 736:316–350, 2013.

[38] Bingni W. Brunton J. Nathan Kutz Steven L. Brunton Jared L. Callaham, James V. Koch. Learning dominant physical processes with data-driven balance models. *Nature Communications*, 12, 2021.

[39] Olivier COUTIER Jean-Luc REBOUD, Benoit STUTZ*. Two-phase flow structure of cavitation: Experiment and modelling of unsteady effects. *Third International Symposium on Cavitation*, 2013.

[40] Tamer A.Zaki Jin Lee. Detection algorithm for turbulent interfaces and large-scale structures in intermittent flows. *Computers & Fluids*, 175:142–158, 2018.

[41] E. Johnsen and T. Colonius. Compressible multi-component flow calculations and shock-bubble interaction. in sixth international symposium on cavitation, cav2006, wageningen, the netherlands, 2006. marin. 2006.

[42] G. Kirchhoff. Zur theorie freier fl¨ussigkeitsstrahlen. *J. reine angew. Math.*, 70:289—298, 1869.

[43] Coutier-Delgosha O. Leroux, J.-B. and J.-A. Astolfi. A joint experimental and numerical study of mechanisms associated to instability of partial cavitation on two-dimensional hydrofoil. *Physics of Fluids*, 17(5), 2005. doi: 10.1063/1.1865692.

[44] J.-C. Loiseau and S. L. Brunton. Constrained sparse galerkin regression. *Journal of Fluid Mechanics*, 838:42–67, 2018. doi: https://doi.org/10.1017/jfm.2017.823.

[45] P. A Lush and P. I. Peters. Visualisation of the cavitating flow in a venturi type duct using high-speed cine photography. *Proc. IAHR Conf. on Operating Problems of Pump Stations and Power Plants*, 5:1–13, 1982.

[46] O. Coutier-Delgosha M. Adama Maiga and D. Buisine. A new cavitation model based on bubble-bubble interactions. *Physics of Fluids*, 30, 2018.

[47] R. Brown M. B. Kennel and H. D. I. Abarbanel. Determining embedding dimension for phase-space reconstruction using a geometrical construction. *Physical Review E*, 45: 3403, 1992.

[48] S. Fuzier M. Adama Maiga & O. Coutier-Delgosha M. Dular, I. Khlifa. Scale effect on unsteady cloud cavitation. *Experiments in Fluids*, 53:1233—1250, 2012.

[49] R. Bachert B. Stoffel M. Frobenius, R. Schilling and G. Ludwig. Three-dimensional, unsteady cavitation effects on a single hydrofoil and in a radial pump measurements and numerical simulations, part two: numerical simulation. *In: Proc. 5th Int. Symp. Cavitation (CAV2003), Osaka*, 2003.

[50] JEAN-MARIE MICHEL MATHIEU CALLENAERE, JEAN-PIERRE FRANC and MICHEL RIONDET. The cavitation instability induced by the development of a re-entrant jet. *Journal of Fluid Mechanics*, 444, 2001.

[51] Mark Effertz Morten Kjeldsen, Roger E. A. Arndt. Spectral characteristics of sheet/-cloud cavitation. *J. Fluids Eng.*, 122(3):481–487, 2000. doi: 10.1115/1.1287854.

[52] J.D. Farmer R.S. Shaw N.H. Packard, J.P. Crutchfield. Geometry from a time series. *Physical review letters*, 45(9):712, 1980.

[53] S. Ulam Nicholas Metropolis. The monte carlo method. *Journal of the American Statistical Association*, 44:335–341, 1949.

[54] A. VABRE O. COUTIER-DELGOSHA, B. STUTZ and S. LEGOUPIL. Analysis of cavitating flow structure by experimental and numerical investigations. *Journal of Fluid Mechanics*, 578:171, 222, 2007. doi: 10.1017/S0022112007004934.

[55] M. Hocevar R. Delion A. Dazin D. Lazaro M. Gmar K. Fezzaa W-K. Lee O. Coutier-Delgosha, A. Vabre. Local measurements in cavitating flow by ultra-fast x-ray imaging. *American Society of Mechanical Engineers*, pages 371–379, 2009.

[56] T. Belamri P.J. Zwart, G. Gerber. A two-phase flow model for prediction cavitation dynamics. *In: Proc. 5th Int. Conf. Multiphase Flow (ICMF 2004), Yokohama*, 2004.

[57] R. Abgrall R. Saurel, F. Petitpas. Modelling phase transition in metastable liquids: application to cavitating and flashing flows. *J. Fluid Mech*, 607:313—350, 2008.

[58] L. Rayleigh. On the pressure developed in a liquid during the collapse of a spherical cavity. *Philosoph. Mag.*, 34:94—98, 1917.

[59] B. Stutz & J. L. Reboud. Experiments on unsteady cavitation. *Experiments in Fluids*, 22:191—198, 1997.

[60] T.S. Chyczewski D.R. Stinebring H.J. Gibeling R.F., D.A. Boger and T.R Govindan. Multi-phase cfd analysis of natural and ventilated cavitation about submerged bodies. *In Proceedings of 3rd ASME/JSME Joint Fluids Engineering Conference, pages ASME Paper FEDSM99–7364*, 1999.

[61] C. Rhodes and M. Morari. False-nearest-neighbors algorithm and noise-corrupted time series. *Physical Review E*, 55:6162, 1997.

[62] E. P. Rood. Review—mechanisms of cavitation inception. *J. Fluids Eng.*, 113(2): 163,175, 1991. doi: 10.1115/1.2909476.

[63] J.W. Daily R.T. Knapp and F.G. Hammitt. *Cavitation*. McGraw-Hill Book Company, 1993.

[64] S. Sen S. Chatterjee, A. Mukhopadhyay. Stability study of laminar flame using proper orthogonal decomposition and dynamic mode decomposition. *n3l - International Summer School and Workshop on Non-Normal and Nonlinear Effects in Aero- and Thermoacoustics*, pages 18–21, 2013.

[65] Joshua L. Proctor J. Nathan Kutz Samuel H. Rudy, Steven L. Brunton. Data-driven discovery of partial differential equations. *Science Advances*, 3(4), 2016.

[66] G.H. Schnerr & J. Sauer. Physical and numerical modeling of unsteady cavitation dynamics. *In: Proc. 4th Int. Conf. Multiphase Flow (ICMF'01), New Orleans*, 2001.

[67] I.H. Sezal S.J. Schmidt and G.H. Schnerr. Compressible simulation of high-speed hydrodynamics with phase change. *ECCOMAS CFD*, 2006.

[68] B. Stutz and J.-L. Reboud. Experiments on unsteady cavitation. *Experiments in Fluids*, 22:191–198, 1997a. doi: 10.1007/s003480050037.

[69] B. Stutz and J.-L. Reboud. Measurements within unsteady cavitation. *Experiments in Fluids*, 29:545–552, 2000. doi: 10.1007/s003480000122.

[70] V.A. Tselischev S.Y. Konstantinov, D.V. Tselischev. Numerical cavitation model for simulation of mass flow stabilization effect in ansys cfx. *Modern Applied Science*, 9: 21—31, 2015.

[71] M. Tosaki S. Allen J.S. Takagi N. Ohta T. Kitamura T. Ikeda, S. Yoshizawa and Y. Matsumoto. Cloud cavitation control for lithotripsy using highintensity focused ultrasound. *Ultrasound in Medicine and Biology*, 32:1383—1397, 2006.

[72] J. (Sir) Thornycroft and S.W. Barnaby. Torpedo boat destroyers. *Minutes of Proceedings of the Institution of Civil Engineers*, 122:51–103, 1895.

[73] R. Tibshirani. Regression shrinkage and selection via the lasso. *Journal of the Royal Statistical Society*, 58:267–288, 1996.

[74] D.H. Trevena. *Cavitation and Tension in Liquids.* Adam Hilger, 1987.

[75] N.V.B. Vaz. Modeling of sheet cavitation on hydrofoils and marine propellers using boundary element methods. *PhD thesis, Universidade T ecnica de Lisboa*, 2005.

[76] G. Wallis. *One-Dimensional Two-phase Flow.* McGraw-Hill, New York, 1967.

[77] T.Y-T. Wu. Cavity and wake flows. *Annual Reviews of Fluid Mechanics*, 4:243—284, 1972.

[78] Pengcheng Guo F Hong X Q Luo X B ZHENG, L L Liu. Improved schnerr-sauer cavitation model for unsteady cavitating flow on naca66. *IOP Conference Series Earth and Environmental Science*, 163(1), 2018.

[79] T. Ikohagi Y. Saito, I. Nakamori. Numerical analysis of unsteady vaporous cavitating flow around a hydrofoil. *In: Proc. 5th Int. Symp. Cavitation (CAV2003), Osaka*, 2003.

[80] S. D. Heister Yongliang Chen. Modeling hydrodynamic nonequilibrium in cavitating flows. *J. Fluids Eng.*, 118(1):172–178, 1996. doi: 10.1115/1.2817497.

[81] R.J. Martinuzzi Z. Hosseini and B.R. Noack. Sensor-based estimation of the velocity in the wake of a low-aspect-ratio pyramid. *Experiments in Fluids*, 56(13), 2015.

[82] Robert J. Martinuzzi Z. Hosseini and B. R. Noack. Modal energy flow analysis of a highly modulated wake behind a wall-mounted pyramid. *Journal of Fluid Mechanics*, 798:717–750, 2016.